

ISSN 1810-648X
E-ISSN 2537-6365



GHITU INSTITUTE OF ELECTRONIC
ENGINEERING AND NANOTECHNOLOGIES

INSTITUTE OF APPLIED PHYSICS

STATE UNIVERSITY OF MOLDOVA

PHYSICAL SOCIETY OF MOLDOVA

Moldavian Journal of the Physical Sciences

Chisinau
2018

Volume 17
No. 3-4

Scientific journal **Moldavian Journal of the Physical Sciences** includes original scientific articles, communications and reviews concerning various problems of modern physics. The journal is published in English, its periodicity is 4 numbers a year, with circulation of 200 copies.

web: <http://sfm.asm.md/moldphys/>

© Ghitu Institute of Electronic Engineering and Nanotechnologies, 2002

EDITORIAL BOARD

Editor-in chief **Veaceslav Ursaki**
Assistant Editor **Ion Tiginyanu**
Assistant Editor **Anatolie Sidorenko**
Assistant Editor **Mihai Macovei**
Assistant Editor **Florentin Paladi**
Assistant Editor **Anatolie Casian**
Responsible secretary **Sofia Donu**

BOARD MEMBERS

| | | |
|---------------|---------------|--------------|
| E. Arushanov | V. Kravtsov | V. Nicorici |
| I. Belousov | L. Kulyuk | E. Rusu |
| E. Condrea | S. Moskalenko | N. Sirbu |
| V. Dorogan | V. Moskalenko | V. Shontea |
| E. Evtodiev | T. Munteanu | D. Tsiuleanu |
| V. Fomin | D. Nedeoglo | V. Tronciu |
| M. Iovu | D. Nica | V. Tsurkan |
| S. Klokishner | A. Nikolaeva | S. Vatavu |

ADVISORY BOARD

| | |
|-------------------------|-------------------------------|
| E. Aifantis, Greece | F. Kusmartsev, United Kingdom |
| Z. Alferov, Russia | V. Moshnyaga, Germany |
| V. Aksenov, Russia | D. Nagy, Hungary |
| A. Balandin, USA | J. Lipkowski, Poland |
| E. Bucher, Germany | V. Litovchenko, Ukraine |
| A. Buzdin, France | L. Pintilie, România |
| E. Burzo, România | A. Revcolevschi, France |
| H. Chiriac, Romania | H. Scherrer, France |
| Z. Dashevsky, Israel | A. Simashkevich, R. Moldova |
| Yu. Dekhtyar, Latvia | F. Sizov, Ukraine |
| J. T. Devreese, Belgium | R. Tidecks, Germany |
| J. Dudley, France | B. Tsukerblat, Israel |
| M. Enachescu, România | M. Y. Valakh, Ukraine |
| O. Guven, Turkey | V. Vlad, Romania |
| H. Hartnagel, Germany | G. Zegrea, Russia |
| M. Kolwas, Poland | D. Khokhlov, Russia |

EXECUTIVE EDITORIAL BOARD

Svetlana Alekseeva
Constantin Morari
Marina Timoshinina

GUIDELINES FOR AUTHORS

The “Moldavian Journal of Physical Sciences” appears quarterly and publishes in English papers referring to original scientific research in physics and related fields, including applications in electronics and technology, material engineering and device physics. A review paper for every issue is planned and short communications with hot news are encouraged.

Papers must be prefaced by a brief abstract in English up to 100 words. Single space of the rows in the manuscript is required.

Authors are invited to send two printed copies of their papers, as well as an electronic record on a 3^{1/4} inches diskette, or by e-mail, in English. The articles will be edited by using WORD for Windows. Chapters must be numbered by using Arabic figures, as follows:

3. Experimental results.
- 3.1. Results analysis.
- 3.2. Methods of calculus.

Formulae must be written very clearly and easy-to-read. Do not use non-explained abbreviations. Illustrations and diagrams must be realized on computer drafts (on images). All graphic and text objects must be of very good quality and easy to read. Figures included in the text are preferable.

Reference citations will be presented as follows: author’s forename initial and last name, journal name, volume, page number, year (in parentheses), for example: F.A. Moldovan, S.P. Russu, Phys. Rev. Let. 85, 357, (2000). Complete title, publisher, city and year will be written for book’s author’s name and forename initial, for example: M. Teodorescu, Cooperation in science and technology with Eastern and European countries, Editura Tehnica, Bucuresti, vol. 1, 1992. References into the text will be made within square brackets, for example [7]; reference citation numbers must be made successively, as they appear into the text.

Manuscripts of regular papers should be limited up to 10 pages and will be signed by authors; they also must be marked “Ready to print”. Reviews are limited up to 20 pages. Maximum 4 pages are admitted for short communications. One full page of the journal (size A4) contains 54 rows with 95 characters/row; font size - 12. Page set up: top, left, right – 2,5; bottom – 3,5 cm. The very manuscript which is marked “Ready to print” will be published within 6 months from sending.

The submitted papers must be reviewed by two independent reviewers. The papers must contain original work and have not submitted for publication to any other journal. The papers which have been published previously, as well those accepted to be published in other reviews, will be not be admitted by Editorial Board; the authors have to mention this situation.

Proofs will be sent to authors for checking. Corrections must be restricted to errors since modifications to the text may be charged to the author. The publishers reserve the right to adapt the presentation of an article to conform to our style. After their publishing in our journal, the manuscripts and corresponding illustrations become the property of Editorial Board and will not be returned to the authors. The same for the papers, which have not been admitted for publication. The publishing in our journal is made free of charge.

All rights are reserved by ”Journal”. Any reproduction or dissemination of the information herein, even as excerpts of any extent, is permitted only by written consent of the Editorial Board.

The papers sent for publishing are considered not secret. The authors only are responsible for this in front of their own institutes or employers. Authors have to mention their complete address and telephone, fax number and e-mail.

Papers from around the world can be sent to be published to the following address:
Ghitu Institute of Electronic Engineering and Nanotechnologies, 3/3 Academy St., MD 2028 Chisinau, the Republic of Moldova, tel. (00 37322) 73-70-92; E-mail: ursaki@yahoo.com, E-mail of responsible secretary: sofiadonu@yahoo.com

TAILORING ELECTRON AND PHONON ENERGY DISPERSION AND THERMAL TRANSPORT IN NANO- AND MICROARCHITECTURES

V. M. Fomin^{1,2}

¹*Institute for Integrative Nanosciences,
Leibniz Institute for Solid State and Material Research, Dresden,
Dresden, D-01069 Germany*

²*Department of Theoretical Physics, Department of Physics and Engineering, Moldova State
University, Chisinau, MD-2009 Republic of Moldova
E-mail: v.fomin@ifw-dresden.de*

(Received August 8, 2018)

1. Introduction

The use of nontrivial geometry and topology for effective tailoring physical properties of diversified quantum fields in novel micro- and nanostructures is one of the most appealing avenues in modern nanophysics and nanotechnologies [1]. Analysis of topologically nontrivial manifolds at the nanoscale is of immense importance for semiconductor, superconductor, and graphene physics as well as for optics, magnetism, and quantum computing. The highly diversified investigations underpin development of promising low-cost high-performance electronic, spintronic, optoelectronic, optical memory, and information processing technology based on quantum rings and related nanoarchitectures. Nanostructuring, as suggested more than two decades ago [2], creates a timely opportunity to search for new advanced thermoelectric materials (see [3, 4] for reviews).

Thermoelectric energy conversion efficiency is quantified by the figure of merit

$$ZT = \frac{S^2 \sigma T}{\kappa_{ph} + \kappa_{el}},$$

where S is the Seebeck coefficient, σ is the electrical conductivity, T is the absolute temperature, κ_{ph} and κ_{el} are the phonon and electron thermal conductivities, respectively. The electron thermal conductivity is usually much smaller than the phonon one. The phonon thermal conductivity is usually dominated by acoustic phonons because of their higher group velocity and lower energy (resulting in higher population factors) as compared with optical phonons. The ambitious task for advancing thermoelectric applications is thus to create materials that would combine properties of (i) electronic metals with high values of the Seebeck coefficient and electric conductivity and (ii) phonon insulators with low values of the phonon thermal conductivity. In what follows, some of the results in the field are overviewed from the point of view of the present author's scientific interests.

The development of subbands of electron spatial quantization in 1D stacks of quantum dots (or, equivalently, segmented nanowires (NWs)) allows for an efficient control over the Seebeck coefficient and the electrical conductivity [5], phonon-engineered thermal transport in NWs with constant and periodically modulated crosssections as well as with core-shell structure [6–8]. A decrease in phonon group velocities in combination with an enhancement of phonon

boundary scattering implies a significant reduction of the phonon lattice thermal conductivity compared with bulk.

Efficient engineering acoustic phonon energy spectrum has been searched for in rolled-up multishell tubular structures. The strain-driven roll-up procedure is an available instrument for the preparation of multilayer micro- and nanosuperlattices (SLs) and their arrays [9–11]. The acoustic phonon dispersion in multishell tubular structures has been analyzed in terms of elastodynamics [12]. It has been shown that the number of shells is an important control parameter of the phonon dispersion together with the structure dimensions and acoustic impedance mismatch between the shells. An increase in the number of shells has been demonstrated to lead to an appreciable decrease in the average and rms phonon group velocities.

2. Effect of the Miniband Energy Spectrum on the Electronic Transport Characteristics in a Periodic 1D Stack of Disk-Shaped InAs/GaAs Quantum Dots (QDs)

An approach for numerical calculation of the electron dispersion, the transport relaxation time, and the transport coefficients in a periodic 1D stack of disk-shaped InAs/GaAs QDs (1D QD SL) has been developed [5]. We study the effect of narrow electronic minibands (Fig. 1) in periodic 1D stacks of disk-shaped InAs QDs in GaAs on their electronic transport characteristics by employing an empirical tight-binding calculation and a continuum model of the electronic structure. Our model includes both the minibands and the continuum of the host conduction band. By calculating the relaxation time for acoustic-phonon scattering explicitly, we show that the popular approximation of a constant relaxation time is not adequate for cross-plane transport through a stack of semiconductor QDs.

From the numerical analysis of the electric and thermal conductivities, the Seebeck coefficient and the figure-of-merit, we conclude that electronic signatures of nanostructurings should be detectable in the thermoelectric response of a 1D stack of QDs. For judiciously chosen values of the donor concentration, depending on the geometrical parameters of the QD SL (see Fig. 2), the thermoelectric power factor is strongly enhanced. Hence, a QD SL exemplifies a material, whose efficiency as a thermoelectric converter is controlled by geometry on the nanoscale. The thermoelectric figure-of-merit as a function of the donor concentration represents the miniband electron energy spectrum of the QD stack and thus can be used as an experimental fingerprint of the electronic structure of it. This method works best for low temperatures and flat QDs.

The highest ZT values are achieved for QDs separated by extremely thin spacer layers, when the miniband features in transport merge with the background due to the conduction band of the host material. For the system studied, InAs QDs in GaAs, the predicted figure-of-merit achieves, at an optimum nanoarchitecture of the stack, maximal values of about 2.7, assuming the achieved phonon heat conductivity values of $\kappa_{ph} \sim 0.5 \text{ W m}^{-1} \text{ K}^{-1}$ (see the forthcoming Sections). Our results imply that for technical operation of QD SLs as thermoelectric converters, the choice of the *optimum nanoarchitecture* and *doping concentration* is of paramount importance.

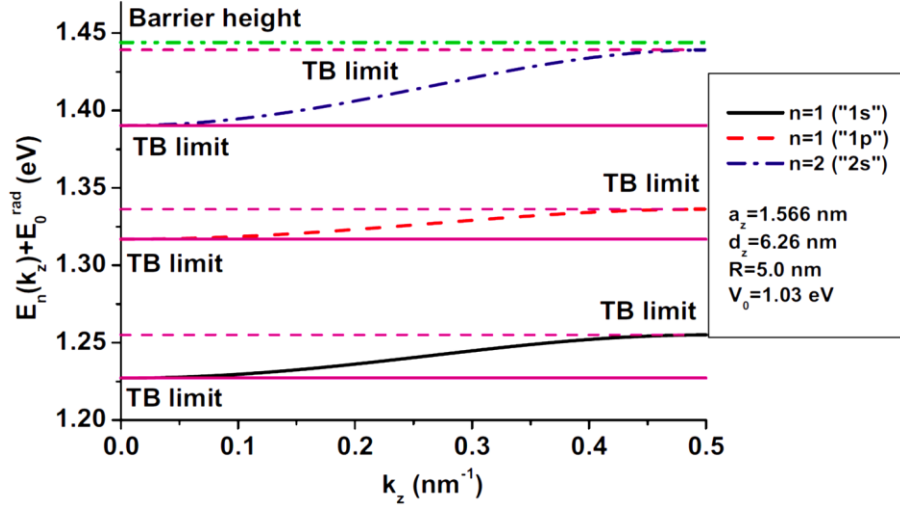


Fig. 1. Renormalized minibands in a 1D stack of InAs/GaAs QDs with geometrical parameters indicated in the inset. The valence band top of GaAs is taken as the zero of the energy. The dash-dotted line represents the position of the barrier (reprinted from [5]).

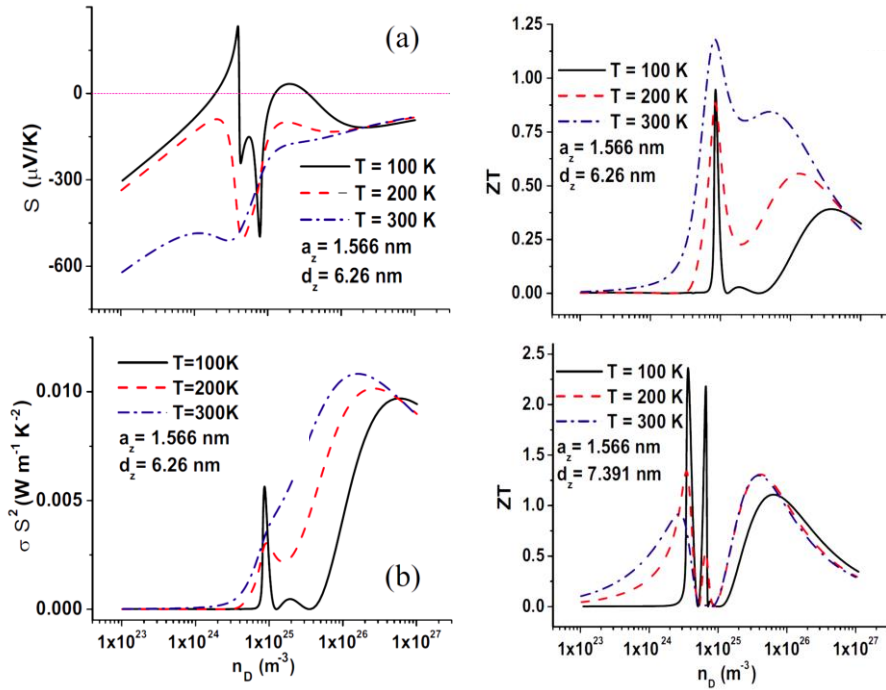


Fig. 2. Left panel: (a) the Seebeck coefficient and (b) the power factor in a stack of InAs/GaAs QDs. Right panel: the figure-of-merit for stacks of InAs/GaAs QDs with geometric parameters indicated in the insets (after [5]).

3. Phonon Filtering and Reduction of Lattice Thermal Conductivity in One-Dimensional QD SLs

It has been theoretically shown that one-dimensional QD SLs (1D-QDSLs) consisting of acoustically mismatched materials exhibit sub-1 W m⁻¹K⁻¹ thermal conductivity in a temperature range of 50–400 K. Coherent Si/Ge 1D-QDSLs, as well as model Si/plastic, Si/SiO₂, and Si/SiC 1D-QDSLs, have been studied [6]. The phonon energy spectra and group velocities are obtained in

terms of the Face-Centered Cubic-Cell model of the Born–von Karman (BvK)-approach to lattice dynamics. On this basis, lattice thermal conductivity is calculated within the Boltzmann transport equation. A strong reduction of lattice thermal conductivity in 1D-QDSL structures in comparison with homogeneous rectangular Si NWs (Fig. 3) is attributed to the exclusion of phonon modes folded in SL segments from the heat flow and the decelerating action of Ge, SiO₂, or plastic materials. Thus, the 1D-QDSL structures act as effective *phonon filters* and thereby eliminate a significant number of phonon modes from thermal transport. The obtained results imply that QDSLs are promising as thermoelectric materials and thermal insulators.

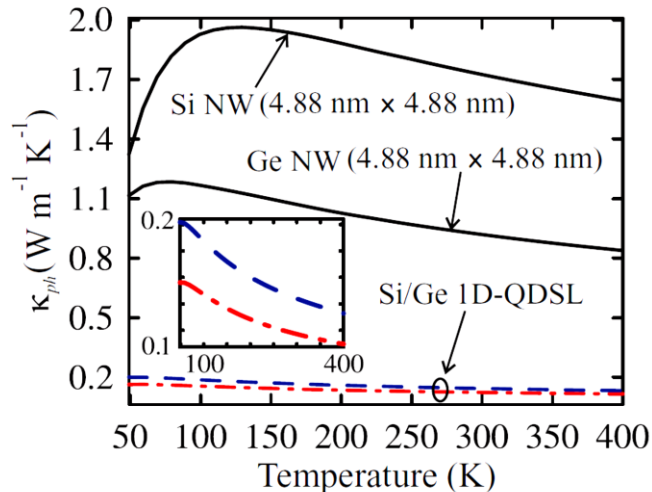


Fig. 3. Temperature dependence of lattice thermal conductivity for Si and Ge homogeneous NWs (solid lines) and for Si/Ge 1D-QDSLs with six atomic layers of Si and two atomic layers of Ge (dashed line) and with four atomic layers of Si and four atomic layers of Ge (dash-dotted line) per SL period. The inset shows a magnified view of the above temperature dependence of thermal conductivity for 1D-QDSLs (reprinted from [6]).

4. Suppression of Phonon Heat Conduction in Cross-Section-Modulated NWs (MNWs)

We have theoretically shown that a phonon heat flux can be significantly suppressed in Si and Si/SiO₂NWs with a periodically modulated cross-section area, which is referred to as the *cross-section-MNWs*, compared with the generic uniform cross-section NWs. The phonon energy spectra were obtained using the five-parameter BvK approach and the Face-Centered-Cubic-Cell model for description of the lattice dynamics. The thermal flux and thermal conductivity in Si and Si/SiO₂ cross-section-MNWs are calculated using the Boltzmann transport equation within the relaxation time approximation. Redistribution of the phonon energy spectra in the cross-section-MNWs leads to a strong decrease in the average phonon group velocities and a respective suppression of the phonon thermal flux in these NWs compared with the generic NWs. This effect is attributed to the exclusion of the phonon modes trapped in the segments of cross-section-MNWs from the heat flow. As a result, a three- to sevenfold drop in the phonon heat flux in a temperature range of 50–400 K is predicted for Si and Si/SiO₂ cross-section-MNWs under consideration. The obtained results indicate that cross-section-MNWs are promising candidates for thermoelectric applications.

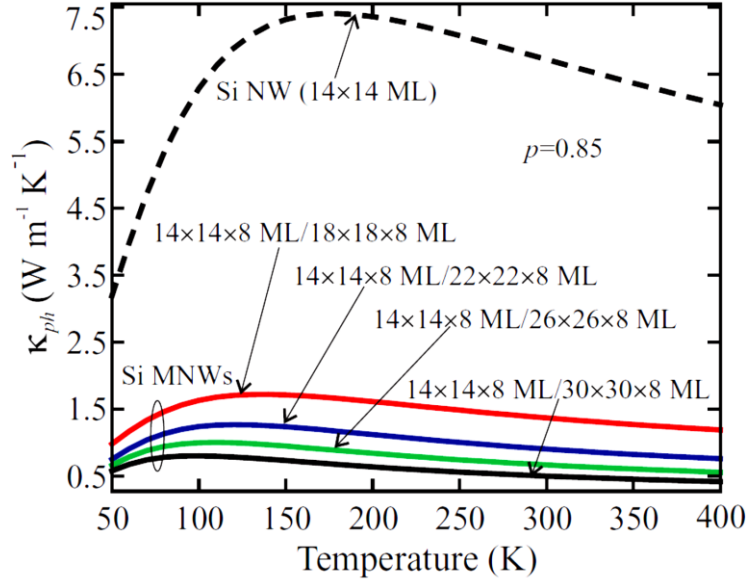


Fig. 4. Temperature dependence of the lattice thermal conductivity in the Si NW with the cross section of 14×14 ML and the various Si cross-section-MNWs with geometric parameters given in the insets (reprinted from [7]).

Our results show that, for all values of specularity parameter p under consideration, the thermal flux carried by the long-wavelength phonon modes in MNWs is lower by a factor of ~ 5 than that in NWs due to *phonon trapping*. An increase in p leads to a decrease in the thermal flux carried by the long-wavelength phonon modes and strongly enhances the thermal flux carried by the rest of the phonon modes in NWs due to attenuation of the boundary scattering of the high-energy phonon modes. These modes in MNWs are not involved in the heat transfer because of their localization in the wide segments. For this reason, the ratio between thermal fluxes in the NW and MNWs appreciably depends on specularity parameter p (Fig. 5).

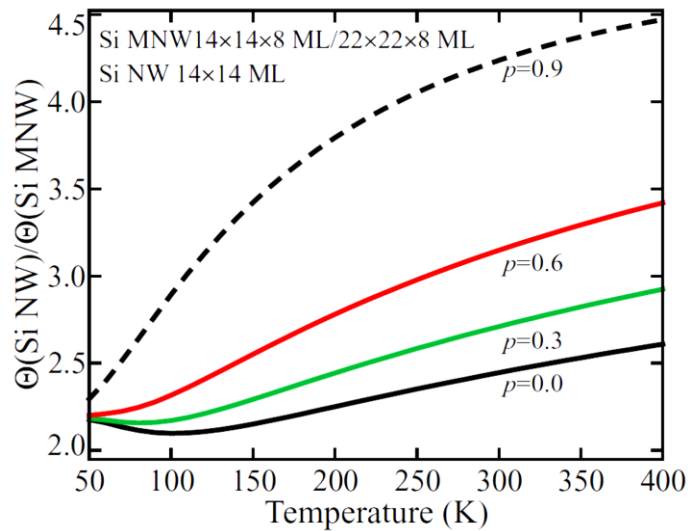


Fig. 5. Temperature dependence of the ratio of thermal fluxes in the Si NW and the Si MNW. The results are shown for different values of specularity parameter $p = 0.0, 0.3, 0.6,$ and 0.9 (reprinted from [7]).

5. Phonon-Engineered Thermal Transport in Si Wires: A Crossover between Nano- and Microscale Regimes

More recently, we have theoretically studied the transition between nanoscale and microscale thermal transport regime at room temperature in Si wires with constant and periodically modulated cross-section. Extrapolating the calculated thermal conductivity from the nano- to micrometer range, we find the characteristic dimensions of the wires, where a crossover between nanoscale and microscale thermal transport occurs. This crossover is observed in both generic (smooth) and cross-section-modulated wires. In case of smooth Si wires, we reveal a strong dependence of the crossing point position on the boundary roughness. For silicon wires with weak boundary roughness, the crossover (Fig. 6) occurs at crosssections of 60×300 nm, while for very rough boundaries it occurs at crosssections of 150×750 nm. In case of periodically modulated wires, the crossover between nano- and microscale regimes occurs at typical crosssections of 120×120 nm of the narrow segment, and it is almost independent of boundary roughness. A strong distinction from the case of smooth wires is attributed to (i) different trends of the phonon thermal conductivity at the nanometer scale, wherefrom the extrapolation was performed, and (ii) different phonon–boundary scattering due to the specific geometry. For modulated silicon wires, the effect of the modulation thickness, the modulation length, and the cross-sectional area on the phonon thermal conductivity at the room temperature is analyzed. A possibility of thermal transport engineering in cross-section-modulated wires by resizing them is revealed in both nano- and microscale regimes. The presented results pave the way towards a better understanding of thermal transport reduction in Si NWs with engineered diameter modulations and shed light on the *crossover between nano- and microscale regimes* of thermal transport.

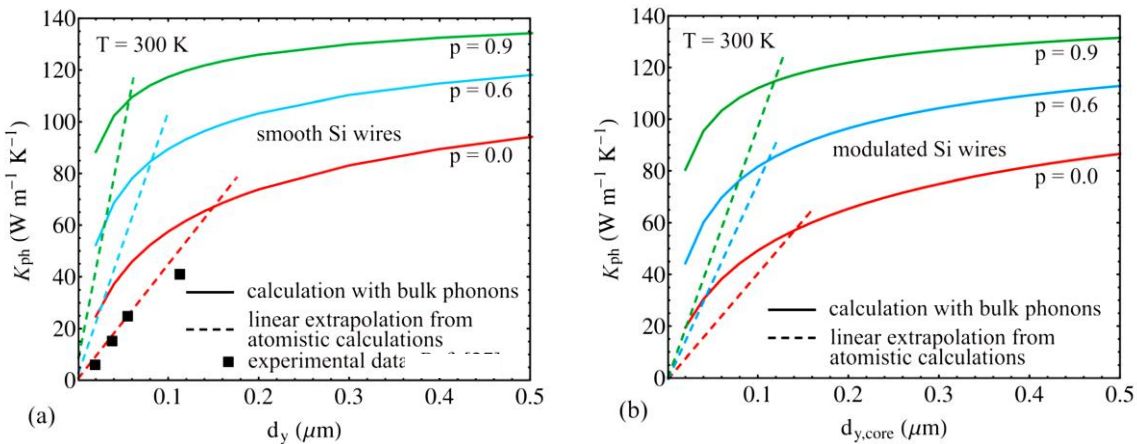


Fig. 6. Room-temperature phonon thermal conductivity: (a) as a function of the cross-section size of smooth Si wires and (b) as a function of core thickness d_y of square-cross-section modulated Si wires for different values of specularity parameter $p = 0, 0.6, \text{ and } 0.9$. Filled squares denote experimental data from [13] (reprinted from [8]).

6. In-Plane Thermal Conductivity of Radial and Planar Si/SiO_x Hybrid Nanomembrane SLs

Although silicon has been widely used in modern electronic devices, it has not yet been implemented in thermoelectric applications mainly due to high thermal conductivity

κ , which leads to an extremely low figure of merit. An approach to manage κ of Si thin-film based nanoarchitectures has been designed through the formation of radial and planar Si/SiO_x hybrid nanomembrane SLs (HNMSLs). For radial Si/SiO_x HNMSLs with different numbers of windings (1, 2, and 5), which are produced by a high-tech method of strain-driven self-assembly (roll-up), a continuous reduction in κ with an increase in the number of windings is observed (Fig. 7). Meanwhile, the planar Si/SiO_x HNMSL, which is prepared by mechanically compressing a five-winding rolled-up microtube, shows the smallest in-plane thermal conductivity among all the reported values for Si-based SLs. A theoretical model is proposed within the framework of the BvK approach to lattice dynamics to quantitatively interpret the experimental data (Fig. 8). The average phonon group velocities are calculated over the entire Brillouin zone. The results are plotted as a function of phonon energy in Fig. 8 (left panel). For Si/SiO₂ HNMSL, average is taken for a particular component of the phonon group velocity (in-plane or cross-plane). The figure reveals an appreciable effect of the phonon confinement on phonon energy dispersion and group velocities in Si/SiO₂ HNMSLs. It is significant that there appear hybrid modes propagating in the whole structure, rather than separate vibrational modes in individual Si or SiO₂ layers. Figure 8 (right panel) shows theoretical results for the lattice thermal conductivity for HNMSL with amorphous SiO₂ layers at different values of mean vibrational energy $\langle E \rangle$: 34 meV (purple curve), 53 meV (black curve), and 70 meV (green curve), along with those for HNMSL with crystalline α -quartz layers (gray curve). The performed analysis indicates that the thermal conductivity of Si/SiO_x HNMSLs is largely determined by the phonon processes in the SiO_x layers.

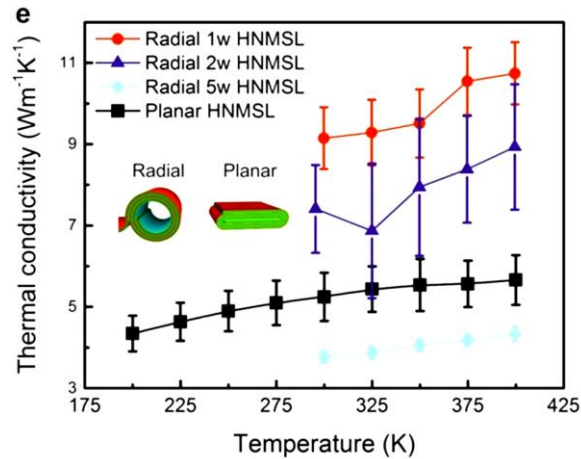


Fig. 7. Experimental in-plane thermal conductivities of planar (black squares) and radial (red circles for one-winding, purple triangles for two-winding and cyan diamonds for five-winding) Si/SiO_x HNMSLs as a function of temperature (reprinted from [11]).

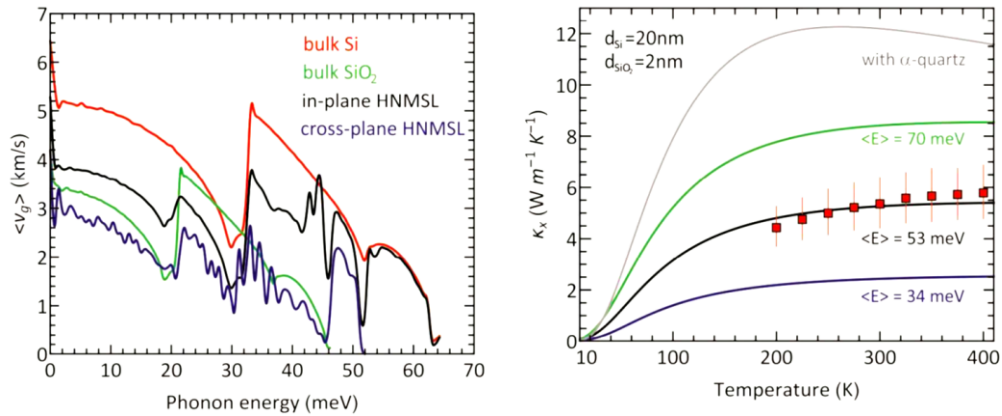


Fig. 8. Theoretical model for planar Si/SiO₂ HNMSLs: (a) schematic structure of a planar Si/SiO₂ HNMSL with a SL period consisting of 2-nm SiO₂, 20-nm Si, and 2-nm SiO₂. Left panel: average phonon group velocity as a function of phonon energy for the Si/SiO₂ HNMSL (black curve, in-plane component; purple curve, cross-plane component), bulk Si (red curve), and bulk SiO₂ (green curve). Right panel: in-plane lattice thermal conductivity as a function of temperature in the Si/SiO₂ HNMSL. Red solid squares denote the experimental data (reprinted from [11]).

7. Phonon Spectrum Engineering in Rolled-Up Micro- and Nanoarchitectures

The strain-driven roll-up procedure paves the way for novel classes of metamaterials, such as single semiconductor radial micro- and nanocrystals and multilayer radial micro- and nanosuperlattices. We have analyzed a possibility of efficient engineering of the acoustic phonon energy spectrum in multishell tubular structures, which provide a model for radial SLs [12]. The acoustic phonon dispersion is determined by solving the equations of elastodynamics for constituent (InAs/GaAs or Si/SiO₂) bi-material systems. It is shown that the total number of shells N_L is an important control parameter of the phonon dispersion along with the structure dimensions and acoustic impedance mismatch between the SL layers. The obtained results suggest that rolled-up nanoarchitectures are promising for thermoelectric applications owing to a possibility of significant reduction of the thermal conductivity without degradation of the electronic transport

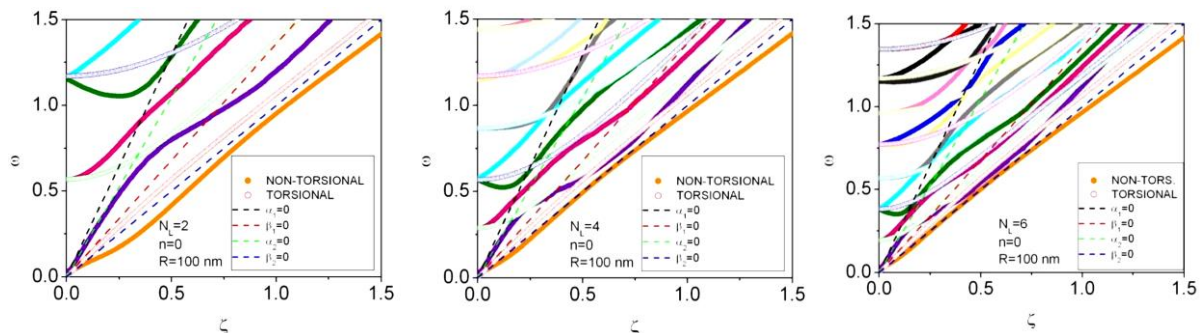


Fig. 9. Phonon dispersion curves for $n = 0$ and $N_L = 2, 4, 6$. The inner and outer radii of the InAs/GaAs multishell tubes are $r_0 = 100$ nm and $r_2 = 110$ nm, $r_4 = 120$ nm, $r_6 = 130$ nm, respectively. Non-torsional and torsional modes are represented by filled and empty circles, respectively. The dashed lines indicate the dispersion curves for dilatational ($\alpha_i = 0$) and shear ($\beta_i = 0$) waves (reprinted from [12]).

To visualize the overall impact of the number of layers in a multishelltube on the group velocity, the average and rms phonon group velocities are calculated for the branches available from the above results (see Fig. 10). At small wave vectors, the average and rms phonon group velocities decrease with increasing N_L .

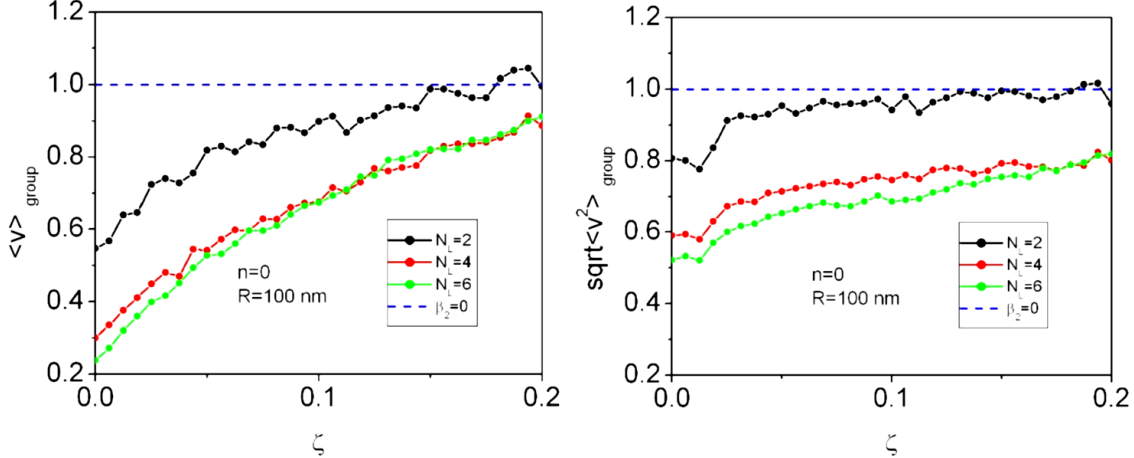


Fig. 10. Average (left panel) and rms phonon group velocity dispersion curves (right panel) for $n = 0$ at $N_L = 2, 4,$ and 6 (reprinted from [12]).

Phonon dispersion curves in Si/SiO₂ multishell tubes with two and four shells are shown in Fig. 11, where the dimensional unit is ~ 5 meV for phonon energy $\hbar\omega$ and $\sim 5 \times 10^8 \text{ m}^{-1}$ for the wave number. With increasing wave number, more phonon modes reveal an appreciable dispersion and therefore provide a larger contribution to the thermal conductivity. The dispersion curves of non-torsional modes in a multishell structure exhibit significant kinks when hitting the dispersion curve of a Rayleigh wave at the surface of Si corresponding to the dispersion relation of a dilatational wave $\alpha_1=0$. The dispersion curves of torsional modes in a multishell structure exhibit moderate kinks when hitting the dispersion curve of a Rayleigh wave at the surface of SiO₂ stemming from the dispersion relation of a shear wave $\beta_2=0$.

The calculated phonon density of states (DOS) reveals almost equidistant peaks typical of a 1D quantum wire (Fig. 12). This fact sheds light on the nature of the vibrational excitations in multishell tubes. The corresponding average group velocity (green) as a function of energy represents the spectral structure of the phonon DOS. The periods of DOS exhibit a hyperbolic dependence on the number of shells N_L with high accuracy. Similarly to Fig. 10, phonon group velocity calculated for long-wave phonons in Si/SiO₂ multishell tubes systematically decreases within increasing N_L .

In the framework of the ongoing research [14], an atomistic calculation is applied to tackle the phonons and thermal transport in multishell nanotubes.

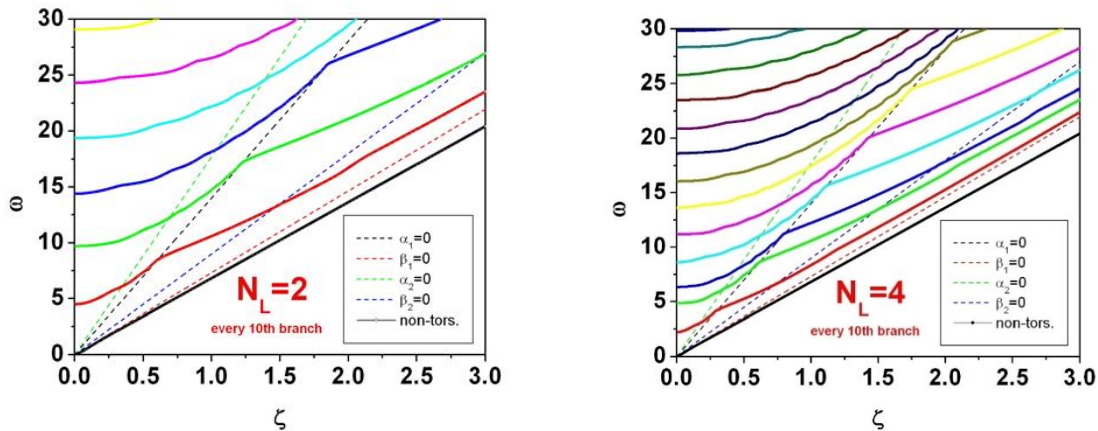


Fig. 11. Phonon dispersion curves for Si/SiO₂ multishell nanotubes with $N_L = 2$ and 4. The inner radius is $r_0=1050$ nm; the thicknesses of the Si and SiO₂ shells are 18 and 2 nm, respectively.

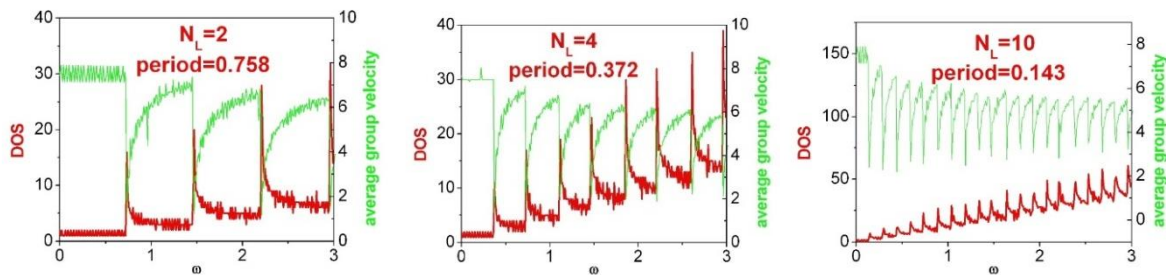


Fig. 12. Phonon DOS and average group velocity for Si/SiO₂ multishell nanotubes with $N_L = 2, 4,$ and 10. The inner radius is $r_0=1050$ nm; the thicknesses of the Si and SiO₂ shells are 18 and 2 nm, respectively.

Conclusions

For various micro- and nanoarchitectures, we have found a possibility of efficiently engineering the Seebeck coefficient and electric conductivity in 1D stacks of QDs, acoustic phonon energy dispersion in 1D QD SLs, cross-section-MNWs, Si wires ranging from nanoscale to microscale, and, more recently, multishell tubular structures. The changes in the acoustic phonon spectrum and their effect on phonon transport have been experimentally detected in first thermal conductivity measurements. Further studies are required to show that a reduction in the phonon group velocity and phonon thermal conductivity can be achieved without significant roughness scattering and degradation of electron transport. Our results suggest that 1D stacks of QDs (1D QD SLs), cross-section-modulated micro- and nanowires, as well as arrays of rolled-up radial SLs, are promising candidates for an advancement in thermoelectric materials and devices.

Acknowledgments. I gratefully acknowledge collaborations with A.A. Balandin, C.I. Isacova, A.I. Cocemasov, D.L. Nika, D. Grimm, G. Li, K. Manga, A. Mavrokefalos, F. Zhu, and O.G. Schmidt. This work has been supported by the German Research Foundation (DFG) through grant no. FO-956/4-1 MULTISHELL.

References

- [1] V.M. Fomin, Topology-driven effects in advanced nanoarchitectures, in: A. Sidorenko (Ed.), *Functional Nanostructures and Metamaterials for Superconducting Spintronics*, Springer International Publishing, Cham, 2018, pp. 195–220.
- [2] L. Hicks and M. Dresselhaus, *Phys. Rev. B* 47, 12727 (1993).
- [3] M.S. Dresselhaus, G. Chen, M. Y. Tang, R. G. Yang, H. Lee, D. Z. Wang, Z. F. Ren, J.-P. Fleurial, and P. Gogna, *Adv. Mater.* 19, 1043 (2007).
- [4] A.A. Balandin and D.L. Nika, *Mater. Today* 15 (6), 266 (2012).
- [5] V. M. Fomin and P. Kratzer, *Phys. Rev. B* 82, 045318 (2010).
- [6] D.L. Nika, E.P. Pokatilov, A.A. Balandin, V.M. Fomin, A. Rastelli, and O.G. Schmidt, *Phys. Rev. B* 84, 165415 (2011).
- [7] D.L. Nika, A.I. Cocemasov, C.I. Isacova, A.A. Balandin, V.M. Fomin, and O.G. Schmidt, *Phys. Rev. B* 85, 205439 (2012).
- [8] A.I. Cocemasov, D.L. Nika, V.M. Fomin, D. Grimm, and O.G. Schmidt, *Appl. Phys. Lett.* 107, 011904 (2015).
- [9] D. Grimm, R.B. Wilson, B. Teshome, S. Gorantla, M.H. Rummeli, T. Bublath, E. Zallo, G. Li, D.G. Cahill, and O.G. Schmidt, *Nano Lett.* 14, 2387 (2014).
- [10] G. Li, D. Grimm, V. Engemaier, S. Löscher, K. Manga, V. K. Bandari, F. Zhu, and O.G. Schmidt, *Phys. Status Solidi (A)* 213, 620 (2016).
- [11] G. Li, M. Yarali, A. Cocemasov, S. Baunack, D. L. Nika, V. M. Fomin, S. Singh, T. Gemming, F. Zhu, A. Mavrokefalos, and O.G. Schmidt, *ACS Nano* 11, 8215 (2017).
- [12] V.M. Fomin and A.A. Balandin, *Appl. Sci.* 5, 728 (2015).
- [13] D. Li, Y. Wu, P. Kim, L. Shi, P. Yang, and A. Majumdar, *Appl. Phys. Lett.* 83, 2934 (2003).
- [14] C. I. Isacova, A. I. Cocemasov, D. L. Nika, and V.M. Fomin (under preparation).

DEPENDENCE OF PEIERLS TRANSITION ON CARRIER CONCENTRATION IN ORGANIC CRYSTALS OF TTT_2I_3 IN THE 3D APPROXIMATION

S. Andronic and A. Casian

*Technical University of Moldova, Stefan cel Mare Avenue 168, Chisinau,
MD-2004 Republic of Moldova
E-mail: andronic_silvia@yahoo.com*

(Received November 19, 2018)

Abstract

The dependence of the Peierls structural transition on carrier concentration in quasi-one-dimensional (Q1D) organic crystals of TTT_2I_3 is studied in the 3D approximation. A more complete physical model that considers simultaneously two most important electron–phonon interactions is used. The first interaction is similar to that of deformation potential, while the second one is of the polaron type. The dynamical interaction of carriers with defects is also taken into account. An analytic expression for the phonon Green function is obtained in the random phase approximation. A renormalized phonon spectrum is determined for different values of dimensionless Fermi momentum k_F . In all cases, the Peierls critical temperature is determined.

1. Introduction

Quasi-one-dimensional organic crystals of tetrathiotetracene iodide (TTT_2I_3) exhibit promising thermoelectric properties. These materials were synthesized independently and nearly simultaneously [1–4] with the aim to find superconductivity in a low-dimensional conductor. At the same time, these crystals show a metal–dielectric transition with decreasing temperature.

Tetrathiotetracene iodide crystals are composed of segregate chains of TTT and iodine. Tetrathiotetracene iodide is a charge-transfer compound. The lattice constants are $a = 18.40 \text{ \AA}$, $b = 4.96 \text{ \AA}$, and $c = 18.32 \text{ \AA}$, which are indicative of a pronounced crystal quasi-one-dimensionality. The highly conducting direction is that along b . The compound is of mixed valence. Two molecules of TTT give one electron to the iodine chain composed of I_3^- ions, which play the role of acceptors. However, the crystals admit a nonstoichiometric composition with a surplus or deficiency of iodine. Therefore, the metal–dielectric transition takes place at different carrier concentrations.

The Peierls transition was studied by many authors (see [5–7] and references therein). Earlier, it was shown for a $\text{TTT}_2\text{I}_{3,1}$ crystal that the transition is of Peierls type.

Previously [8], the Peierls transition in TTT_2I_3 crystals was analyzed in the 2D approximation. It was found that the Peierls transition begins at $T \sim 35 \text{ K}$ in TTT chains and considerably reduces the electrical conductivity. Due to the interchain interaction, the transition is completed at $T \sim 19 \text{ K}$.

A 3D physical crystal model was studied in [9]. A $\text{TTT}_2\text{I}_{3,1}$ crystal was analyzed. In this case, dimensionless Fermi momentum $k_F = 0.517\pi/2$. The transition begins at $T \sim 35 \text{ K}$ in TTT chains. Due to the interchain interaction, the transition is completed at $T \sim 9.8 \text{ K}$. It was observed

in experiments that the electrical conductivity has a maximum at 35 K and achieves zero at $T \sim 10$ K. It was shown that the hole–phonon interaction and the interactions with structural defects diminish the renormalized phonon spectrum $\Omega(q_x)$ and reduce the sound velocity in a wide temperature range.

In this paper, we study the behavior of the Peierls transition in TTT_2I_3 crystals in the 3D approximation for different k_F values that is determined by variations in the carrier concentration. Defect scattering is also considered. Peierls critical temperature T_p is determined for different values of dimensionless Fermi momentum $k_F - \delta$, where δ is the variation in Fermi momentum k_F due to a decrease in the carrier concentration. The results obtained in the 3D physical model are analyzed and commented in detail.

2. Three-Dimensional Physical Model of the Crystal

The physical model of the crystal was described in more detail in [8]. The Hamiltonian of the 3D crystal model in the tight binding and nearest neighbor approximations has the form

$$H = \sum_{\mathbf{k}} \varepsilon(\mathbf{k}) a_{\mathbf{k}}^{\dagger} a_{\mathbf{k}} + \sum_{\mathbf{q}} \hbar \omega_{\mathbf{q}} b_{\mathbf{q}}^{\dagger} b_{\mathbf{q}} + \sum_{\mathbf{k}, \mathbf{q}} A(\mathbf{k}, \mathbf{q}) a_{\mathbf{k}}^{\dagger} a_{\mathbf{k}+\mathbf{q}} (b_{\mathbf{q}} + b_{-\mathbf{q}}^{\dagger}) \quad (1)$$

where the first term is the energy operator of free holes in the periodic field of the lattice. The second term is the energy operator of longitudinal acoustic phonons; the third term represents the hole–phonon interactions; and $a_{\mathbf{k}}^{\dagger}$, $a_{\mathbf{k}}$ are the creation and annihilation operators of the hole with a 3D quasi-wave vector \mathbf{k} and projections (k_x, k_y, k_z) . The energy of the hole $\varepsilon(\mathbf{k})$, measured from the band top is presented in the form

$$\varepsilon(\mathbf{k}) = -2w_1(1 - \cos k_x b) - 2w_2(1 - \cos k_y a) - 2w_3(1 - \cos k_z c) \quad (2)$$

where w_1 , w_2 and w_3 are the transfer energies of a hole from one molecule to another along the chain (x direction) and perpendicular to it (y and z directions). In Eq. (1), $b_{\mathbf{q}}^{\dagger}$, $b_{\mathbf{q}}$ are the creation and annihilation operators of an acoustic phonon with 3D wave vector \mathbf{q} and frequency $\omega_{\mathbf{q}}$. The Peierls transition occurs at low temperatures. In this case, the interaction of electrons with optical phonons can be neglected. It was shown in [10] that the spectrum of acoustic phonons of a simple one-dimensional chain is described by

$$\omega_{\mathbf{q}}^2 = \omega_1^2 \sin^2(q_x b / 2) + \omega_2^2 \sin^2(q_y a / 2) + \omega_3^2 \sin^2(q_z c / 2) \quad (3)$$

where ω_1 , ω_2 , and ω_3 are the limit frequencies in the x , y , and z directions. Two most important electron–phonon interaction mechanisms are considered: one of the deformation potential type and the other of the polaron type. The coupling constants of the first interaction are proportional to derivatives w'_1 , w'_2 and w'_3 of w_1 , w_2 , and w_3 with respect to the intermolecular distances. The coupling constant of the second interaction is proportional to the average polarizability of the molecule α_0 . This interaction is important for crystals composed of large molecules, such as TTT, so as α_0 is roughly proportional to the molecule volume.

The square module of matrix element $A(\mathbf{k}, \mathbf{q})$ from Eq. (1) can be written in the form

$$|A(\mathbf{k}, \mathbf{q})|^2 = 2\hbar w_1'^2 / (NM\omega_q) \times \{ [\sin(k_x b) - \sin(k_x - q_x, b) - \gamma_1 \sin(q_x b)]^2 + d_1^2 [\sin(k_y a) - \sin(k_y - q_y, a) - \gamma_2 \sin(q_y a)]^2 + d_2^2 [\sin(k_z c) - \sin(k_z - q_z, c) - \gamma_3 \sin(q_z c)]^2 \}. \quad (4)$$

Here, M is the mass of the molecule; N is the number of molecules in the basic region of the crystal; $d_1 = w_2 / w_1 = w_2' / w_1'$; $d_2 = w_3 / w_1 = w_3' / w_1'$; parameters γ_1 , γ_2 , and γ_3 describe the ratio of amplitudes of the polaron-type interaction to the deformation potential one in the x , y , and z directions:

$$\gamma_1 = 2e^2 \alpha_0 / b^5 w_1', \gamma_2 = 2e^2 \alpha_0 / a^5 w_2', \gamma_3 = 2e^2 \alpha_0 / c^5 w_3'. \quad (5)$$

In the reported results of experimentally measured longitudinal electrical conductivity of TTT_2I_3 crystals as a function of temperature, a sharp decrease in electrical conductivity for temperatures lower than $T_{\max} = 35$ K is observed [2]. Analysis shows that the Hamiltonian from Eq. (1) can not explain this behavior of the electrical conductivity. In addition, it is necessary to take into account the dynamical interaction of carriers with defects. The static interaction will contribute to the renormalization of the hole spectrum. The defects in TTT_2I_3 crystals are formed due to different coefficients of dilatation of the TTT and iodine chains. The Hamiltonian of this interaction H_{def} is presented in the form

$$H_{\text{def}} = \sum_{\mathbf{k}} \sum_{q, n=1}^{N_d} B(q_x) \exp(-iq_x x_n) a_{\mathbf{k}}^+ a_{\mathbf{k}-\mathbf{q}} (b_{\mathbf{q}} + b_{\mathbf{q}}^-). \quad (6)$$

Here, $B(q_x)$ is the matrix element of a hole interaction with a defect; it is presented as follows:

$$B(q_x) = \sqrt{\hbar / (2NM\omega_q)} \cdot I(q_x), \quad (7)$$

where $I(q_x)$ is the Fourier transformation of the derivative with respect to the intermolecular distance from the energy of interaction of a carrier with a defect, x_n numbers the defects, which are considered linear along the x -direction of the TTT chains and distributed randomly:

$$I(q_x) = D(\sin(bq_x))^2, \quad (8)$$

where constant $D = 1.03$; it determines the intensity of the hole interaction with a defect.

The renormalized phonon spectrum, $\Omega(\mathbf{q})$ is determined by the pole of the Green function and obtained from the transcendent dispersion equation

$$\Omega(\mathbf{q}) = \omega_q [1 - \bar{\Pi}(\mathbf{q}, \Omega)]^{1/2} \quad (9)$$

where the principal value of the dimensionless polarization operator takes the form

$$\text{Re} \bar{\Pi}(\mathbf{q}, \Omega) = -\frac{4}{\hbar \omega_q} \sum_{\mathbf{k}} \frac{[|A(\mathbf{k}, -\mathbf{q})|^2 + |B(q_x)|^2] (n_{\mathbf{k}} - n_{\mathbf{k}+\mathbf{q}})}{\varepsilon(\mathbf{k}) - \varepsilon(\mathbf{k} + \mathbf{q}) + \hbar \Omega} \quad (10)$$

Here, $n_{\mathbf{k}}$ is the Fermi distribution function. Equation (9) can be solved only numerically.

3. Results and Discussion

Numerical simulations for the 3D physical model of the crystal are performed for the following parameters [11]: $M = 6.5 \times 10^5 m_e$ (m_e is the mass of the free electron), $w_1 = 0.16$ eV, $w'_1 = 0.26$ eV·Å⁻¹, $d_1 = 0.015$, $d_2 = 0.015$, $\gamma_1 = 1.7$, γ_2 and γ_3 are determined from the following relationships: $\gamma_2 = \gamma_1 b^5 / a^5 d_1$ and $\gamma_3 = \gamma_1 b^5 / c^5 d_2$. The sound velocity along the TTT chains was estimated by comparison of the calculated results for the electrical conductivity of TTT₂I₃ crystals with the reported ones [2], $v_{s1} = 1.5 \times 10^5$ cm/s. For v_{s2} and v_{s3} in transversal directions (in the a direction and the c direction), we took 1.35×10^5 cm/s and 1.3×10^5 cm/s, respectively.

Figures 1–4 show dependences of renormalized phonon frequencies $\Omega(q_x)$ as a function of q_x for different temperatures and different of q_y and q_z values. The same figures show dependences for initial phonon frequency $\omega(q_x)$. It is evident that the $\Omega(q_x)$ values are diminished compared with those of $\omega(q_x)$ in the absence of the hole–phonon interaction. This means that the hole–phonon interaction and structural defects diminish the values of lattice elastic constants. In addition, one can observe that, with a decrease in temperature T , the curves change their form and a minimum appears in the $\Omega(q_x)$ dependences. This minimum becomes more pronounced at lower temperatures.

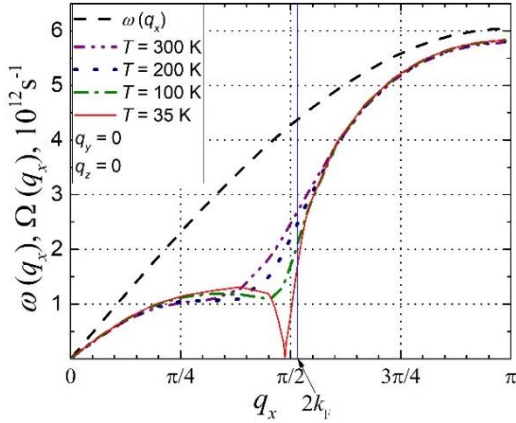


Fig. 1. Renormalized phonon spectrum $\Omega(q_x)$ for $\gamma_1 = 1.7$ and different temperatures. The dashed line is for the spectrum of free phonons. $k_F = 0.517\pi/2$.

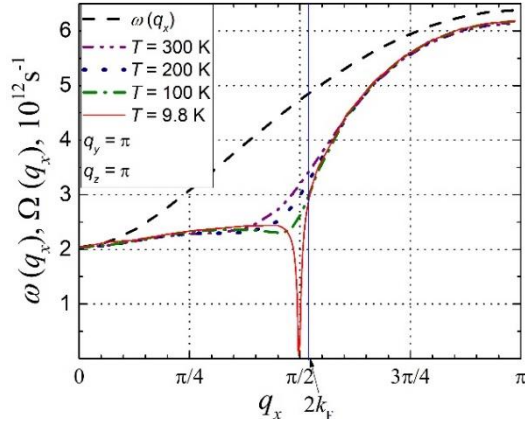


Fig. 2. Renormalized phonon spectrum $\Omega(q_x)$ for $\gamma_1 = 1.7$ and different temperatures. The dashed line is for the spectrum of free phonons. $k_F = 0.517\pi/2$.

Figures 1 and 2 were analyzed in detail in [9]. Figure 1 shows the case where $q_y = 0$ and $q_z = 0$ and dimensionless Fermi momentum $k_F = 0.517\pi/2$. In this case, the interaction between the TTT chains is neglected. The Peierls transition begins at $T = 35$ K. At this temperature, the electrical conductivity is significantly diminished, so as a gap in the carrier spectrum is fully opened just above the Fermi energy. In addition, it is evident that the slope of $\Omega(q_x)$ at low $\Omega(q_x)$ is diminished compared with that of $\omega(q_x)$. This means that the hole–phonon interaction and structural defects have reduced also the sound velocity in a wide temperature range. If the interaction between transversal chains is taken into account ($q_y \neq 0$ and $q_z \neq 0$), the temperature at $\Omega(q_x) = 0$ is diminished. This case is shown in Fig. 2 ($q_y = \pi$ and $q_z = \pi$) and $k_F = 0.517\pi/2$. It is

evident from the graph that the transition is completed at $T \sim 9.8$ K. According to [4], the electrical conductivity significantly decreases and achieves zero at $T \sim 10$ K. Thus, our calculations show that the transition is of the Peierls type and completed at this temperature.

Figure 3 shows the case where the Fermi momentum decreases and has a value of $k_F = (0.517\pi/2) - 0.018$. In Fig.3, the case where $q_y = 0$ and $q_z = 0$ is presented. It is evident that the Peierls transition begins at $T = 57$ K.

Figure 4 shows the case where the interaction between the TTT chains is taken into account ($q_y = \pi$ and $q_z = \pi$) and the Fermi momentum has the same value of $k_F = (0.517\pi/2) - 0.018$. It is evident that, at $\Omega(q_x) = 0$, the temperature decreases considerably, namely, to $T = 14$ K.

It was found that, with a decrease in the carrier concentration, T_p increases. For $k_F = 0.517\pi/2$, the transition begins at $T \sim 35$ K and is completed at $T \sim 9.8$ K. For $k_F = (0.517\pi/2) - 0.018$, the transition begins at $T \sim 57$ K at $q_y = 0$ and $q_z = 0$ and is completed at $T \sim 14$ K at $q_y = \pi$ and $q_z = \pi$.

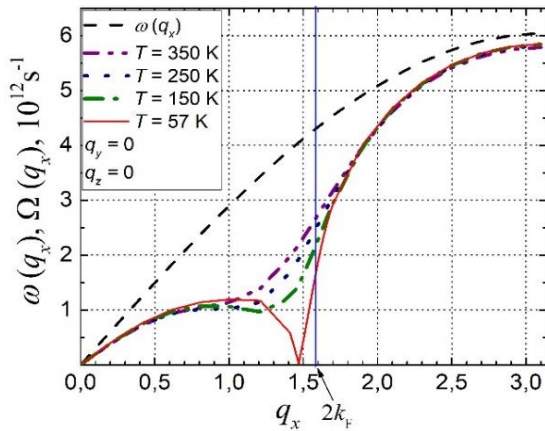


Fig. 3. Renormalized phonon spectrum $\Omega(q_x)$ for $\gamma_1 = 1.7$ and different temperatures. The dashed line is for the spectrum of free phonons.
 $k_F = (0.517 \pi/2) - 0.018$.

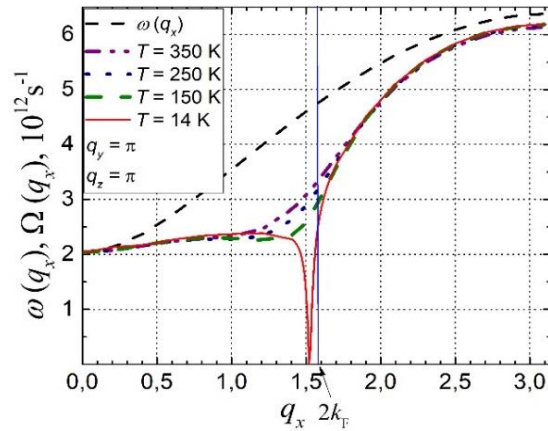


Fig. 4. Renormalized phonon spectrum $\Omega(q_x)$ for $\gamma_1 = 1.7$ and different temperatures. The dashed line is for the spectrum of free phonons.
 $k_F = (0.517 \pi/2) - 0.018$.

4. Conclusions

The dependence of the Peierls structural transition on carrier concentration in quasi-one-dimensional (Q1D) organic crystals of TTT_2I_3 is studied in the 3D approximation. A more complete crystal model is used; it takes into account two most important hole-phonon interactions. The interaction of holes with structural defects in the direction of the TTT chains is taken into account too. An analytical expression for the polarization operator is derived in the random phase approximation. The method of retarded temperature dependent Green function is applied. The numerical calculations for renormalized phonon spectrum $\Omega(q_x)$ for different temperatures are presented in two cases: (i) at $k_F = 0.517\pi/2$ and (ii) at a varying carrier concentration and $k_F = 0.517\pi/2 - \delta$, where δ is the variation in Fermi momentum k_F , which is determined by the decrease in the carrier concentration. It is found that, at $k_F = 0.517\pi/2$, the Peierls transition begins at $T \sim 35$ K in the TTT chains and considerably decreases the electrical

conductivity. Due to the interchain interaction, the transition is completed at $T \sim 9.8$ K. It is shown that the transition is of the Peierls type, so as at $T \sim 10$ K the electrical conductivity achieves zero. The hole–phonon interaction and the interactions with structural defects also diminish $\Omega(q_x)$ and reduce the sound velocity in a wide temperature range. It is observed that, with a decrease in carrier concentration, the Peierls critical temperature increases.

Acknowledgments. The authors express gratitude to the support of the scientific program of the Academy of Sciences of Moldova under project no. 14.02.116F.

References

- [1] I.I. Buravov, G.I. Zvereva, V.F. Kaminskii, et.al., Chem. Commun. 18, 720 (1976).
- [2] V.F. Kaminskii, M.I. Kidekel', Lyubovskii, et. al., Phys. Status Solidi A 44, 77 (1977).
- [3] B. Hilti and C.W. Mayer, Helv. Chim. Acta 61, 501 (1978).
- [4] L.G. Isset and E.A. Perz-Albuerene, Sol. State Comm., 21, 433 (1977).
- [5] L. N. Bulaevskii, Usp. Fiz. Nauk 115, 263 (1975).
- [6] M. Hohenadler, H. Fehske, and F.F. Assaad, Phys. Rev. B 83, 115105 (2011).
- [7] V. Solovyeva et al., J. Phys. D: Appl. Phys. 44, 385301 (2011).
- [8] S. Andronic and A. Casian, Adv. Mater. Phys. Chem. 7, 212 (2017).
- [9] S. Andronic, I. Balmus, and A. Casian, 9th Int. Conf. on Microelectronics and Computer Science, Chisinau, Republic of Moldova, October, 19–21, 2017.
- [10] A. Graja, Low-dimensional organic conductors, Singapore, Word Scientific, 1989.
- [11] A. Casian and I. Sanduleac, J. Electron. Mater. 43, 3740 (2014).

INVESTIGATION OF ORIENTATION MAGNETIC PHASE TRANSITION FOR USE IN ULTRAFAST OPTOMAGNETIC BISTABLE EFFECTS

S. A. Baranov^{1,2} and **I. I. Dobynde¹**

¹*Institute of Applied Physics, Academy of Sciences of Moldova, Academiei str. 5, Chisinau, MD-2028 Republic of Moldova
E-mail: baranov@phys.asm.md*

²*Shevchenko State University, str. 25 Oktyabrya 128, Tiraspol, Republic of Moldova*

(Received December 4, 2017)

Abstract

Theoretical results of a study of the magnetization orientation phase transition in magnetically ordered cylindrical nanoparticles are described. The hysteresis dependence of equilibrium magnetization orientation X on external parameter p is derived. This hysteresis can determine the region for the observation of optical bistability in the optomagnetic inverse Faraday effect.

1. Introduction

An ultrashort laser pulse (ULP) excites the spin precession in magnetically-ordered dielectrics, as stated in [1–3]. The spin-reorientation phase transition in orthoferrites can be induced by an ULP and the rise of time of this transition is a few picoseconds [1, 2].

The femtosecond magnetization dynamics of a thin cobalt film excited with ULPs was studied using two complementary pump-probe techniques, namely, spin-, energy-, and time-resolved photoemission and the time-resolved magneto-optical Kerr effect.

Combining the two methods, it is possible to identify the microscopic electron spin-flip mechanisms responsible for the ultrafast macroscopic magnetization dynamics of the cobalt film. In particular, the authors of [1, 2] show that electron–magnon excitation does not affect the overall magnetization even though it is an efficient spin-flip channel on the sub-200 fs time scale. Instead, we find an experimental evidence for the relevance of Elliott–Yafet-type spin-flip processes for the ultrafast demagnetization taking place on a time scale of 300 fs.

A typical experimental geometry is schematically shown in Fig. 1 (see [1–3]).

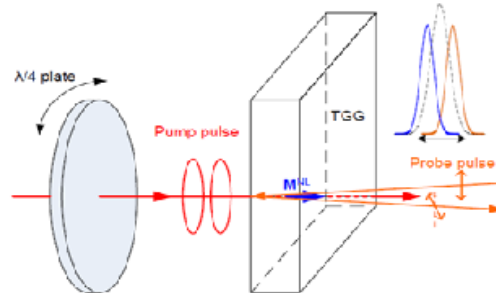


Fig. 1. Example of experimental geometry [1–3].

2. Model Cylindrical Nanoparticles and Calculation Method

The Landau–Lifshits equation-based description of the reorientation phase transitions dynamics was considered (see [4–7]):

$$\frac{dM}{dt} = -\gamma_0 M \times H_{\text{eff}} + \alpha M \times \frac{dM}{dt} \quad , \quad (1)$$

where M is the saturation magnetization, γ_0 is the gyromagnetic ratio, H_{eff} determined as a anisotropy field (about H_{eff} and free energy $F(\Psi)$, see below), and α is the Gilbert damping parameter.

A simple version of anisotropy energy is presented in the following form:

$$F_{em} = -\frac{3}{2} \lambda \sigma \cos^2(\psi - \psi_0) \quad . \quad (2)$$

Then, for magnetic permeability μ , the following could be obtained:

$$\mu = \left(\frac{3\lambda\sigma}{M^2} - N_{\Delta} \right)^{-1} \quad . \quad (3)$$

The above equation was derived in terms of the orientation phase transition theory.

However, in the case where F_{ms} and F_{em} compensate for each other, the expansion term F_{em} should be considered; it can be expressed in the following form:

$$F_2 = K_2 \cos^4(\psi - \psi_0) \quad . \quad (4)$$

The form of function F_2 for orientation change of phase in crystalloid magnetic depends on the type symmetry of the crystal; equation (4) corresponds to a hexagonal symmetry. The form of the above function for amorphous materials is not exactly known; therefore, further calculations of quality are only calculations of free energy and should also contain the F_H field term and have the following form:

$$F_H = -MH \cos \psi \quad (5)$$

and

$$F = F_{ms} + F_H + F_{em} + F_2 \quad . \quad (6)$$

Equilibrium orientation of magnetization is deducted from the solution for the equation obtained from the following:

$$\frac{\partial F}{\partial \psi} = 0 \quad \text{provided that} \quad \frac{\partial^2 F}{\partial^2 \psi} \geq 0 \quad . \quad (7)$$

For the relative magnetization along microwire axis $X = \cos \psi$, a numerical solution could be obtained. For quality assessment, the equation could be simplified if we assume that

$$F_{em} + F_{ms} = K_1 \cos^2(\psi - \psi_0) \quad , \quad (8)$$

and

$$F_2 = K_2 \cos^4 \psi \quad . \quad (9)$$

In the case where $\psi_0 \approx \pi/2$, the equation will acquire the following form:

$$4gX^3 + 2X + p = 0, \quad (10)$$

$$\text{where } g = \frac{K_2}{K_1} \text{ and } p = \frac{MH}{K_1}.$$

Parameter p characterizes the applied field, while parameter g characterizes the relation of the anisotropy constants, where the g value significantly increases near the “compensation” point due to the fact that K_1 tends to zero.

The generalized coordinate $\sin^2 \psi$ expansion was used for the free energy representation:

$$F = F_0 + K_1(T) \sin^2 \psi + K_2 \sin^4 \psi \quad (11)$$

The summand, which is proportional to the value of $\{H(t)M \sin \Psi\}$ and corresponds to the interreaction with the field, enters the F_0 term.

Parameter Ψ is the angle between the magnetization vector and the anisotropy axis and the external field $H(t)$.

In the elementary case, the direction of the $H(t)$ vector coincides with the axis of all anisotropies; coefficients $K_1(T)$ and K_2 are the scalar parameters of these anisotropies; a change in them initiates the onset of reorientation phase transitions.

3. Results and Discussion

Let us consider the following expansion of the free energy:

$$F = F_0 + K_1(T) \cos^2(\psi - \psi_0) + K_2 \cos^4 \psi \quad (12)$$

The free energy representation is attributed to the fact the anisotropy axes would be probably nonparallel to one another in the general case. Equilibrium magnetization orientation $X = \cos \psi$ is determined by expression (13):

$$\begin{aligned} & -16 \cdot g^2 \cdot X^8 + (16 \cdot g^2 - 16 \cdot p \cdot g \cdot \cos 2\psi_0) \cdot X^6 - 8 \cdot p \cdot g \cdot X^5 + \\ & + (16 \cdot p \cdot g \cdot \cos 2\psi_0 - 4) \cdot X^4 + (8 \cdot p \cdot g - 4 \cdot p \cdot \cos 2\psi_0) \cdot X^3 + (4 - p^2) \cdot X^2 + \\ & + 4 \cdot p \cdot \cos 2\psi_0 \cdot X + p^2 - \sin^2 2\psi_0 = 0 \end{aligned} \quad (13)$$

where $p = MH/K_1$ and $g = K_2/K_1$.

We derived the hysteresis dependence of the X value on external parameter p from expression (13) (see Figs. 2, 3).

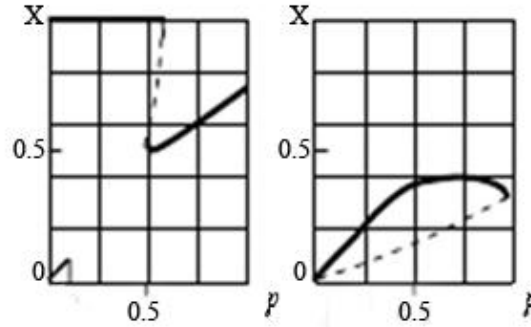


Fig. 2. Examples of numerical solutions for expression (13) for $g = 0.1$ and $g = -1$.

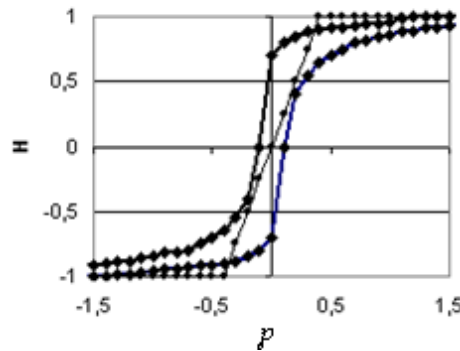


Fig. 3. Examples of numerical solutions for expression (13) for $g = -1$ and $\langle\langle K_2 \rangle\rangle = -100$.

4. Conclusions

It has been analytically shown that experimental data described in [1–3] can be interpreted as magnetization orientation phase transitions in magnetically ordered cylindrical nanoparticles [4–7]. This result can determine the region for the observation of optical bistability in the optomagnetic inverse Faraday effect [1, 2].

References

- [1] A.M. Kalashnikova, A.V. Kimel', and R.V. Pisarev, *Usp. Fiz. Nauk* 185, 1054 (2015).
- [2] A.V. Kimel and A.K. Zvezdin, *Low Temp. Phys.* 41, 878 (2015).
- [3] A.P. Pyatakov, A.S. Sergeev, E.P. Nikolaeva, T.B. Kosykh, A.V. Nikolaev, K.A. Zvezdin, and A.K. Zvezdin, *Usp. Fiz. Nauk* 185, 1078 (2015).
- [4] H. Horner and C.M. Varma, *Phys. Rev. Lett.* 20, 845 (1968).
- [5] L.D. Landau and E.M. Lifshits, *Elektrodinamika sploshnykh sred*, Nauka, Moscow, 1982.
- [6] K.P. Belov, A.K. Zvezdin, A.M. Kadomtsev, and R.Z. Levitin, *Usp. Fiz. Nauk* 119, 447 (1976).
- [7] V.G. Bar'yakhtar, A.N. Bogdanov, and D.A. Yablonskii, *Usp. Fiz. Nauk* 156, 47 (1988).

SYNCHRONIZATION OF CHAOTIC QUANTUM DOT LASERS WITH EXTERNAL FEEDBACK UNDER PARAMETER MISMATCH

T. Oloinic¹, S. S. Rusu^{1,2}, and V. Z. Tonciu¹

¹*Department of Physics, Technical University of Moldova, Stefan cel Mare Av. 168, Chisinau, MD-2004 Republic of Moldova*

²*Institute of Applied Physics, Academy of Sciences of Moldova, Academiei str. 5, Chisinau, MD-2028 Republic of Moldova
tatiana.oloinic@fiz.utm.md*

(Received July 30, 2018)

Abstract

This paper reports the numerical results on the synchronization features of a chaotic quantum dot semiconductor laser. The dynamic behavior is studied in terms of the Bloch equations model. Optimum conditions for chaotic operation are found. The synchronization of two unidirectional-coupled (master–slave) systems and the effect of parameter mismatch on the synchronization quality are studied.

1. Introduction

In the last decade, the synchronization of chaotic oscillators [1] has been the subject of different studies due to fundamental interest and applications in chaos-based communications systems [2, 3]. It is well known that semiconductor lasers subject to the influence of optical feedbacks are characterized by different dynamical behaviors, such as periodic and quasi-periodic pulsations, low frequency fluctuations, and coherent collapse. Typically, to achieve a chaotic behavior of conventional lasers with feedback from a distant mirror, a delay roundtrip time of at least a few nanoseconds is required. In this case, the mirror should be placed at a distance of a few tens of centimeters from the back facet of the laser. On the other hand, lasers with multisection external cavities can be suitable candidates for integrated chaotic emitters. Lasers subject to feedback from cavities with air gaps have been considered in the literature [4, 5]. In particular, feedback from a two-phase section was used to control the chaotic dynamics of semiconductor lasers with optical feedback. The dynamics of the system of a quantum dot laser with feedback proposed in this paper can be described by the Bloch equation model [6]. Thus, in this paper, we analyze the synchronization properties of two quantum dot lasers with multisection feedback coupled unidirectionally. The effect of parameter mismatch on the synchronization quality is studied.

The paper is structured as follows. We start in Section 2 by describing the laser setup and we introduce the model to describe the system dynamics. Section 3 presents a study of the dynamics of a laser under the action of multicavity feedback. Suitable conditions for the chaotic evolution of the output power system due to the influence of feedback are determined. The synchronization properties of two devices are presented. Finally, conclusions are given in Section 4.

2. Laser Model and Equations

Figure 1 shows the structure of a semiconductor laser with active medium quantum dots under the influence of feedback from equally distributed external cavities. We consider a single-mode DFB laser coupled to longitudinal multicavities. The first mirror is located at distance l from the laser facet, and the distance between mirrors is taken also l . The feedback part is composed by air-gap and phase sections. The phase sections are controlled by a small injected current. We assume that the injected current into the phase sections is small enough to change only the refractive index, i.e., the phase, so that the optical length of the resonator remains constant or is changed in the sub-wavelength range.

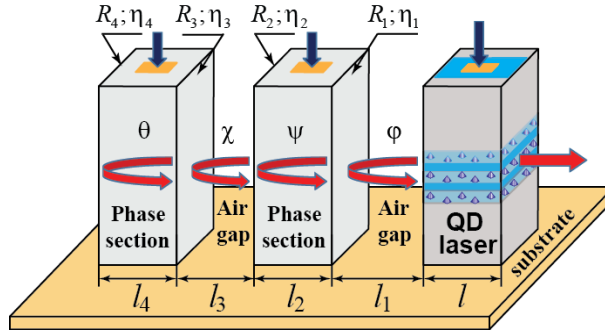


Fig. 1. Schematic view of a laser with a quantum dot active medium under the influence of multicavity external optical feedback. Phases ψ and θ are controlled by an injected current. R_1 and R_3 are the reflectivity of the air-material facet, respectively. R_2 and R_4 are the outer facet of the material cavity reflectivity, respectively.

The dynamical behavior of the system is described by the Bloch equations [6, 7]:

$$\frac{dE}{d\tau} = -kE + 2Z^{QD}\Gamma gP + \frac{Z^{QD}\Gamma\beta}{\tau_{eff}} E \left(\frac{D+1}{2} \right)^2 + \eta_1 e^{i\phi} E(\tau - \tau_1) + \eta_2 e^{i\psi} E(\tau - \tau_2) + \eta_3 e^{i\chi} E(\tau - \tau_3) + \eta_4 e^{i\theta} E(\tau - \tau_4) + \zeta E, \quad (1)$$

$$\frac{dP}{d\tau} = -\gamma P + gDE, \quad (2)$$

$$\frac{dD}{d\tau} = -4gEP + \frac{d_0 - D}{T_1} - \frac{1}{\tau_{eff}} \left(\frac{D+1}{2} \right)^2, \quad (3)$$

where E is the complex amplitude of the electric field, P is the polarization, and D is the inversion. These equations are used for master and slave lasers. k is the photon decay rate.

$g = \sqrt{\frac{G\gamma c_n}{2Z^{QD}\Gamma}}$ and β represent the coupling and spontaneous emission factors [6], where G is the gain and c_n as the speed of light in the laser medium; Z^{QD} is the number of quantum dots in the active region of the laser; Γ represents the confinement factor that characterizes the fraction of the quantum dots within the mode volume, which contribute to the laser emission; T_1 and d_0 are the inversion lifetime and pump strength; η_i are the feedback strengths governed by reflectivity R_i , respectively; ζ is the coupling strengths; τ_i are the external cavity round trips. The dimensionless parameters are $k = 300$, $Z^{QD} = 1000$, $\Gamma = 0.01$, $\beta = 1.0$, $d_0 = 0.95$, $\gamma = 100$,

$T_1 = 0.01$, $g = 48.86$, $\tau_{\text{eff}} = 0.001$, $\eta_1 = \eta_2 = \eta_3 = \eta_4 = 25$, $\zeta = 20$. These parameter values are used for the calculated results that are shown in all figures of the paper.

3. Results and Discussion

It is well known that the synchronization of two lasers can be quantified by measuring the cross-correlation coefficient, and the synchronization quality depends on the similarity between the master and slave lasers. As noted above, we focus here on the effect of the mismatch between different laser and material parameters on the synchronization features of two chaotic lasers coupled unidirectionally. Figure 2 shows the dependence of the cross-correlation coefficient on the phase difference (phase master – phase slave) for feedback strengths $\eta_i = 25$ and coupling strengths $\zeta = 20$. The other phases of passive sections are fixed.

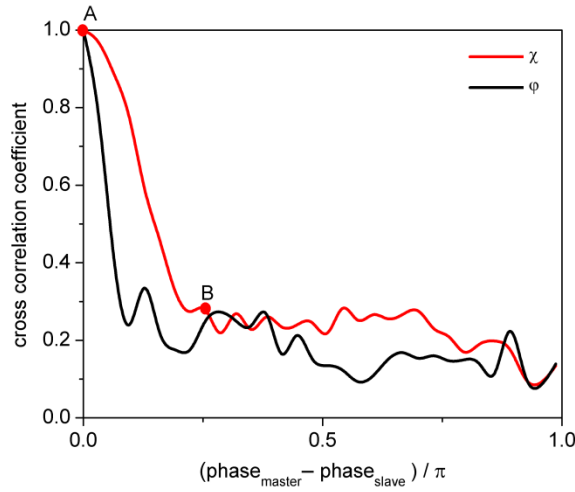


Fig. 2. Cross-correlation coefficient as a function of the feedback phase difference (phase master – phase slave) for coupling $\zeta = 20$. Parameters: $\varphi_s = 0$, $\psi_m = \psi_s = \pi/5$, $\chi_s = 0$, $\theta_m = \theta_s = \pi/4$.

The black line shows the degradation of the synchronization due to a mismatch of phase's φ of the master and slave lasers of the first air gap section. Phase φ_s of the slave laser is kept to zero, while phase φ_m of the master is varied from 0 to π . One can see the following conclusion. When the feedback phases coincide, the system shows perfect synchronization with a cross-correlation coefficient approaching unity (see point A in Fig. 2). An increase in the mismatch of the feedback phases induces a fast degradation of the synchronization, which is indicated by a reduction of the cross-correlation coefficient. This fast degradation is followed by the slowly one. The red line shows the effect of a mismatch in the second air-gap cavity feedback phase χ . We consider phase χ_s of the slave laser to be zero and vary phase χ_m of the master. As the mismatch is increased, the degradation is clearly less severe than for the case of mismatch in the feedback phase φ of the first air-gap. Thus, the phase of the shorter cavity is more sensitive to mismatch than that of long cavities.

Figure 3 shows the optical power time trace of the master (black) and slave (red) lasers and the synchronization diagrams for points A and B of Fig. 2, respectively. When the synchronization is perfect, the cross-correlation coefficient is close to unity $C = 0.995$ (see Fig. 3a). The synchronization map shows a clear synchronization process. Figure 3b shows the same dependences for point B, when the degradation of synchronization is observed and the

cross-correlation coefficient is $C = 0.3$. The trajectories of the master and slave lasers depart from each other and the synchronization map is a cloud of points showing the lack of correlation between outputs.

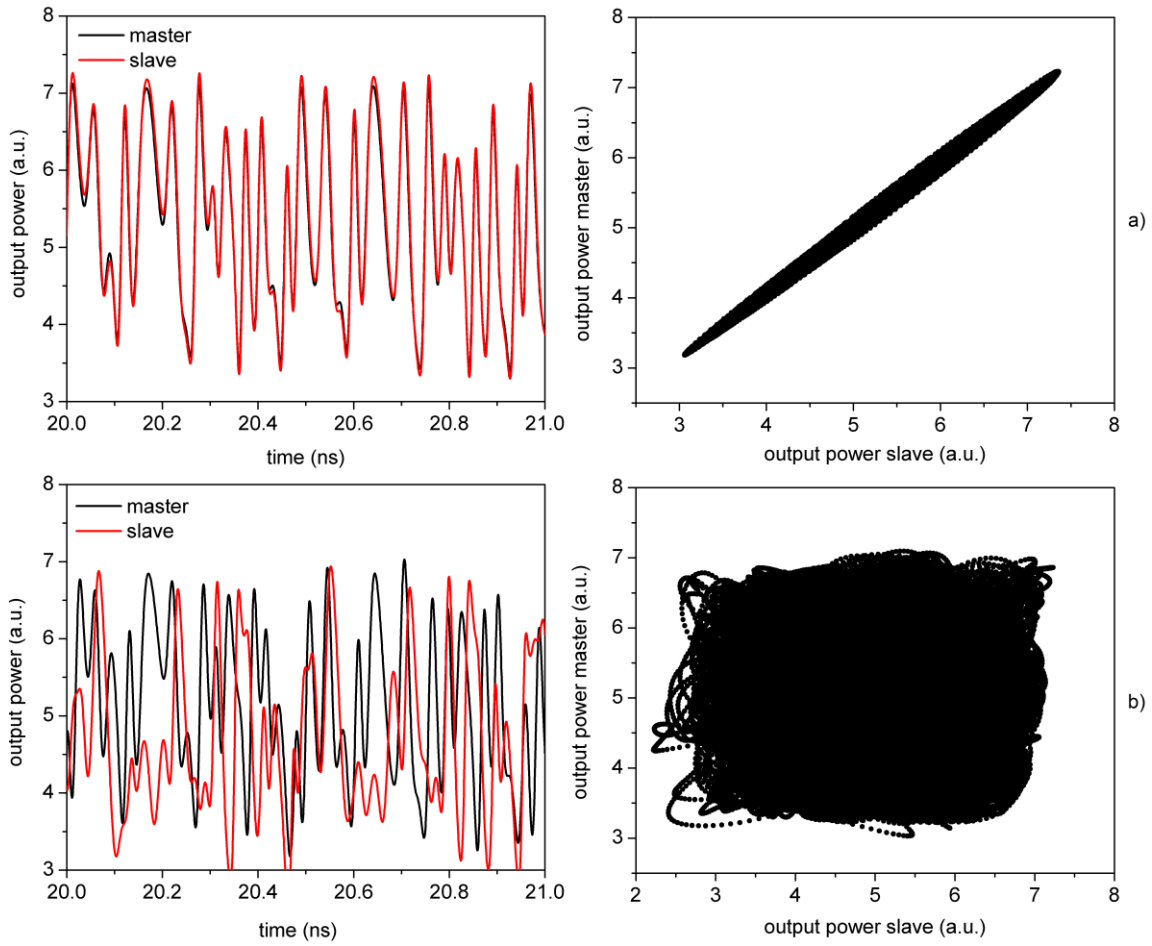


Fig. 3. Pulse traces of output power (left) and synchronization diagram (right) for points A (a) and B (b) of Fig 2. Parameters are the same as in Fig. 2.

Next, we study the effect of mismatch between other parameters on the synchronization performance of quantum dot lasers with feedback. Figure 4 shows the dependence of cross-correlation coefficient on mismatch between the difference of the gain (left) and the number of quantum dots (right) of the master and slave lasers. One can observe a higher degradation of synchronization in the case of gain mismatch compared with that of the number of quantum dots in active regions. This finding can be attributed to the fact that the difference in the number of quantum dots of the master and slave lasers leads only to a difference in the output power, but not in the high degradation of synchronization. However, note that the gain mutually depends on the number of quantum dots.

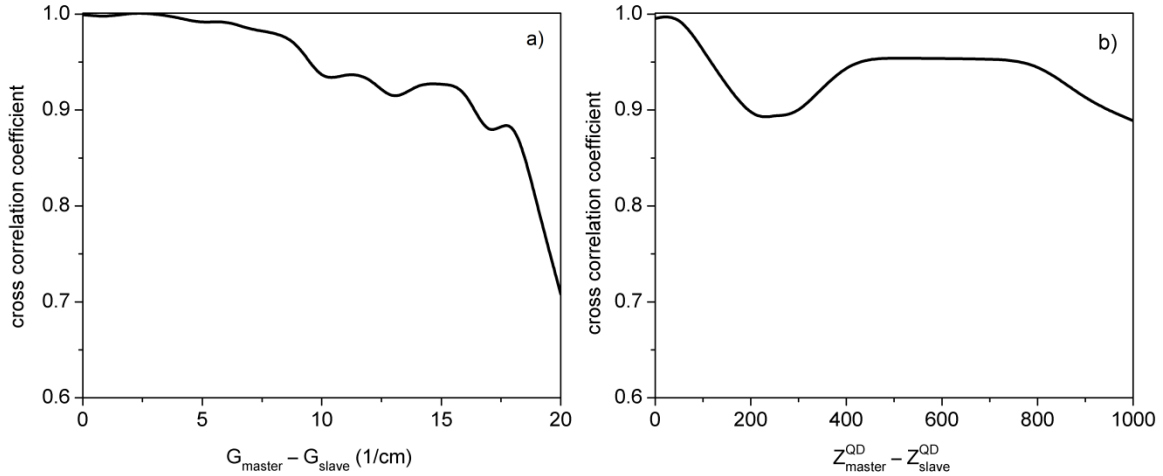


Fig. 4. Cross-correlation coefficient as a function of the difference of (a) the gain and (b) the number of quantum dots of the master and slave lasers. Parameters: $\varphi_s = \varphi_m = 0$, $\psi_m = \psi_s = \pi/5$, $\chi_m = \chi_s = 0$, $\theta_m = \theta_s = \pi/4$. The fixed value parameters for the slave laser are $G(\text{slave})=60$, $Z^{\text{QD}}(\text{slave}) = 1000$.

4. Conclusions

We have studied the synchronization properties of chaotic quantum dots laser under the influence of multisections optical feedback. The feedback implies a complex behavior keeping the device compact. A novel setup for the implementation of multiple feedbacks has been proposed. We have shown that two of these devices with equal parameters can be synchronized when they operate in the chaotic regime in a master–slave configuration, and the synchronization with higher cross correlation is achieved. However, synchronization is degraded when there is a mismatch in the material and device parameters of the master and slave lasers. It has been found that a mismatch in the first air gap feedback phase has stronger effects in the master–slave cross-correlation than a mismatch in the second air gap phase. In addition, it has been shown that the difference in the gain of the master and slave lasers leads to a degradation of synchronization. The number of quantum dots does not affect strongly the synchronization features of quantum dot lasers.

Finally, we believe that our work provides a good basis for future studies and, in particular, provides pointers for more detailed studies of synchronization of compact quantum dot lasers with feedback and their applications for chaos communication.

Acknowledgments. The authors acknowledge the financial support of the Technical University of Moldova (projects 14.02.116F/34S and 16. 80012.02.27F).

References

- [1]A. Pikovsky, M. Rosenblum, and K. Kurths, Synchronization: A Universal Concept in Nonlinear Sciences, Cambridge University Press, Cambridge, 2003.
- [2]A. Argyris, D. Syvridis, L. Larger, V. Annovazzi-Lodi, P. Colet, I. Fischer, J. García-Ojalvo, C.R. Mirasso, L. Pesquera, and A.L. Shore, Nature 438, 343 (2005).

- [3]C.R. Mirasso, P. Colet, and P. Garcia-Fernandez, *IEEE Photon. Technol. Lett.* 8, 299 (1996).
- [4]V.Z. Tronciu, C. Mirasso, P. Colet, M. Hamacher, M. Benedetti, V. Vercesi, and V. Annovazzi-Lodi, *IEEE J. Quantum Electron.* 46, 1840 (2010).
- [5]V.Z. Tronciu, C. Mirasso, and P. Colet, *J. Phys. B: At. Mol. Opt. Phys.* 41, 155401 (2008).
- [6]R. Aust, T. Kaul, C.-Z. Ning, B. Lingnau, and K. Ludge, *Opt. Quantum Electron.* 48, 109 (2016).
- [7]B. Lingnau, *Nonlinear and Nonequilibrium Dynamics of Quantum-Dot Optoelectronic Devices*, Doctoral Dissertation, Berlin, 230 p., (2015).

DETERMINATION OF CHARGE CARRIER SYSTEM PARAMETERS IN $\text{Pb}_{1-x}\text{Sn}_x\text{Te}$ BY JOINT ANALYSIS OF TEMPERATURE DEPENDENCES OF FOUR KINETIC COEFFICIENTS

D. Meglei and S. Alekseeva

*Gitsu Institute of Electronic Engineering and Nanotechnologies,
Academy of Sciences of Moldova, Academiei str. 3/3, Chisinau, MD-2028 Republic of Moldova
E-mail: alexeeva @nano.asm.md*

(Received November 8, 2018)

Abstract

The temperature dependences of electrical conductivity (σ), Hall coefficient (R), thermopower (α), and Nernst–Ettingshausen coefficient (Q) for five $\text{Pb}_{0.82}\text{Sn}_{0.18}\text{Te}$ samples with different charge carrier concentrations in a temperature range of 100–300 K have been studied. According to the obtained experimental data, the temperature dependences of the mobility and the effective scattering parameter have been calculated. The main features of the experimental data can be interpreted in terms of a two-band model of the valence band structure with several groups of holes involved in the transport phenomena. It has been found that the behavior of the temperature dependence of the effective scattering parameter significantly depends on the charge carrier concentration. The determined quantitative values of the effective scattering parameter are consistent with the concepts of a mixed scattering mechanism.

1. Introduction

Semiconductor materials of $\text{Pb}_{1-x}\text{Sn}_x\text{Te}$ solid solutions are commonly used in two main fields of solid-state electronics, namely, infrared optoelectronic devices and thermoelectric converters. The most interesting property of $\text{Pb}_{1-x}\text{Sn}_x\text{Te}$ is the ability to control the band gap by changing the chemical composition without a significant change in the crystal structure. In addition, lead chalcogenides are topological insulators; that is, they are representatives of the subclass of narrow-gap semiconductors that act as insulators in the bulk of the material and exhibit metallic conductivity on the surface.

The scientific interest in these materials is primarily associated with their unusual galvanomagnetic, thermomagnetic, and magneto-optic properties.

The solid solution of lead telluride and tin— $\text{Pb}_{1-x}\text{Sn}_x\text{Te}$ —is a narrow-gap semiconductor. The band gap of a narrow-gap solid solution is determined by the composition of the solution (x value). At $x = 0.18$, at helium temperatures, the band gap E_g of $\text{Pb}_{1-x}\text{Sn}_x\text{Te}$ is about 0.05 eV.

The absolute extremes of the conduction and valence bands of $\text{Pb}_{1-x}\text{Sn}_x\text{Te}$ are located at the L point at the boundary of the Brillouin zone. In addition, the valence band of the $\text{Pb}_{1-x}\text{Sn}_x\text{Te}$ solid solutions is composed of a group of light and heavy holes.

2. Results and Discussion

To obtain reliable experimental results, severe requirements are imposed on the quality of the samples under study: the volume distribution of the components should be uniform, while the amount of mechanical defects should be reduced to minimum. The most effective method for synthesizing homogeneous $\text{Pb}_{1-x}\text{Sn}_x\text{Te}$ single crystals is the gas-phase growth technique.

Experimental studies of transport phenomena in semiconductors provide the most complete information about the kinetics of charge carriers and their energy spectrum with a wide variation in the concentration of charge carriers and impurities and in temperature.

A comprehensive study of the thermopower, electrical conductivity, Hall coefficient, and Nernst–Ettingshausen coefficient (NEC) of the same samples by a joint analysis makes it possible to determine the charge carrier parameters.

In this study, $\text{Pb}_{0.82}\text{Sn}_{0.18}\text{Te}$ single crystals were synthesized by the gas-phase growth technique. Microstructural and spectral studies and measurements of the Hall coefficient confirmed the high quality of the synthesized single crystals.

Temperature dependences of the kinetic coefficients (thermopower, electrical conductivity, Hall coefficient, and transverse NEC) of the synthesized $\text{Pb}_{0.82}\text{Sn}_{0.18}\text{Te}$ single crystals with a charge carrier concentration of 10^{16} to 10^{19} cm^{-3} in a temperature range of 80–400 K were studied.

In our previous reports [1, 2], the temperature dependences of thermopower, electrical conductivity, and Hall coefficient were characterized. The temperature studies of electrical conductivity σ , thermopower α , Hall coefficient R , and NEC Q were conducted according to standard procedures.

Measurements of four main kinematic coefficients (σ , R , α , Q) make it possible to determine the main characteristics of a semiconductor material, particularly the effective scattering parameter of charge carriers r_{eff} (exponent in the dependence of the mean free path of the carriers on energy $l \sim \epsilon^r$). The effective scattering parameter of carriers r_{eff} can be calculated by the following formula [3–5]:

$$\frac{Q}{R\sigma\alpha} = \frac{r_{\text{eff}} - 0,5}{r_{\text{eff}} + 1} \quad (1)$$

where R is the Hall coefficient, σ is the electrical conductivity, α is the Seebeck coefficient, and Q is the NEC.

Figure 1 shows temperature dependences of the NEC of the $\text{Pb}_{0.82}\text{Sn}_{0.18}\text{Te}$ samples with different charge carrier concentrations. The temperature dependences of the samples shown in Fig. 1 are nonmonotonic and exhibit a maximum. At low temperatures, the NEC is minimal; with an increase in temperature, it achieves a maximum value and then decreases. An exception is provided by sample 5 (not shown in the figure) with a minimum hole concentration of 10^{16} cm^{-3} ; at low temperatures, the NEC of this sample is maximal and abruptly decreases with increasing temperature. The positive sign of all the NECs suggests that the optical phonon scattering of charge carriers is dominant.

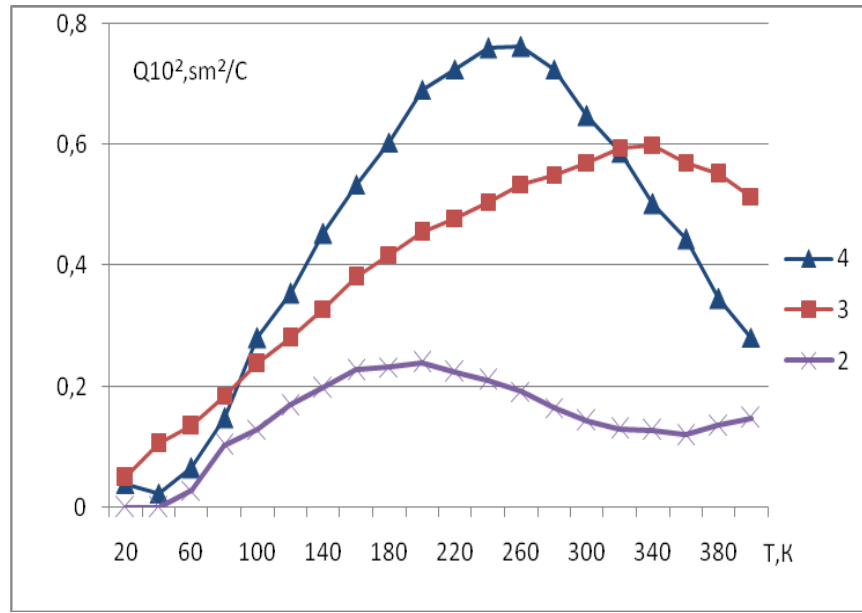


Fig. 1. Temperature dependence of the NEC of the $\text{Pb}_{0.82}\text{Sn}_{0.18}\text{Te}$ samples with different charge carrier concentrations: (2) 15×10^{17} , (3) 5.2×10^{17} , and (4) $2.6 \times 10^{17} \text{ cm}^{-3}$.

The experimental temperature dependences of the Hall coefficient and electrical conductivity of $\text{Pb}_{0.82}\text{Sn}_{0.18}\text{Te}$ with different charge carrier concentrations are shown in Figs. 2 and 3.

The temperature dependences of the samples shown in Figs. 2 and 3 are nonmonotonic and exhibit a maximum.

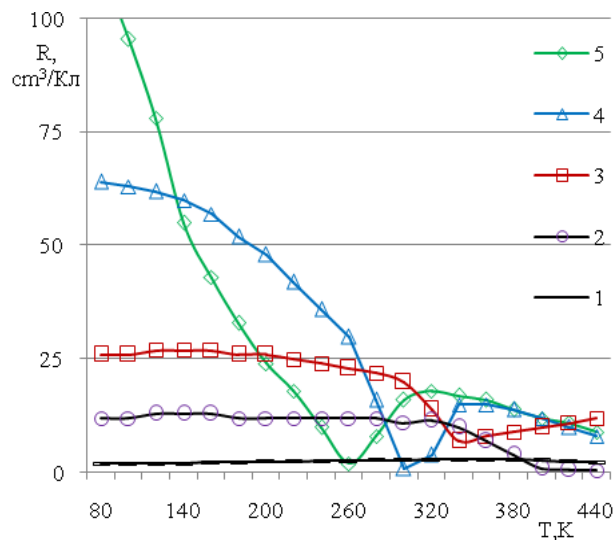


Fig. 2. Temperature dependence of the Hall coefficients of the $\text{Pb}_{0.82}\text{Sn}_{0.18}\text{Te}$ samples with different charge carrier concentrations: (1) 200×10^{17} , (2) 15×10^{17} , (3) 5.2×10^{17} , (4) 2.6×10^{17} , and (5) $0.52 \times 10^{17} \text{ cm}^{-3}$.

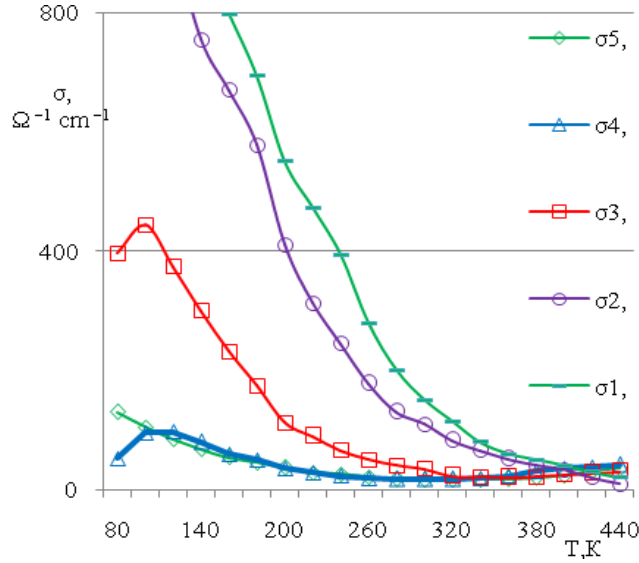


Fig. 3. Temperature dependence of the electrical conductivity of the $\text{Pb}_{0.82}\text{Sn}_{0.18}\text{Te}$ samples with different charge carrier concentrations: (1) 200×10^{17} , (2) 15×10^{17} , (3) 5.2×10^{17} , (4) 2.6×10^{17} , and (5) $0.52 \times 10^{17} \text{ cm}^{-3}$.

Figure 4 shows temperature dependences of the thermopower of $\text{Pb}_{1-x}\text{Sn}_x\text{Te}$ ($x = 0.18$) with different charge carrier concentrations. For the samples with a low charge carrier concentration, the thermopower sign inversion is observed; this finding indicates the transition to the intrinsic conductivity region (curves 4, 5). For the samples with a lower charge carrier concentration, the thermopower sign inversion is observed at lower temperatures.

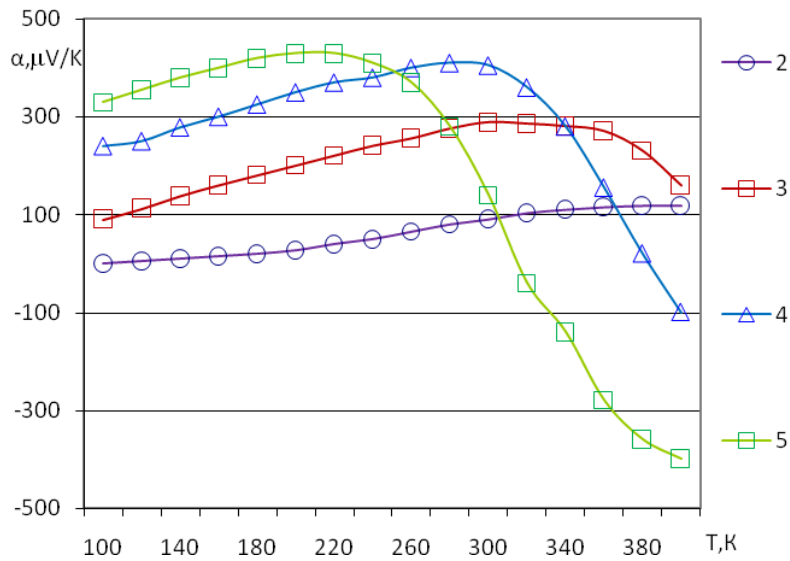


Fig. 4. Temperature dependence of the thermopower of the $\text{Pb}_{0.82}\text{Sn}_{0.18}\text{Te}$ samples with different charge carrier concentrations: (2) 15×10^{17} , (3) 5.2×10^{17} , (4) 2.6×10^{17} , and (5) $0.52 \times 10^{17} \text{ cm}^{-3}$.

To interpret the obtained experimental data, the two-band Gottwick's model with a linear temperature term was used [6–9]. In this approximation, it is assumed that the Lorentzian resonance occurs in the vicinity of the Fermi surface. This model makes it possible to determine the Fermi energy and the position and width of the resonance using experimental data. Parameters E_0 and G are determined by the position of the center and the width of the resonance on the energy axis, respectively.

According to the data shown in Figs. 1–4, the temperature dependences of effective scattering parameter r_{eff} can be calculated by formula (1).

Temperature dependences of the effective scattering parameter r_{eff} of the $\text{Pb}_{0.82}\text{Sn}_{0.18}\text{Te}$ samples with different charge carrier concentrations are shown in Figs. 5 and 6. It is evident from the figures that the behavior of the temperature dependence of the effective scattering parameter significantly depends on the charge carrier concentration.

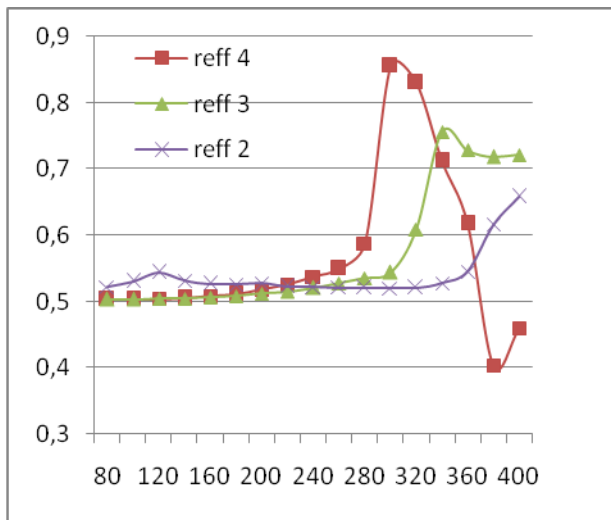


Fig. 5. Temperature dependence of the effective scattering parameter r_{eff} of the $\text{Pb}_{0.82}\text{Sn}_{0.18}\text{Te}$ samples with different charge carrier concentrations: (2) 15×10^{17} , (3) 5.2×10^{17} , and (4) $2.6 \times 10^{17} \text{ cm}^{-3}$.

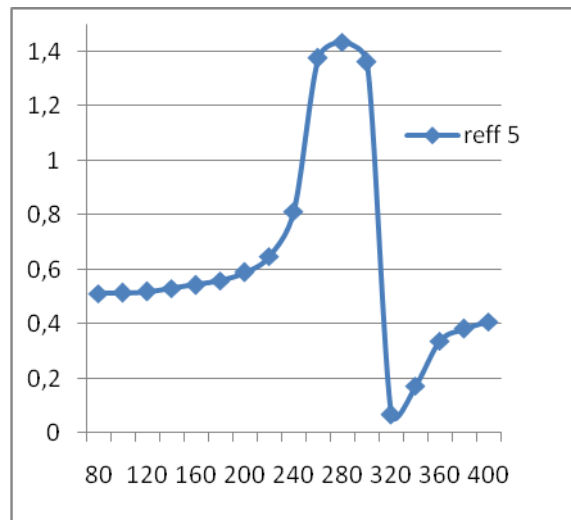


Fig. 6. Temperature dependence of the effective scattering parameter r_{eff} of the $\text{Pb}_{0.82}\text{Sn}_{0.18}\text{Te}$ sample with a charge carrier concentration of $5.2 \times 10^{16} \text{ cm}^{-3}$.

It is reasonable to expect that, in addition to acoustic phonon scattering, possible scattering mechanisms will be Coulomb potential scattering of ionized impurities and defects and optical phonon scattering [10].

All the samples are characterized by the following feature: the effective scattering parameter increases with increasing temperature and abruptly decreases upon the achievement of a maximum. For temperatures in a region of 80–250 K, the r_{eff} value is about 0.5; this finding can be attributed to optical phonon scattering. The determined quantitative values of the effective scattering parameter at temperatures above 250 K are consistent with the concepts of a mixed scattering mechanism.

References

- [1] D. Meglei and S. Alekseeva, *Mold. J. Phys. Sci.* 13 (1–2), 20 (2014).
- [2] D. Meglei and S. Alekseeva, *Mold. J. Phys. Sci.* 15 (3–4), 134 (2016).
- [3] S.A. Nemov, N.M. Blagikh, A. Allakhhakh, and L.D. Ivanova, *Fiz. Tekh. Poluprovodn.* 49, 1346 (2015).
- [4] S.A. Nemov, N.M. Blagikh, A. Allakhhakh, L.D. Ivanova, M.B. Dzhafarov, and A.E. Demchenko, *Fiz. Tverd. Tela* 58, 2208 (2016).
- [5] V.E. Gasumyants, O.A. Martynova, and R.M. Dubrovin, *Fiz. Tverd. Tela* 57, 2293 (2015).
- [6] U. Gottwick, K. Gloss, S. Horn, E. Steglich, and A. Grewe, *J. Magn. Magn. Mater.* 47–48, 536 (1985).
- [7] Sh.R. Ghorbani, Stockholm Doctoral Dissertation, Royal Institute of Technology Solid State Physics, Department of Physics & IMIT, 2002.
https://www.researchgate.net/profile/S_Ghorbani/publication/267389946_Structural_and_Electrical_Transport_Properties_of_Doped_Nd-123_Superconductors/links/54cf6bb50cf298d656636e70/Structural-and-Electrical-Transport-Properties-of-Doped-Nd-123-Superconductors.pdf
- [8] S.S. Ragimov and I.N. Askerzade, *Zh. Tekh. Fiz.* 80 (10), 150 (2010).
- [9] O.S. Komarova and V.E. Gasumyants, *Fiz. Tverd. Tela*, 52 (4), 625 (2010).
- [10] B.M. Askerov, *Kineticheskie yavleniya v poluprovodnikakh*, Nauka, Leningrad, 1970.

STRAIN INFLUENCE ON THE DIFFUSION THERMOPOWER IN Bi WIRES

E. Condrea

*Ghitu Institute of Electronic Engineering and Nanotechnologies, Academiei str. 3/3, Chisinau,
MD-2028 Republic of Moldova
E-mail: condrea@nano.asm.md*

(Received November 21, 2018)

Abstract

We present the results of studies of the thermopower in glass-coated Bi wires under the action of uniaxial deformation. At the liquid helium temperature, thin Bi wires exhibit large positive thermopower values, which are dominated by the diffusive transport mechanism of holes. The observed increase in the negative contribution to total thermopower under uniaxial strain testifies that the hole-dominated transport can be transformed into the electron-dominated transport. The observed trend to negative thermopower values under strain can be attributed partially to a slight increase in the electron mobility and partially to the occurrence of the phonon drag effect of electrons. The phonon drag effect prevails in the thermopower, if the phonons acquire a sufficient momentum to scatter the carriers across the Fermi surface changed after an Electronic Topological Transition.

1. Introduction

Currently, metallic and semimetallic wires are widely used as building elements in a variety of nanodevices. The emergence of studies concerned with the transport properties of Bi wires is motivated partially by the interesting thermoelectric and magnetotransport properties of bismuth nanowires (NWs), which make them potentially useful for device applications [1–4].

The prospect of the thermoelectric application of the wires will require the possibility of controlling their parameters. In this context, Bi wires embedded in an individual glass capillary allow us to perform measurements of thermoelectric parameters in wide ranges of temperatures and elastic strains. It is well known that the total thermopower (TEP), which is also referred to as the Seebeck coefficient (S), of bulk bismuth samples at the liquid helium temperature is the sum of the diffusion (S_d) and phonon drag terms (S_g):

$$S = S_d + S_g. \quad (1)$$

Systematic measurements of a set of bulk Bi samples with different sizes have shown the changes in the magnitude of phonon drag thermopower with a moderate variation in the size of the samples [5–8]. As concerns low-dimensional Bi samples, such as films, whiskers, and wires, there is a larger spread in the thermopower measurements. In addition, a severe discrepancy was observed between experimental results for Bi wires with identical diameters obtained by different technological methods [9–13] (see table).

In different cases of positive S , which indicate the p -type transport for Bi NW composites [10] and for individual polycrystalline NWs [3] or negative S of Bi/Al₂O₃ arrays [11], the authors suggest that uncontrolled impurities can easily affect the value and sign of S .

In general, in bulk Bi crystals oriented along the bisectrix axis, an intrinsically negative phonon drag contribution is dominant in the TEP at low temperatures [6, 7]. Our previous studies of individual glass-coated Bi wires oriented along the bisectrix axis revealed a large positive thermopower dominated by the diffusion effect [14]. The diffusive origin of the TEP was attributed to structural imperfections, which strongly diminish the phonon–electron contribution to the total TEP. The suppression of the electron contribution to TEP was attributed to a mechanism based on the model of selective carrier scattering by potential barriers, which was advanced by Ravich [15]. Some significant changes in the quality and parameters of Bi wires can be obtained using different external impacts, such as the electric field effect, deformation, and magnetic field.

Thermopower discrepancy observed between experimental results for Bi wires obtained by different technological methods

| Technological methods | Thermopower (TEP) | | Temperatures (T) K |
|--|---|-----------------------|------------------------|
| | carrier dominated transport (d is diameter, nm) | | |
| | positive (p -type) | negative (n -type) | |
| glass-coated Bi Nws ⁹ | $d < 800$ | $d > 800$ | 77 |
| Bi NWs ¹⁰ and composites ¹¹ embedded in porous anodic alumina (Bi/Al ₂ O ₃) | positive | | below 30 |
| | | negative | above 30 |
| | | $d = 40$ and 65 | 4.2–300 |

The goal of this work is to study the changes revealed in the TEP behavior under the action of uniaxial deformation at low temperatures. To draw detailed information on how the diffusive and phonon drag terms of TEP vary with strain, we measured the temperature dependences of thermopower $S(T)$ at various values of applied strain. The critical value of the uniaxial strain when the phonon drag effect becomes predominant in the total TEP was determined.

2. Results and Discussion

The studied single-crystalline Bi wires were obtained by the glass-coated melt spinning method [16]. The axis of the prepared wires is oriented at an angle of about 19° to the C_1 bisector axis in the bisector–trigonal plane.

Experimental procedure and methods are presented in detail in our previous papers concerning the galvanomagnetic properties of Bi wires [14, 17]. In this paper, we discuss the results of the thermopower measurements extended in a temperature range of 4.2–50 K and focus on the explanation of the unusual behavior of TEP at a high value of uniaxial strain.

The measured temperature dependences of the thermopower for wires with diameters of 100–350 nm exhibit a nearly linear behavior with a positive slope in a temperature range of 5–20 K (Fig. 1a, curves 1–3). Considering the quasi-linear dependence of $S(T)$, the observed TEP was

associated with the diffusion transport mechanism. According to [14], the diffusive origin of the TEP was attributed to the limited diameter and structural imperfections within the nanowire, which strongly diminish the contribution from electrons or from the phonon–electron interaction to the total thermopower. The suppression of the electron contribution to TEP was attributed to a mechanism based on the model of selective carrier scattering by potential barriers, where the electrons are scattered much stronger than holes, which eventually affects the electron mobility: $\mu_e < \mu_h$ [15]. The predominance of the phonon drag term was observed for the thicker wires with $d > 600$ nm (Fig. 2). This finding can be attributed to an increase in the electron to hole mobility ratio, which in turn can be associated either with a diminished effect of the surface scattering of electrons (due to an increase in the wire diameter) or with a decrease in the concentration of structural imperfections (due to technological conditions in the preparation of thicker wires).

In the continuation of the studies of the strained Bi wires, the dependences of thermopower on strain ($0 \leq \varepsilon \leq 3\%$) and temperature ($4.2 \text{ K} \leq T \leq 300 \text{ K}$) were measured. Note that an increase in the contribution of electrons to TEP up to a sign change from positive to negative was observed in our earlier studies on Bi wires under a uniaxial strain [17]. The TEP dependences on strain are fairly different for thinner and thicker wires in the studied range of diameters (Fig. 1).

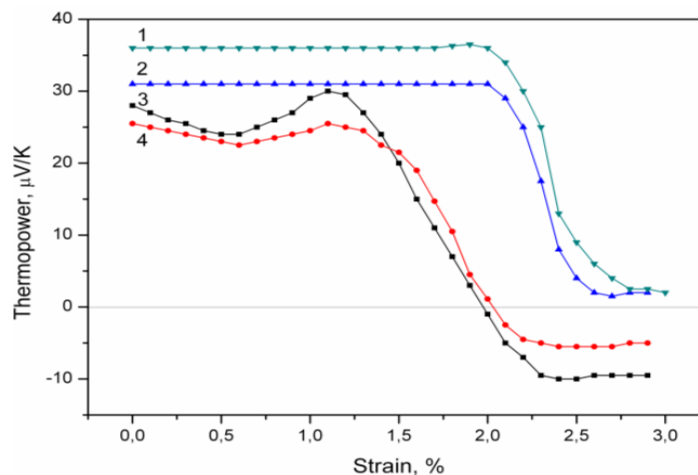


Fig. 1. Strain dependence of TEP for Bi wires of different diameters at 4.2 K: (1) 2.4, (2) 1.0, (3) 0.18, and (4) 0.35 μm .

Two types of behavior for two sets of samples were revealed: the first type for NWs with diameters $0.1 \leq d \leq 0.35 \mu\text{m}$ and the second type for wires with $0.35 < d < 3.0 \mu\text{m}$. The application of strain upon the wires of the second type ($d > 0.35 \mu\text{m}$) does not produce any variation in the $S(\varepsilon)$ dependence up to a strong deformation (Fig.1, curves 1, 2). Only above $\varepsilon = 2.0\%$, the $S(\varepsilon)$ decreases and trends to zero. The second type of behavior is developed for the wires when the phonon drag contribution is dominant in the total TEP. In the case of the first type wires ($d \leq 0.35 \mu\text{m}$), the $S(\varepsilon)$ dependences exhibit a nonmonotonous behavior, which indicates a complex charge transport mechanism (Fig. 1, curve 3, 4). The initial positive TEP smoothly decreases, goes through fine minima, and increases up to a peak around strain of 1.1% with the subsequent sharp decrease, a change in sign, and the nearly saturation behavior under a higher strain. Note that a nonmonotonous behavior is inherent in the wires in which TEP is dominated by the diffusion transport mechanism. This complex behavior is representative of a competition

among the different scattering mechanisms for the carriers and balances between the diffusive transport of electron or hole parts of the Fermi surface that changed during straining. The emergence of a peak on $S(\varepsilon)$ around $\varepsilon \approx 1.1\%$ (Fig. 1, curve 3, 4) is indicative of a change in the Fermi surface topology under strain known as the Electronic Topological Transition (ETT), or the Lifshitz transition.

Analyzing the nonmonotonous behavior of $S(\varepsilon)$ (Fig. 1, curves 3, 4) under a strain higher than the ETT point ($\varepsilon \geq 1.1\%$), we observed a sharp decrease in TEP and the sign change from positive to negative. Taking into consideration some predicted anomalies arising in the phonon spectrum for the materials undergoing an ETT of the Fermi surface [18], we can suppose that the increase in the negative contribution to TEP is attributed to the occurrence of the phonon drag effect of electrons under strain. The phonon drag effect prevails in the TEP, if the phonons acquire a sufficient momentum to scatter the carriers across the Fermi surface changed after the ETT.

To draw more detailed information on how the diffusive and phonon drag terms of TEP vary with strain, we measured the temperature dependences of thermopower $S(T)$ at various values of applied strain. Figure 4 shows the temperature dependences of TEP from the nondeformed state (curve *a*) up to maximal strain (curve *g*).

A quasi-linear $S(T)$ dependence for thermopower in the nondeformed state persistent up to a strain of $\varepsilon \approx 1.1\%$ indicates the diffusive origin of it (Fig. 4, curves 1–3). The temperature dependence of thermopower measured after an ETT in the region of the abrupt drop of $S(\varepsilon)$ develops into a nonlinear dependence. The observed nonlinear dependence with a negative temperature coefficient ($\partial S/\partial T < 0$) indicates the dominance of the phonon drag effect in a narrow temperature range of 5–18 K (Fig. 4, curve 4). In correlation with the predictions made in [18], the phonon drag effect becomes dominant in the thermopower if the phonon momentum is sufficient for interacting of the phonons with the electrons after an ETT.

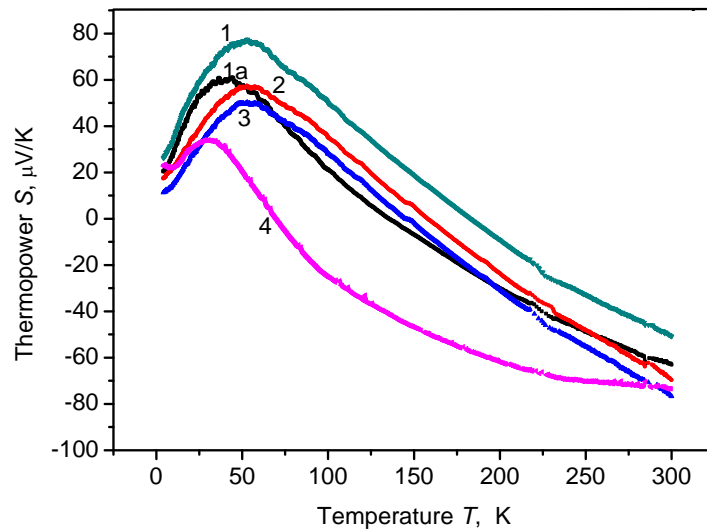


Fig. 2. Temperature dependences of the thermopower for as-prepared and thermally annealed Bi wires of various diameters: (1) 120 nm (as-prepared); (1a) 120 nm (after thermal treatment); (2) 250 nm; (3) 350 nm; and (4) 650 nm.

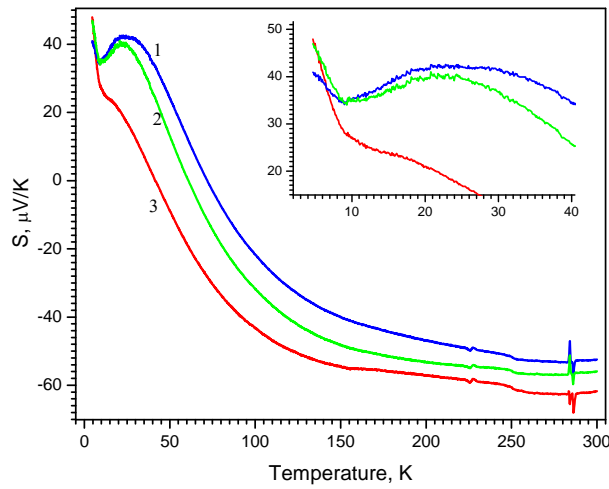


Fig. 3. Temperature dependences of the thermopower for second type of Bi wires when the phonon drag contribution is dominant in the total TEP for various diameters: (1) 0.8, (2) 1.1, and (3) 3.0 μm . Inset (b): expanded version of $S(T)$ dependences in a temperature range of 4.2–20 K.

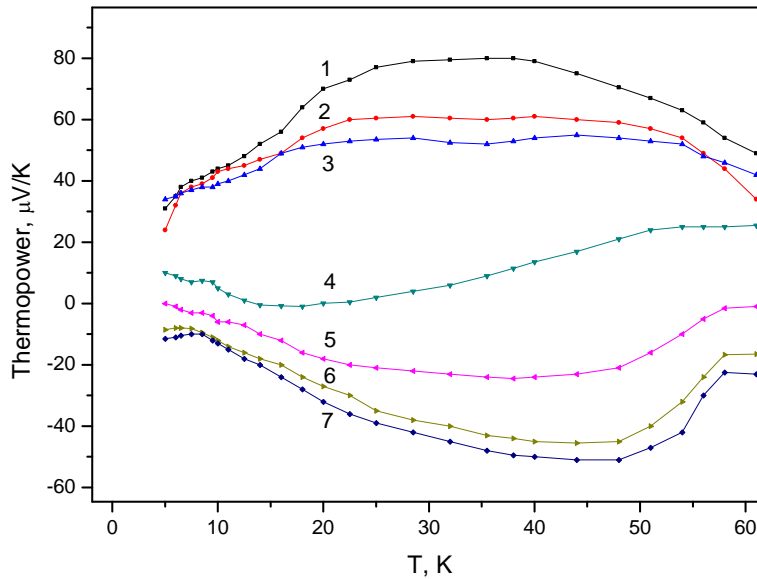


Fig. 4. Temperature dependence of thermopower of the 300-nm Bi wire at various strain values (1) 0, (2) 0.6, (3) 1, (4) 1.6, (5) 1.9, (6) 2.2, and (7) 7 %.

The increase in negative contribution under strain to the total TEP (equation (1)) suggests that a phonon drag term with a negative sign is added to the initial positive diffusion term. The predominance of the phonon drag effect of electrons implies that required condition $q \leq 2k_F$ (q is the phonon momentum, $2k_F$ is the maximum dimension of Fermi surface) for the phonons

interacting with a certain type of charge carriers is satisfied for electrons after an ETT in the region of the abrupt drop of $S(T)$.

Some information on the Fermi momentum p_F of the electrons was provided by the set of curves of the LMR measurements under different strains. In accordance with the galvanic magnetic size effect theory, the extreme p_F value of the electrons in the plane perpendicular to the magnetic field was determined in the nondeformed state and at a strain value of $\varepsilon \approx 1\%$: p_F ($\varepsilon = 0\%$) = 1.1×10^{-21} g cm s⁻¹ and p_F ($\varepsilon \approx 1\%$) = 1.25×10^{-21} g cm s⁻¹. These rough estimates indicate an increase in p_F of heavy electrons, which can contribute to the phonon drag effect.

After the change in the sign of the TEP, a further increase in strain does not have an obvious effect on the $S(\varepsilon)$ dependence under a higher strain (i.e., a nearly saturation behavior above $\varepsilon \geq 2\%$ in curves 3, 4 in Fig. 1); however, it revealed an unusual evolution of the $S(T)$ temperature dependence started after the ETT and shown in curves 4–7 in Fig. 4. At the first glance, the $S(T)$ dependence under a high strain (Fig. 4, curves 5–7) represents a standard behavior of TEP in metals and becomes more metallic as the applied strain increases. However, the occurrence of minima around 40–50 K and the following trend to positive values do not correlate with this assumption. For a bismuth-like semimetal, in which electrons and holes can simultaneously contribute to TEP, it is necessary to take into account how each contribution to the phonon scattering mechanism acts and how they combine under a given strain to yield the sign and the magnitude of the total TEP. If we assume that a modification of all parts of the Fermi surface, both electrons and holes, takes place as a result of an ETT, we do not exclude that, at a certain strain value, one can expect the occurrence of a hole phonon drag effect. A relative enhancement of the hole phonon drag effect can be also caused by a change in the anisotropy of the hole Fermi surface and in the respective ellipsoid of the interacting phonons. To univocally interpret the origin of the temperature dependence of TEP under a high strain, we should extend the measurements of $S(T)$ under strain to a temperature range below 4.2 K for determining the position and magnitude of the phonon drag peak.

3. Conclusions

Thermopower of Bi wire of Bi wires is examined in the light of the strain-induced Electronic Topological Transition in the band structure under uniaxial strain.

At the liquid helium temperature, the diffusive transport mechanism of holes is dominant in the total TEP. However, the hole-dominated transport can be transformed into the electron-dominated transport through smooth manipulations with the phonon spectrum and the Fermi surface by applying strain. The observed trend to negative thermopower values under strain is representative of a slight increase in the electron mobility after an ETT, and the saturation-like behavior of the negative TEP under a high strain is the result of competition between the different scattering mechanisms for the heat carriers and balances between the electron and hole phonon drag contributions.

References

- [1] N.P. Armitage, R. Tediosi, F. Levy, E. Giannini, L. Forro, and D. van der Marel, Phys. Rev. Lett. 104, 237401 (2010).
- [2] T.W. Cornelius, M.E. Toimil Molares, R. Neumann, and S. Karin, J. Appl. Phys. 100, 114307 (2006).
- [3] F. Chen and K.L. Stokes, R. Funahashi, Appl. Phys. Lett. 81, 2379 (2002).

- [4] S.V. Ovsyannikov, V.V. Shchennikov, G.V. Vorontsov, A.Y. Manakov, A.Y. Likhacheva, and V.A. Kulbachinskii, *J. Appl. Phys.* 104, 053713 (2008).
- [5] J.-P. Issi and J.H. Manges, *Phys. Rev. B* 6, 4429 (1972).
- [6] C. Uher and W.P. Pratt Jr., *J. Phys. F: Met. Phys.* 8, 1979 (1978).
- [7] J. Boxus and J.-P. Issi, *J. Phys. C: Solid State Phys.* 10, L397 (1977).
- [8] J. Boxus, C. Uher, J. Heremans, and J.-P. Issi, *Phys. Rev. B* 23, 449 (1981).
- [9] P.P. Bodiul, D.V. Gitsu, V.A. Dolma, M.F. Miglei, and G.G. Zegrea, *Phys. Status Solidi (a)* 53, 87 (1979).
- [10] J. Heremans and C.M. Thrush, *Phys. Rev. B* 59 12579 (1999).
- [11] Y.-M. Lin, O. Rabin, S.B. Cronin, J.Y. Ying, and M.S. Dresselhaus, *Appl. Phys. Lett.* 81, 2403 (2002).
- [12] Yu. P. Gaidukov, *Sov. Phys.-Usp.* 27, 256 (1984) [*Usp. Fiz. Nauk* 142, 5710 (1984)].
- [13] J.P. Heremans, C.M. Thrush, D.T. Morelli, and M.C. Wu, *Phys. Rev. Lett.* 88, 216801 (2002)
- [14] A.D. Grozav and E. Condrea, *J. Phys.: Condens. Matter*, 16, 6507 (2004)
- [15] Y.I. Ravich, in: *CRC Handbook of Thermoelectrics*, edited by D.M. Rowe, CRC Press, New York, 1995, ch. 7, pp. 67–73.
- [16] M. Hagiwara and A. Inoue, *Production Techniques of Alloy Wires by Rapid Solidification in Rapidly Solidified Alloys*, edited by H.H. Liebermann, Dekker, New York, 1993, p.141.
- [17] E. Condrea, A. Nicorici, A. Gilewski, and S. Matyjasik. *J. Low Temp. Phys.* 174, 232 (2014).
- [18] L. Dagens. *J. Phys. F: Met. Phys.* 8, 2093 (1978).

MICRO-RAMAN SPECTRA OF Ge–As–Se CHALCOGENIDE AMORPHOUS POWDERS

O. V. Iaseniuc¹, M. S. Iovu¹, A. Ghiulnare², R. Mesterca², A. Jderu², and M. Enachescu^{2,3}

¹*Institute of Applied Physics, Academiei str. 5, Chisinau, MD-2028 Republic of Moldova*
²*Center for Surface Science and Nanotechnology, UPB, Splaiul Independentei 313, Bucharest, Romania*

³*Academy of Romanian Scientists, Bucharest, Romania*
E-mails: oxana.iaseniuc@gmail.com

(Received November 12, 2018)

Abstract

Analysis of the Micro-Raman spectra of $\text{Ge}_x\text{As}_x\text{Se}_{1-2x}$ ($x = 0.05\text{--}0.30$) amorphous chalcogenide glasses are reported. The Micro-Raman spectra exhibit three main peaks located at about $\nu = 193, 213, \text{ and } 255 \text{ cm}^{-1}$. The peaks at around $\nu = 193$ and 213 cm^{-1} can be attributed to the vibrations of GeSe bonds. The presence of the Raman peak at about $\nu = 255 \text{ cm}^{-1}$ is attributed to the bond-stretching vibrations of the disordered Se chains and rings. With an increase in the Ge concentration, this peak is shifted to a higher wavenumber due to the shortening of the Se chains. The peak at about $\nu = 300 \text{ cm}^{-1}$ is characteristic of the Ge–Ge vibration mode. It is found that the different Ge concentrations slightly change the shape of the Micro-Raman spectra, mainly the intensity ratio.

1. Introduction

In the last decade, interest in amorphous chalcogenide glasses (CGs) has increased due to applications of this material in photonics and optoelectronics. In particular, $\text{Ge}_x\text{As}_x\text{Se}_{1-2x}$ CGs (average coordination number of $Z = 2.1.5\text{--}2.90$) are important for a wide range of technical applications, such as infrared optical elements, acousto-optic and all-optical switching devices, holography, diffractive optics, photonic crystals, etc. [1, 2]. These glasses, such as the Ge–As–Se system, exhibit high chemical stability, fairly high transmission in the IR region, high refractive index, excellent nonlinear properties, low phonon energy, and photo-induced effects [1–4]. Recently, Ge–As–Se CGs have been used as core materials for high-efficiency fiber amplifiers, Raman-parametric lasers, and wavelength converters [5, 6]. It has been found that the physical properties of covalently-bonded glasses are determined by the mean coordination number Z (average number of covalent bonds per atom) [7]. In addition, recently, it has been found that, in the disordered network of the $\text{Ge}_x\text{As}_x\text{Se}_{1-2x}$ glassy system, there exist three distinct phases—floppy, intermediate, and stressed rigid—and the dependence of physical properties on the average coordination number Z [8–10]. It has been shown that some CGs from the $\text{Ge}_x\text{As}_x\text{Se}_{1-2x}$ system, namely, the $\text{Ge}_{0.18}\text{As}_{0.18}\text{Se}_{0.64}$ system, in which the stressed rigid phase exists, can be effectively used as temperature sensors [11]. In addition, according to Mössbauer spectroscopy and X-ray photoelectron spectroscopy studies [7] of ^{119}Sn in the $\text{As}_2\text{Se}_3:\text{Sn}_x$ glassy system [12], the introduction of group IV elements of the Periodic Table (Sn or Ge) in arsenic selenide base glass leads to the formation of new tetrahedral $\text{Sn}(\text{Se}_{1/2})_4$ and quasi-octahedral SnSe and GeSe_4

structural units, respectively. In addition, the formation of metal–metal bonds and phase separation in the studied $\text{Ge}_x\text{As}_x\text{Se}_{1-2x}$ and $(\text{As}_4\text{S}_3\text{Se}_3)_{1-x}\text{Sn}_x$ glasses can explain some physicochemical properties [7]. Optical studies, such as infrared reflectance and Raman spectroscopy, are efficient tools for obtaining information on the local structure of the disordered material, especially, when the composition is varied. Analysis of the Raman spectra of binary CGs $\text{As}_x\text{S}_{100-x}$ has revealed the presence of phase separation effects for $x \leq 25$ [13]. It has been shown that doping of chalcogenide glasses with metal impurities shift the main bands to the high frequency region and lead to the appearance of the additional vibration bands in the low frequency spectral range [14–16]. It has been shown that doping of As_2Se_3 with 0.5 at % Dy leads to the appearance of a new additional band in the Raman spectra at $\nu = 185 \text{ cm}^{-1}$, which can be attributed to the formation of new structural units, such as $\text{DySe}/\text{DySe}_2$ [17]. In addition, Raman spectroscopy has been effectively used to study the photo-induced transformation and structural changes during a heat treatment in amorphous As-based thin films. Some results on bulk glasses (optically polished plates) and amorphous thin films of $\text{Ge}_x\text{As}_x\text{Se}_{1-2x}$ have been reported [18]. It has been shown that the Micro-Raman spectra of bulk glasses and thermally deposited amorphous $\text{Ge}_x\text{As}_x\text{Se}_{1-2x}$ thin films consist of one main vibration band situated at about $\nu = 246 \text{ cm}^{-1}$ for a lower concentration of Ge and As and is attributed to $(\text{AsSe}_{1/2})_3$ pyramidal units. With an increase in the Ge and As concentrations, this band is shifted to a higher frequency region up to $\nu = 236 \text{ cm}^{-1}$ for $x = 0.30$. The vibration mode situated at around $\nu = 205 \text{ cm}^{-1}$ is attributed to $\text{Ge}(\text{Se}_{1/2})_4$ tetrahedral units; the intensity increases with increasing Ge and As concentrations. Some shoulders in high-frequency regions at $\nu = 365\text{--}390$ and $500\text{--}530 \text{ cm}^{-1}$, which are attributed to the presence of As–Se bands and Se–Se chains, are also observed.

In this study, we report the experimental results of Raman spectra measurements for powder samples of $\text{Ge}_x\text{As}_x\text{Se}_{1-2x}$ glasses ($x = 0.05\text{--}0.30$, $Z = 2.15\text{--}2.90$).

2. Experimental

Bulk $\text{Ge}_x\text{As}_x\text{Se}_{1-2x}$ ($x = 0.05\text{--}0.30$) CGs were prepared from the elements of 6N purity (Ge, As, Se,) by the conventional melt quenching method. The starting components were mixed in quartz ampoules and then evacuated to a pressure of $P \sim 10^{-5}$ Torr, sealed, and heated to a temperature of $T = 900^\circ\text{C}$ at a rate of $1^\circ\text{C}/\text{min}$. The quartz tubes were held at this temperature for 48 h for homogenization and then slowly quenched in a furnace.

The Raman studies of the chalcogenide samples were carried out by Confocal Micro-Raman Spectroscopy using a LabRam HR800 system at room temperature. All the Raman spectra were generated by exposing the specimens to a 0.03-mW green laser (wavelength of 532 nm) during 300 s and dispersing the emitted signal onto the CCD detector using a 600 lines/mm grating. The spectral resolution is about 0.6 cm^{-1} . The chalcogenide samples were optically examined using an Axio Observer Inverted Microscope (Zeiss). All the micrographs were recorded in the reflection mode at different magnifications ($5\times$, $10\times$, $20\times$, and $50\times$).

3. Results and Discussion

Figures 1 and 2 show the Micro-Raman spectra of the $\text{Ge}_{0.07}\text{As}_{0.07}\text{Se}_{0.86}$ powder samples with a mean coordination number of $Z = 2.21$. This composition with a low Ge concentration is situated in the floppy region [9]. The Micro-Raman spectra of the powder samples consist of four main vibration bands centered at around $\nu = 193$, 239, 256, and 475 cm^{-1} . The peak around

$\nu = 193 \text{ cm}^{-1}$ can be attributed to the vibration of GeSe bonds (structural units $\text{Ge}(\text{Se}_{1/2})_4$). The peak situated at $\nu = 239 \text{ cm}^{-1}$ is attributed to the vibration of $\text{As}(\text{Se}_{1/2})_3$ pyramids [9, 19]. The presence of the Raman peak at $\nu = 256 \text{ cm}^{-1}$ is due to the bond-stretching vibration of the disordered Se chains and rings. The peak located in a high frequency region at $\nu = 475 \text{ cm}^{-1}$ is associated with the presence of As–Se bands and Se–Se chains.

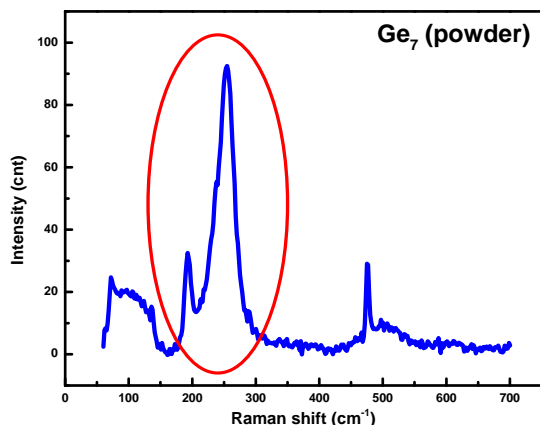


Fig. 1. Raman spectra of the $\text{Ge}_{0.07}\text{As}_{0.07}\text{Se}_{0.86}$ powder samples.

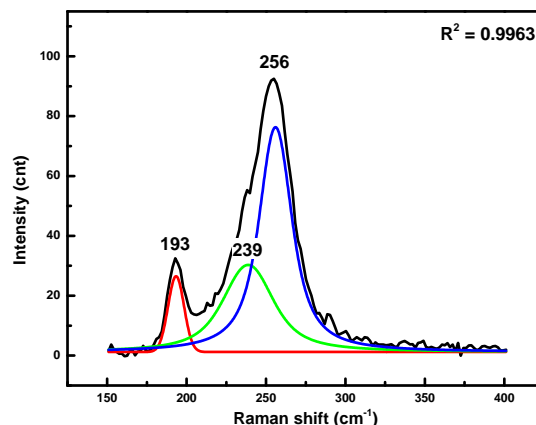


Fig. 2. Deconvolution of the spectral region marked in Fig. 1.

Figures 3 and 4 show the Micro-Raman spectra of the $\text{Ge}_{0.16}\text{As}_{0.16}\text{Se}_{0.68}$ powder with a mean coordination number of $Z = 2.48$. Note that the composition with a Ge concentration of 16 at % is situated in the intermediate region. It was found that Micro-Raman spectra of the powder samples consist of five main vibrational bands situated at around $\nu = 194, 233, 262, 292,$ and 475 cm^{-1} . As in the case of the $\text{Ge}_{0.07}\text{As}_{0.07}\text{Se}_{0.86}$ powder samples, the peak at around $\nu = 194 \text{ cm}^{-1}$ can be attributed to the GeSe vibrational bonds (structural units $\text{Ge}(\text{Se}_{1/2})_4$). The peak at $\nu = 233 \text{ cm}^{-1}$ shows modes of $\text{As}(\text{Se}_{1/2})_3$ pyramids. The presence of the Raman peak at $\nu = 262 \text{ cm}^{-1}$ is attributed to the bond-stretching vibration of the disordered Se chains and rings. The peak located in a high frequency region at $\nu = 475 \text{ cm}^{-1}$ can be caused by the presence of As–Se bands and Se–Se chains.

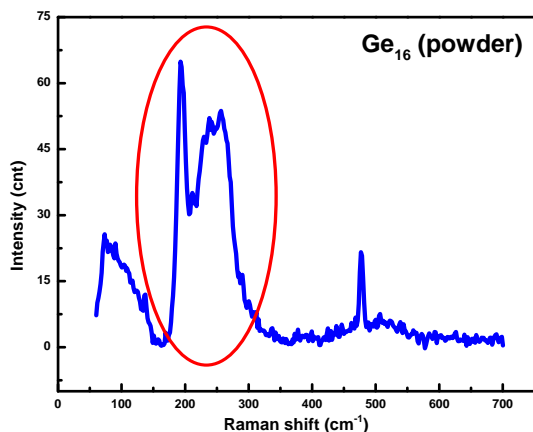


Fig. 3. Raman spectra of the $\text{Ge}_{0.16}\text{As}_{0.16}\text{Se}_{0.68}$

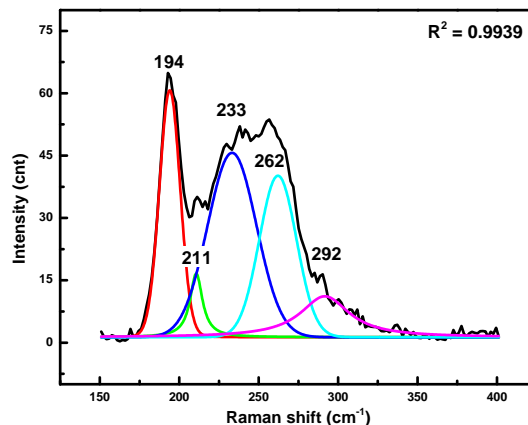


Fig. 4. Deconvolution of the spectral region

powder samples.

marked in Fig. 3.

Figures 5 and 6 illustrate the Micro-Raman spectra of the $\text{Ge}_{0.25}\text{As}_{0.25}\text{Se}_{0.50}$ powder with a mean coordination number of $Z = 2.75$. This composition is situated in the stressed-rigid region. The Micro-Raman spectra of the $\text{Ge}_{0.25}\text{As}_{0.25}\text{Se}_{0.50}$ powder samples consist of a single broad peak centered at around $\nu = 237 \text{ cm}^{-1}$. Some weak peaks in the low frequency region at around $\nu = 192 \text{ cm}^{-1}$ and two peaks in the high-frequency region at around $\nu = 259$ and 475 cm^{-1} are identified. The deconvolution process using the Gaussian function of the main peak gives the position of the vibrational modes located at around $\nu = 192, 215, 237, 269,$ and 291 cm^{-1} .

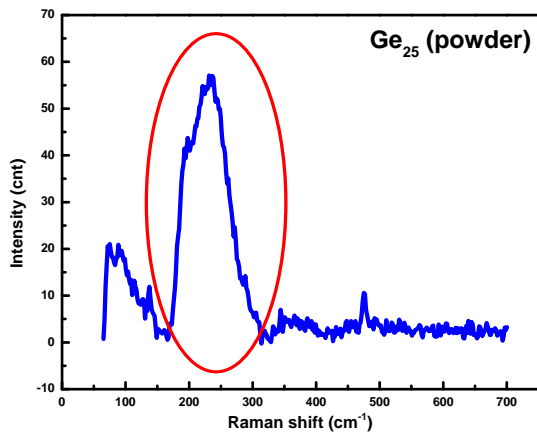


Fig. 5. Raman spectra of the $\text{Ge}_{0.25}\text{As}_{0.25}\text{Se}_{0.50}$ powder samples.

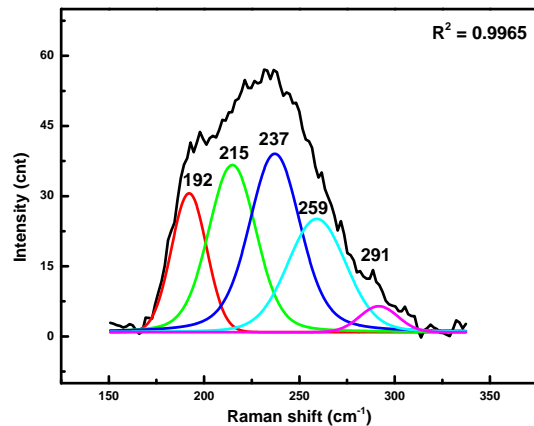


Fig. 6. Deconvolution of the spectral region marked in Fig. 5.

The Micro-Raman spectra of the $\text{Ge}_x\text{As}_x\text{Se}_{1-2x}$ powder samples showed that, with an increase in the Ge concentration, the intensity of the vibrational mode $\nu = 194 \text{ cm}^{-1}$ (GeSe bonds) became more intensive, while the peak at $\nu = 230 \text{ cm}^{-1}$ ($\text{As}(\text{Se}_{1/2})_3$ pyramids) decreases in intensity. This case is illustrated in Fig. 7, where the Micro-Raman spectra are summarized for all the powder samples of the $\text{Ge}_x\text{As}_x\text{Se}_{1-2x}$ glassy system. It is evident from the figure that, with an increase in the Ge concentration up to $x = 0.18$ ($Z = 2.54$), the intensity of the vibrational mode $\nu = 195 \text{ cm}^{-1}$ (GeSe bonds) increases. According to other measurements [20], studies of the Raman spectra of Ge–Se compounds reveal a decrease in the strength of the Se-chain with the mode centered near $\nu = 260 \text{ cm}^{-1}$ and an enhancement in the strength of the vibrational mode around $\nu = 216 \text{ cm}^{-1}$, which indicates the occurrence of a certain phase separation in these materials.

Figure 8 represents the dependence of the wavenumber position of the vibrational modes centered at around $\nu = 193, 236,$ and 255 cm^{-1} on mean coordination number Z . In addition, this figure shows the floppy, intermediate and stressed-rigid phases and their dependences for each region. The same dependences of the peak position of vibrational modes on mean coordination number Z were obtained for the $\text{Ge}_x\text{As}_y\text{Se}_{1-x-y}$ glassy system [21]. It was found that the corner-sharing of the vibrational mode at $\nu = 190 \text{ cm}^{-1}$ (tetrahedral units $\text{GeSe}_{4/2}$) is almost constant, when the mean coordination number Z is less than 2.5; however, it slightly decreases to low wavenumbers at $Z > 2.5$, as in our case (Fig. 8, black curve). The disappearance of the vibrational

mode at $\nu = 255 \text{ cm}^{-1}$ means the complete replacement of Se by Ge and by As in $\text{Ge}_x\text{As}_x\text{Se}_{1-2x}$ CGs. The full width at half maximum (FWHM) of the vibrational mode at $\nu = 193 \text{ cm}^{-1}$ increases with an increase in the Ge concentration from 14 cm^{-1} for $x = 0.05$ to 27 cm^{-1} for $x = 0.30$.

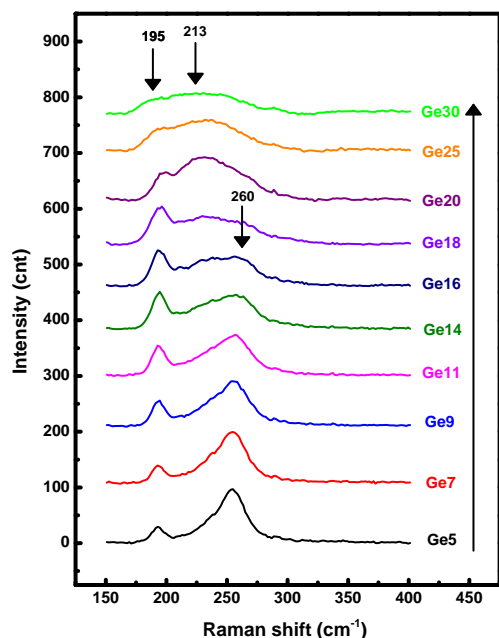


Fig. 7. Raman spectra of the $\text{Ge}_x\text{As}_x\text{Se}_{1-2x}$ powder samples. The Ge content is indicated in percents.

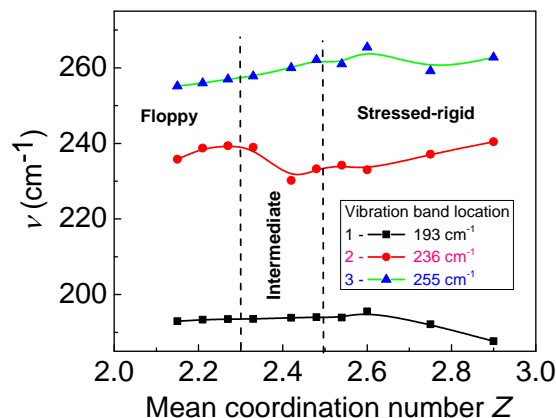


Fig. 8. Position dependence of main vibrational modes ($\nu = 193, 213,$ and 255 cm^{-1}) on mean coordination number in the Raman spectra of the $\text{Ge}_x\text{As}_x\text{Se}_{1-2x}$ powder samples.

4. Summary

Bulk (powder) glasses of the $\text{Ge}_x\text{As}_x\text{Se}_{1-2x}$ ($x = 0.05\text{--}0.30$) system with an average coordination number of $Z = 2.15\text{--}2.90$ have been studied and characterized by Micro-Raman spectroscopy. It had been found that the Micro-Raman spectra exhibit three main peaks located at around $\nu = 193, 213,$ and 255 cm^{-1} . The peaks at around $\nu = 193$ and 213 cm^{-1} can be attributed to the vibrational GeSe bonds. The presence of a Raman peak at $\nu = 255 \text{ cm}^{-1}$ is due to the bond-stretching of the disordered Se chains and rings.

It has been found that the vibration features of the Micro-Raman spectra change with increasing mean coordination number Z . With an increase in the Ge concentration, the vibration peak at $\nu = 255 \text{ cm}^{-1}$ is shifted to a higher wavenumbers due to the shortening of Se chains. The Ge concentration in the glassy system also changes the intensity of the vibrational modes in the Micro-Raman spectra.

Acknowledgments. This work was supported by projects CSSDT 16.80012.50.22A, CSSDT 15.817.02.03A, ASM-ANCS # 13.820.05.15/RoF, and the Romanian Executive Agency for Higher Education, Research, Development and Innovation Funding (UEFISCDI) through the

program PN-II “Capacitati” under contract no. 686/ 22.04.2013 and under Projects M-ERA.net 37/2016 and ECSEL – R3PowerUP, 2017.

References

- [1] H. Jain and M. Vlcek, *J. Non-Cryst. Solids* 354, 1401 (2005).
- [2] A. Zakery and S.R. Elliot, *J. Non-Cryst. Solids* 330, 1 (2003).
- [3] A. Kovalskiy, J. Cech, M. Vlcek, C.M. Waits, M. Dubey, W.R. Heffner, and H. Jain, *J. Micro/Nanolith. MEMS MOEMS* 8 (4), 043012 (2009).
- [4] I. Blonskyi, V. Kadan, O. Shpotyuk, M. Iovu, and I. Pavlov, *Opt. Mater.* 32, 1553 (2010).
- [5] Z. Rang, V.S. Shiryaev, D. Furniss, L. Sojka, S. Sujecki, M. Benson, A.B. Seddon, and M.F. Chiurbanov, *Opt. Mater. Express* 54 (8), 1722 (2015).
- [6] R. Ahmad and M. Rochette, *IEEE J. Sel. Top. Quantum Electron.* 20 (5), 0900706 (2014).
- [7] R. Golovchak, O. Shpotyuk, M. Iovu, A. Kovalskiy, and H. Jain, *J. Non-Cryst. Solids* 357, 3454 (2011).
- [8] Y. Wang, P. Boolchand, and M. Micoulaut, *Europhys. Lett.* 52 (6), 633 (2000).
- [9] Qu Tao, D.G. Georgiev, P. Boolchand, and M. Micoulaut, *Mat. Res. Soc. Symp. Proc.*, 754, CC8-12 (2003)
- [10] O. Shpotyuk, M. Hyla, V. Boyko, and R. Golovchak, *Physica B* 403, 3830 (2008).
- [11] M. Shpotyuk, D. Chalyy, O. Shpotyuk, M. Iovu, A. Kozdras, and S. Ubizkii, *Solid State Phenom.* 200, 316 (2013).
- [12] P. Boolchand, D. Georgiev, and M. Iovu, *Chalcog. Lett.* 2 (4), 27 (2005).
- [13] T. Wagner, S.O. Kasap, M. Vlcek, A. Sklenar, and A. Stronski, *J. Mater. Sci.* 33, 5581 (1998).
- [14] M.S. Iovu, E.I. Kamitsos, C.P.E. Varsamis, P. Boolchand, and M. Popescu, *J. Optoelectron. Adv. Mater.* 7 (3), 1217 (2005).
- [15] A.V. Stronski, M. Vlcek, A.I. Stetsun, A. Sklenar, and P.E. Shepeliavyi, *J. Non-Cryst. Solids* 270, 129 (2000).
- [16] M.S.Iovu, S.D. Shutov, A.M. Andriesh, E.I. Kamitsos, C.P.E.Varsamis, D. Furniss, A.B. Seddon, and M. Popescu, *J. Optoelectron. Adv. Mater.* 3 (2), 443 (2001).
- [17] M.S. Iovu, E.I. Kamitsos, and C.P.E. Varsamis, *Mold. J. Phys. Sci.* 3 (3–4), 286 (2004).
- [18] M.S. Iovu, O.V. Iaseniuc, D. Dinescu, and M. Enachescu, in *Proc. SPIE 10010, Advanced Topics in Optoelectronics, Microelectronics, and Nanotechnologies VIII*, M. Vladescu R. Tamas, I. Cristea (Eds.), p. 100100 (2016).
- [19] Y.-L. Gan, L. Wang, X.-Q. Su, S.-W. Xu, X. Shen, and R.-P. Wang, *J. Raman Spectrosc.* 45, 377 (2014).
- [20] P. Boolchand, M. Jin, D.I. Novita, and S. Chakravarty, *J. Raman Spectrosc.* 38, 660 (2007).
- [21] R.P. Wang, A. Smith, A. Prasad, D.Y. Choi, and B. Luter-Davis, *J. Appl. Phys.* 106, 043520 (2009).

Eu³⁺ PHOTOLUMINESCENCE IN MONONUCLEAR COORDINATION COMPOUNDS WITH DIFFERENT LIGANDS

O. Bordian

Institute of Applied Physics, Academiei str. 5, Chisinau, MD-2028 Republic of Moldova

E-mail: bordianolea@gmail.com

(Received October 18, 2018)

Abstract

Novel Eu³⁺-based photoluminescent (PL) organic coordination compounds have been synthesized; their optical properties in the UV–Vis spectrum have been characterized. The paper presents results of studying mononuclear coordination compounds (MCCs) with the Eu³⁺ ion, namely, Eu(*o*-MBA)₃Phen, Eu(TTA)₃(Ph₃PO)₂, Eu(DBM)₃Phen, and Eu(DBM)₃(Ph₃PO)₁H₂O. The energy of the absorption threshold (E_g) for all the studied ligands has been found to be greater than the energy required for excitation of the ${}^7F_0 \rightarrow {}^5D_0$ transitions within the transitions $4f$ orbital of the Eu³⁺ ion. The PL emission spectra of the studied coordination compounds are associated with the internal transitions of the Eu³⁺: ${}^5D_0 \rightarrow {}^7F_i$ ($i = 0, 1, 2, 3, 4$). Emission peak positions in the PL spectra are registered around 537, 580, 612, 650, and 702 nm. The FWHM of the dominant PL band at 612 nm is less than 10 nm; this finding indicates that MCCs exhibit atomic-like fluorescence emission and color purity.

1. Introduction

Coordination compounds of rare earth elements (REEs) are excellent materials for various applications because of a number of their specific properties: high efficiency (100% theoretical efficiency), easy color tuneability, temperature insensitivity, chemical environmental stability, etc. [1]. These properties enable them to be applied in various fields of optoelectronics and monochromatic light sources for organic light emitting diodes [2], luminescent sensors [2], waveguide amplifiers [3], etc. An important domain for application of coordination compounds is related to medicine and biology for tissue and cell imaging [4], drug delivery monitoring, etc [5].

Direct excitation of Eu³⁺ ions and their luminescence are negligible because the cross section of the REE ions related to absorption of the excitation light is small. Their luminescence can be significantly improved, if the REE ions are coordinated to the organic ligands with high absorption of light and form complex compounds of REEs. Enhancement of the fluorescence intensity in these compounds is associated with the energy transfer from organic ligands to REE ions.

The $4f$ orbital of the Eu³⁺ ion is shielded by electrons with a higher energy on the $5s^2$ and $5p^6$ orbital levels. This feature is responsible for an insignificant effect of the outer compound environment and crystalline symmetry on the $4f \rightarrow 4f$ transitions in of the Eu³⁺ ion. A way to overcome the problem of poor absorption of europium ions and to achieve high photoluminescence (PL) emissions is to surround the REE ion with compatible organic ligands

that are capable of absorbing the excitation light and transferring the absorbed energy to $4f$ states of the REE ion. At the same time, the surrounding ligands offer a rigid coordination protection to minimize nonradiative losses of luminescence. The saturation of the Eu^{3+} coordinate sphere with ligands allows the ion to be protected from the action of water molecules or other media that can stop luminescence [4].

Ligands play the role of complexation agents for mononuclear coordination compounds (MCCs). They can be divided into ionic ligands with chemical valence bonds and anionic neutral coordinating ligands (Table 1). The proper choice of ligands is very important for improving the luminescence efficiency of coordination compounds with Eu^{3+} ions. This is why the choice of ligands in a mononuclear compounds and their coordination with the Eu^{3+} ion is a problem that should be further studied.

This study is focused on two aims: first, to study the optical properties of various ligands to provide their optimum selection for synthesizing new MCCs and, second, to develop methods for the synthesis of new organic coordination compounds $\text{Eu}(\text{DBM})_3(\text{Ph}_3\text{PO})_1\text{H}_2\text{O}$, $\text{Eu}(\text{DBM})_3\text{Phen}$, $\text{Eu}(o\text{-MBA})_3\text{Phen}$, and $\text{Eu}(\text{TTA})_3(\text{Ph}_3\text{PO})_2$ and study their luminescent properties.

2. Methodology

2.1 Experimental

The physical properties of coordination compounds were characterized by UV–Vis and IR spectroscopy. Optical transmission spectra were measured in a spectral range of 300–800 nm on a SPECORD UV-Vis instrument (Carl Zeiss Jena). The PL of high-resolution emission spectra of powder samples were recorded using different excitation light sources: a 5-mW nitrogen laser at 337 nm at a repetition rate of 10–100 Hz and a LD source at 405 nm. The PL signal was detected using a Hamamatsu H8259-01 photomultiplier module and a C8855-01 counting unit connected to a PC. Fluorescence measurements were performed in a photon counting mode. The spectral resolution for PL spectra measurements was as low as 0.25 nm. The time-resolved PL intensity decays were recorded using an N_2 pulsed laser with a pulse width of 10 ns at a repetition rate of 10 Hz. The time resolution of the set-up was 50 μs , which was sufficient for the registration of the kinetics of the PL relaxation in a range of up to 10 ms. All PL spectra were measured at room temperature.

2.2. Technological Details and Ligand Characterization

To study the PL properties of Eu^{3+} MCCs, the following set of MCCs was designed and synthesized: $\text{Eu}(\text{DBM})_3\text{Phen}$, $\text{Eu}(o\text{-MBA})_3\text{Phen}$, $\text{Eu}(\text{TTA})_3(\text{Ph}_3\text{PO})_2$, and $\text{Eu}(\text{DBM})_3(\text{Ph}_3\text{PO})_1\text{H}_2\text{O}$. The ligands selected for synthesis of the MCCs are optimal for controlling the luminescence properties by the energy transfer mechanism and improving the compatibility and dissolution in various solvents. The chemical structures of the ligands are shown in Fig. 1. The ligands were applied as complexation agents for MCCs based on the Eu^{3+} ion. Both ionic ligands with valence chemical bonds and anionic coordination ligands were used.

The ligands were used to prepare REE coordination compounds and provide effective transitions of energy to the central Eu^{3+} ion. From the ligands absorption spectra, the absorption thresholds of the studied ligands were determined: thenoyltrifluoroacetone (TTA), α,α dipy, dibenzoylmethane (DBM), Dipic, Phen, triphenylphosphine oxide (TPPO), *o*-methylbenzoic acid

(*o*-MBA), and methanol (see Table 1).

All reagents used for the preparation of the Eu^{3+} coordination compounds were of analytical grade (~99.5% purity, Sigma Aldrich) and used without further purification. The ligands are divided into two groups: (1) ligands with valence anionic–cationic bonds, namely, TTA, DBM, and *o*-MBA and (2) ligands with coordinating bonds to the Eu^{3+} ion, namely, Phen and Ph_3PO . Both types of ligands are used as complexation agents of MCCs and as key components for absorption of excitation light and subsequent energy transfer to the central Eu^{3+} ion. In addition to providing technological compatibility with different solvents, ligands ensure electrons transition to the 5D_0 level of the Eu^{3+} ion with subsequent $^5D_0 \rightarrow ^7F_j$ transitions within the $4f$ shell.

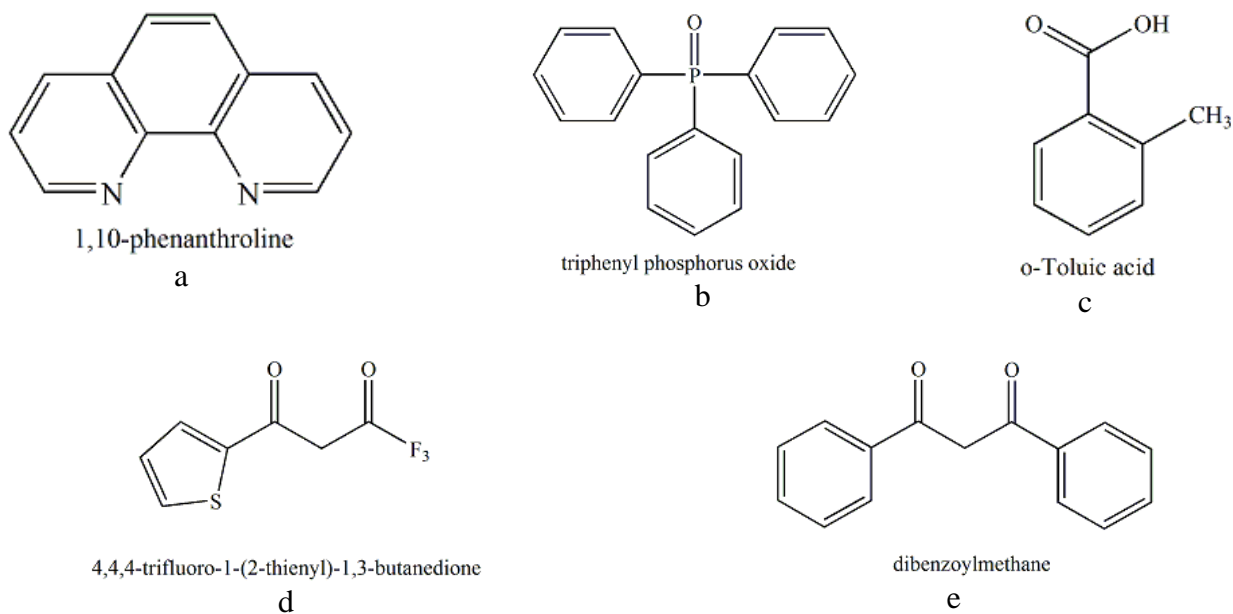


Fig. 1. Chemical structure of ligands used for the preparation of organic coordination compounds: (a) Phen, (b) Ph_3PO , (c) *o*-MBA, (d) TTA, and (e) DBM.

Table 1. Absorption threshold of ligands

| Ligand | Ligand type | E_g , eV |
|------------------------|-------------|------------------|
| TTA | ionic | 3.06 |
| α,α dipy | anionic | 3.4 |
| DBM | ionic | 3.11 |
| Dipic | anionic | 3.25 |
| Phen | anionic | 3.56 |
| Ph_3PO | anionic | 3.72 |
| <i>o</i> -MBA | ionic | 4.15 |
| methanol | solvent | 3.21; 3.23; 4.25 |

2.3. Synthesis of Eu^{3+} -Based Coordination Compounds

Eu(DBM)₃Phen–tris(1,3-phenyl-1,3-propanedione)1,10-phenanthroline Europium(III)

In this case, 0.67 g of DBM was dissolved in 10 mL of ethanol (96%); 0.2 g of phenanthroline was added to this solution; the resulting mixture was a light yellow transparent solution. Three milliliters of a 1 N NaOH solution were added to the resulting solution. The color became intense yellow. After that, 0.26 g of the EuCl_3 salt was added to 5 mL of ethanol. An incomplete dissolution was observed, and turbidity remained. Upon addition of 1 mL of H_2O , the material was completely dissolved; however, the turbidity remained.

The saturated solution was admixed with a few droplets of a EuCl_3 solution; a yellow viscous compound immediately precipitated. Subsequently, it was dissolved, filtered, and washed with ethanol and chloroform. As a result, after filtration and drying, 0.55 g of the material was dissolved in acetone. From analytical calculations for $\text{C}_{57}\text{H}_{41}\text{EuN}_2\text{O}_6$, the following content was determined (%): C, 68.33; H, 4.13; and N, 2.80. From elemental analysis, it was found (%): C, 68.43; H, 4.28; and N, 2.29.

Eu(o-MBA)₃Phen–tris(2-methylbenzoic acid)1,10-phenanthroline Europium(III)

Warmed ethanol (96%) with 0.4 g (3 mmol) of *o*-methylbenzoic acid and 0.2 g (1 mmol) of 1,10-phenanthroline were adjusted to a pH value of 6.0–7.0 with a 1 M NaOH solution. Further, europium chloride (1 mmol) was dissolved in 5 mL of water, added dropwise to the organic mixture, and stirred. A light pink precipitate was formed immediately. The precipitate was filtered, washed with small portions of ethanol, and dried thoroughly in air. The synthesis yield was 0.56 g (37.6%). From analytical calculations for $\text{C}_{36}\text{H}_{29}\text{O}_6\text{N}_2$, it was found (%): Eu, 20.61; C, 58.63; H, 3.97; and N, 3.80. From elemental analysis, it was found (%): Eu, 20.88; C, 59.23; H, 4.17; and N, 3.75.

Eu(TTA)₃(Ph₃PO)₂–tris(4,4,4-trifluoro-1-(2-thienyl)-1,3-butanedione bis(phenyl- λ -phosphine oxide)Europium(III)

In this case, 0.66 g (3 mmol) of TTA and 0.56 g (2 mmol) of TPPO were dissolved in 10 mL of warm 96% ethanol, and 3 mL of a 1 N sodium hydroxide solution was added. The mixture was stirred, while 1 mmol of europium chloride in 5 mL of water was added dropwise. A light pink precipitate was immediately formed. The precipitate was filtered off, washed with small portions of ethanol and diethyl ether, and dried thoroughly in air; the solid of the complex was obtained. The yield was 0.68 g. From analytical calculations for $\text{C}_{60}\text{H}_{42}\text{F}_9\text{EuO}_8\text{P}_2\text{S}_3$, it was found (%): C, 52.53; H, 3.09. From elemental analysis, it was found (%): C, 52.37 and 52.28; H, 3.18 and 2.98.

Eu(DBM)₃(Ph₃PO)₁H₂O–tris(1,3-phenyl-1,3-propanedione) mono(phenyl- λ -phosphine oxide) aqua Europium(III)

In this case, 0.5 g (2.24 mmol) of DBM and 0.21 g of TPPO (0.746 mmol) were dissolved in 10 mL of heated 96% ethanol to the resulting warm solution. A filtered solution of 0.19 g (0.746 mmol) of europium chloride hexahydrate was dissolved in a mixture of 2 mL of

water and 1 mL of ethanol, and 2.3 mL of 1 N sodium hydroxide solution were added. During mixing and grinding, a creamy residue precipitated. The resulting precipitate was washed with water and then with methanol and ether. The substance is readily soluble in methanol and ether. The yield was 0.42 g. Analysis for chlorine negative, analysis for europium: analytical calculations (%): 13.59. From elemental analysis, it was found (%): 13.81.

3. Optical and Luminescence Characterization of the MCCs

3.1. Optical Properties of the MCCs

Absorption spectra $\alpha(\lambda)$ of the solutions with the different ligands and for the different MCCs in the UV–Vis domain show absorption bands with the first sharp absorption threshold in the spectral range of 330–380 nm. These bands are apparently attributed to the absorption of the coordinating ionic ligands incorporated in the organic compound.

The absorption thresholds of the ligands and MCCs were determined from the Tauc plot $(ah\nu)^{1/n} = f(h\nu)$, where the value of exponent n is determined by the nature of the amorphous–crystalline material transition: for allowed direct transitions, $n = 1/2$ [5]. From linear interpolation of the experimental plot, we obtained the energy values for the absorption threshold $E_g = \text{LOMO} - \text{HOMO}$ (where HOMO is the energy of the highest occupied molecular orbital, and LUMO is the energy of the lowest unoccupied molecular orbital). In this way, from experimental data, energy values E_g were estimated for each ligand: $\text{Eu}(\text{DBM})_3(\text{Ph}_3\text{PO})_1\text{H}_2\text{O}$, 2.83 eV; $\text{Eu}(\text{TTA})_3(\text{Ph}_3\text{PO})_2$, 3.05 eV; $\text{Eu}(o\text{-MBA})_3\text{Phen}$, 3.42 eV; and $\text{Eu}(\text{DBM})_3\text{Phen}$, 3.11 eV.

3.2. Luminescent Properties of the MCCs

The PL spectra of all coordinating compounds with the Eu^{3+} ions have similar shapes and almost identical emission peaks. The only difference between them is the maximum magnitude of the PL intensity that determines the efficacy (Table 2). The radiative transitions of europium ions can be observed in PL spectra; they are centered at around 580, 590, 612–615, 651, and 700 nm (Figs. 4a–4d). These emission bands are attributed to internal $4f$ electron transitions ${}^5D_0 \rightarrow {}^7F_i$ ($i = 0, 1, 2, 3, 4$) of the Eu^{3+} ion with a dominant emission band in the region of 612–615 nm (${}^5D_0 \rightarrow {}^7F_2$). Comparison of the PL spectra of the studied MCCs shows an increase in the PL intensity in $\text{Eu}(\text{TTA})_3(\text{Ph}_3\text{PO})_2$ by about 4.6 times in comparison with the intensity of the other studied MCCs.

The high efficiency of PL in coordinating compounds with Eu^{3+} ions is attributed to the mechanism of energy transfer through the excited electrons states from the singlet (S) and triplet (T) levels of the ligands to the central Eu^{3+} ion (Fig. 5). The observed emission bands are associated with radiative transitions ${}^5D_0 \rightarrow {}^7F_i$ from the excited states in the Eu^{3+} $4f$ shell. It was found that, of all the studied compounds, $\text{Eu}(\text{TTA})_3(\text{Ph}_3\text{PO})_2$ exhibits the most efficient energy transfer from ligands to the Eu^{3+} ion (Fig. 4a).

From analysis of the experimental results on PL and absorption spectra, we can identify a cascade of the energy transfer from the LUMO energy levels of ligands to the energetic levels of the $4f$ electronic shell of the Eu^{3+} ion. It should be noted that the energy of the S and T levels of ligands in MCCs is higher than the energies of the respective PL bands of the Eu^{3+} ion ${}^5D_0 \rightarrow {}^7F_j$ (Fig. 6).

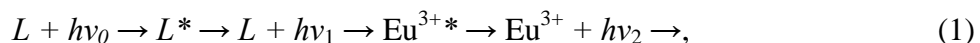
4. Discussion

4.1. Energy Transfer

Energy transfer through the excitation of electrons takes place between different sites within the same molecule (intramolecular transfer). In the case of the radiation mechanism, known as the Förster's mechanism of energy transfer [6], the acceptor (Eu^{3+} ion) receives absorbed energy of the donor (ligands) in form of photons (Figs. 5, 6).

The transfer of radiative energy takes place when the energy of the electron excitation of the acceptor is greater than that of the donor. This process is fast enough to take place over the lifetime of the excited state.

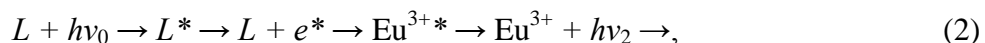
The energy transfer mechanism in the Förster process is illustrated by the scheme shown in Fig. 5:



where L and L^* denotes the unexcited and excited ligands, respectively; hv_0 is the excitation photon energy; hv_1 is the ligand emission photon energy; hv_2 is the emission photon energy from the Eu^{3+} ion; and Eu^{3+*} denotes the Eu^{3+} ion in the excited state.

The efficiency of the energy transfer process depends on the spectral overlap between the ligand emission and the absorbance of the Eu^{3+} acceptor.

The Dexter energy transfer process is an electron exchange mechanism [7]. The Dexter mechanism takes place between the ligand and the Eu^{3+} ion, which are extremely close and, in most cases, molecularly connected. This mechanism is also referred to as the electronic mechanism carried out by molecular chemical bonds. Energy transfer is the process by which an excited triplet or singlet state of the ligand creates an excited state in the Eu^{3+} ion. The Dexter relation below illustrates the overall form of the electron exchange mechanism (Fig. 5):



where e^* denotes the excited electron.

The distance separating the ligand and acceptor sites of Eu^{3+} is fairly small and facilitates an efficient energy transfer due to the minimum spacing within the MCC molecule.

The energy levels of the emitting states 5D_i of Eu^{3+} are smaller than the threshold energy obtained from extinction coefficient (ϵ) for the mentioned ligands. The electronic state with the lowest energy value of the ligand in the triplet state is greater than that of the lowest transition ${}^5D_0 \rightarrow {}^7F_0$; therefore, the expected energy transfer occurs. To provide an efficient energy transfer, the triplet energy of the ligand should be greater than or equal to the europium level of 5D_0 (${}^5D_0 = 17264 \text{ cm}^{-1}$).

The identification of the PL bands in the spectrum in Fig. 2c is characteristic of transitions of excited electrons from the 5D_0 level to 7F_i . This also refers to the spectra shown in Figs. 2a, 2b, and 2d.

The dominant emission band associated with the ${}^5D_0 \rightarrow {}^7F_2$ optical transition can be deconvoluted into three to five bands (Fig. 3). According to Judd–Ofelt theory [4, 11, 2], it can be speculated that the studied compounds have a triclinic symmetry of the lattice.

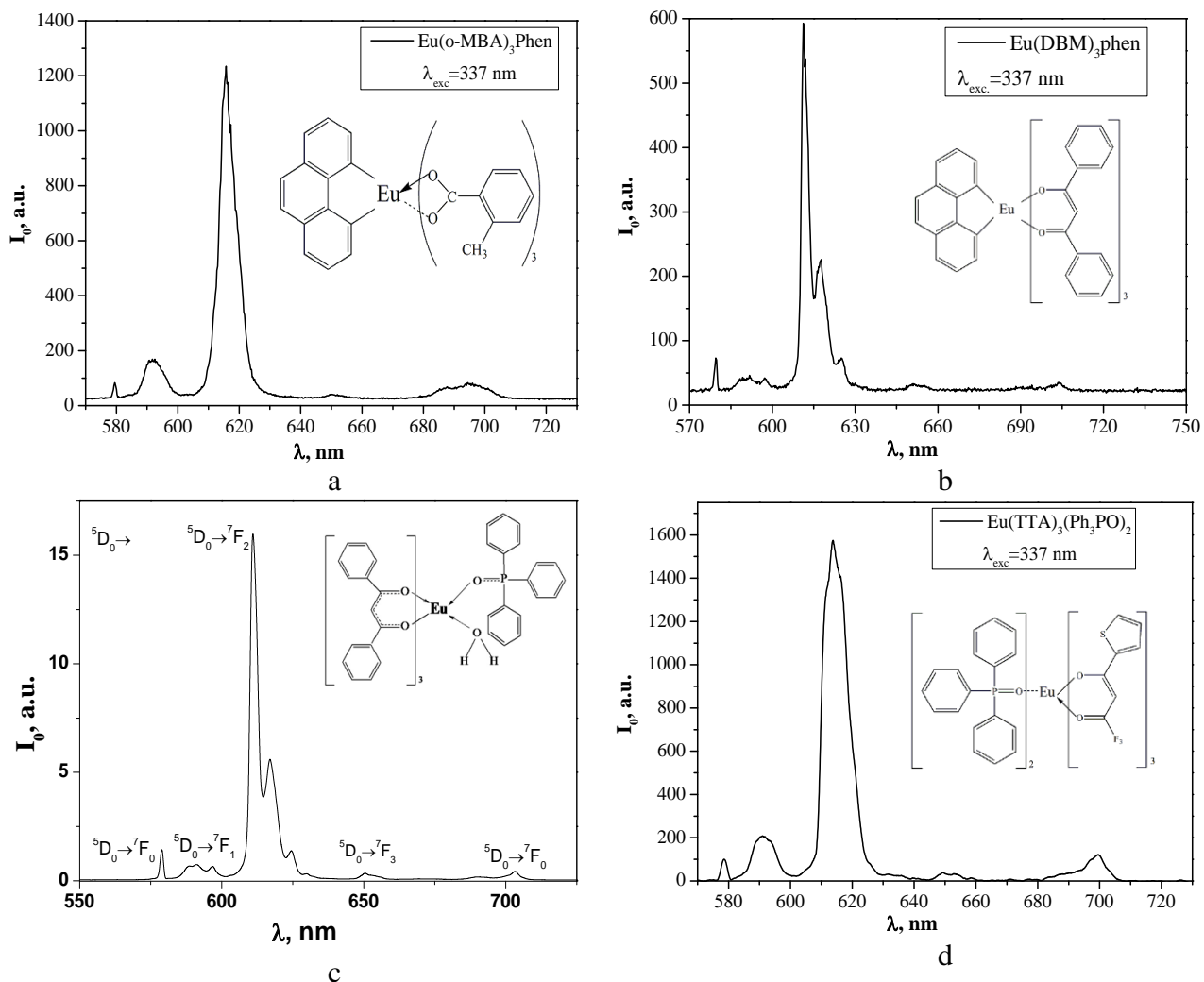


Fig. 2. PL spectra and chemical structure of Eu^{3+} MCCs: (a) $\text{Eu}(\text{o-MBA})_3\text{phen}$, (b) $\text{Eu}(\text{DBM})_3\text{phen}$, (c) $\text{Eu}(\text{DBM})_3(\text{Ph}_3\text{PO})_1\text{H}_2\text{O}$, and (d) $\text{Eu}(\text{TTA})_3(\text{Ph}_3\text{PO})_2$. The excitation wavelength is 337 nm.

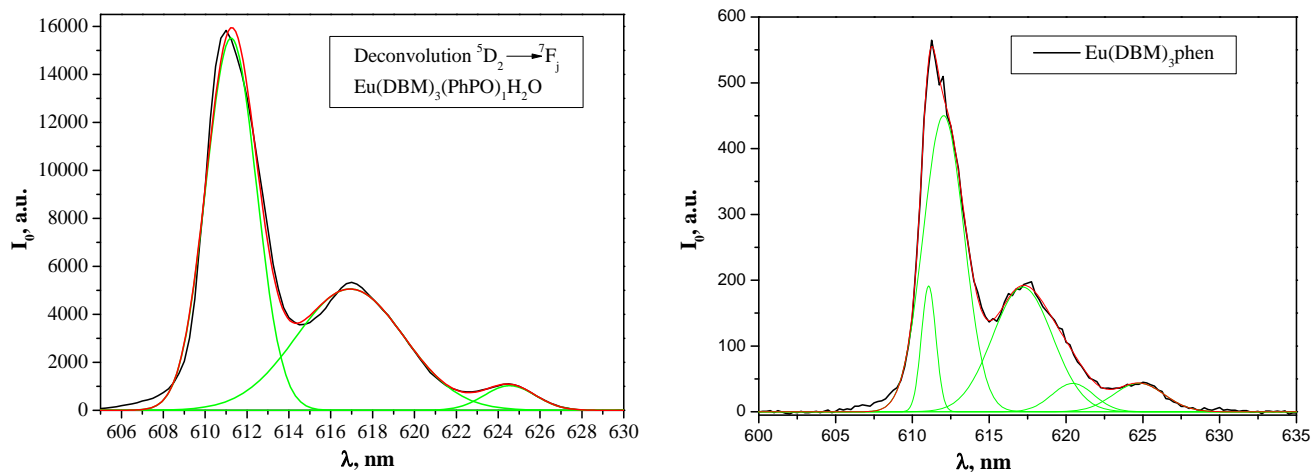


Fig. 3. PL spectra and their deconvolution (in green) of MCCs for the luminescent band associated with the ${}^5\text{D}_0 \rightarrow {}^7\text{F}_2$ transition (in Fig. 2) of $\text{Eu}(\text{DBM})_3(\text{Ph}_3\text{PO})_1\text{H}_2\text{O}$ and $\text{Eu}(\text{DBM})_3\text{phen}$; $\lambda_{\text{exc}} = 337$ nm.

Figure 4 illustrates the decay of PL intensity under pulsed laser excitation plotted in the $\ln(I_{PL})-t$ coordinates. The exponential pattern of the decay, as in Fig. 4, is characteristic of all the MCCs studied here. This plot corresponds to the exponential decay of the PL intensity, which can be described by the following relation: $I = I_0 \cdot \exp(-t/\tau)$, where τ is the characteristic time of the spontaneous PL decay. For the MCCs, the τ values are listed in Table 2.

The interpretation of the PL spectra is made in terms of the Judd–Ofelt theory [8, 9]. The estimated values of the transition probabilities and efficiency of PL were calculated (Table 2). The intensity of emission transitions are described by the relation

$$I_{0 \rightarrow j} = h\nu_{0 \rightarrow j} A_{0 \rightarrow j} N_0, \quad (3)$$

where $h\nu_{0 \rightarrow j}$ is the energy maximum of the transition, N_0 is the concentration of the emitting centers of Eu^{3+} ions, and $A_{0 \rightarrow j}$ is the Einstein coefficients of spontaneous emission. The coefficients of spontaneous emission $A_{0 \rightarrow j}$ are obtained from the equation

$$A_{0 \rightarrow j} = \frac{\lambda_{0 \rightarrow j} \times I_{0 \rightarrow j}}{\lambda_{0 \rightarrow 1} \times I_{0 \rightarrow 1}} \times A_{0 \rightarrow 1}, \quad (4)$$

where $I_{0 \rightarrow j}$ corresponds to the integrated PL intensity related to the ${}^5D_0 \rightarrow {}^7F_j$ transition, and $\lambda_{0 \rightarrow j}$ is the wavelength of the PL maximum of the $0 \rightarrow j$ transitions. For experimental determination of emission coefficients $A_{0 \rightarrow j}$ from the emission spectra, the magnetic dipole, the allowed ${}^5D_0 \rightarrow {}^7F_1$ transition was used, which is formally insensitive to the chemical environment around the Eu^{3+} ion and, consequently, can be used as a reference $A({}^5D_0 \rightarrow {}^7F_1) = 50 \text{ s}^{-1}$ [10].

The results of the study of the PL spectra and the calculations performed according to formulas (2)–(4) are shown in Table 2. The PL parameters are as follows: integrated PL intensity (I), λ_{max} , I_{max} , and the probability of $A_{0 \rightarrow j}$ transitions at excitation with a laser beam of 337 or 405 nm. The relaxation time of PL of the MCCs is 0.27 ms for $\text{Eu}(\text{DBM})_3(\text{Ph}_3\text{PO})_1\text{H}_2\text{O}$ and 0.52 ms for $\text{Eu}(o\text{-MBA})_3\text{Phen}$ (Fig. 4).

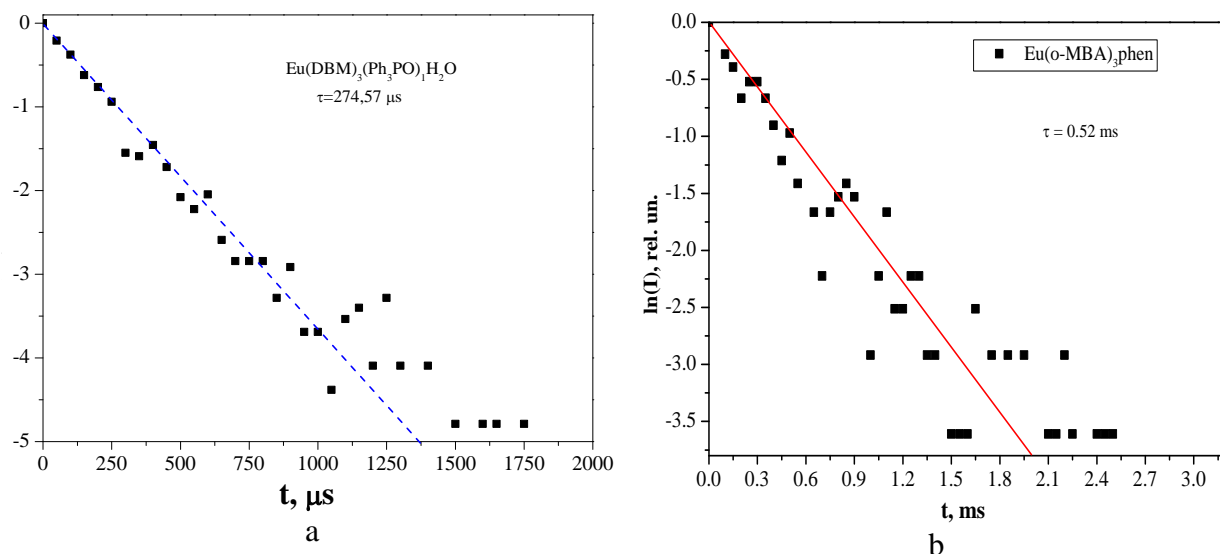


Fig. 4. Kinetics of the PL decay after 10-ns pulsed excitation at 337 nm: (a) $\text{Eu}(\text{DBM})_3(\text{Ph}_3\text{PO})_1\text{H}_2\text{O}$ and (b) $\text{Eu}(o\text{-MBA})_3\text{Phen}$.

Table 2. Parameters of PL transitions ${}^5D_0 \rightarrow {}^7F_j$ ($j = 0, 1, 2, 3, 4$) for Eu^{3+} -based MCCs

| Eu(<i>o</i> -MBA) ₃ Phen, $\lambda_{\text{exc}} = 337$ nm | | | | | |
|--|-------------------------------|-------------------------------|-------------------------------|-------------------------------|-------------------------------|
| | ${}^5D_0 \rightarrow {}^7F_0$ | ${}^5D_0 \rightarrow {}^7F_1$ | ${}^5D_0 \rightarrow {}^7F_2$ | ${}^5D_0 \rightarrow {}^7F_3$ | ${}^5D_0 \rightarrow {}^7F_4$ |
| <i>I</i> (integrated PL intensity), rel. un. | 57.7 | 1008.3 | 8412.5 | 79.1 | 886.6 |
| λ_{max} , nm | 579.4 | 591.4 | 615.6 | 649.7 | 694.6 |
| I_{max} , quant/s | 79.5 | 167.9 | 1232.8 | 40.8 | 82.1 |
| $A_{0 \rightarrow j}$, s^{-1} | 2.8 | 50 | 434.1 | 4.3 | 51.6 |
| Eu(DBM) ₃ Phen, $\lambda_{\text{exc}} = 337$ nm | | | | | |
| | ${}^5D_0 \rightarrow {}^7F_0$ | ${}^5D_0 \rightarrow {}^7F_1$ | ${}^5D_0 \rightarrow {}^7F_2$ | ${}^5D_0 \rightarrow {}^7F_3$ | ${}^5D_0 \rightarrow {}^7F_4$ |
| <i>I</i> (integrated PL intensity), rel. un. | 56.3 | 156.5 | 3142 | 44.3 | 85.6 |
| λ_{max} , nm | 579.5 | 591.8 | 611.1 | 651.5 | 704.02 |
| I_{max} , quant/s | 165.9 | 91.7 | 1770.8 | 64.5 | 68.2 |
| $A_{0 \rightarrow j}$, s^{-1} | 17.6 | 50 | 1036.6 | 15.6 | 32.5 |
| $\lambda_{\text{exc}} = 405$ nm | | | | | |
| | ${}^5D_0 \rightarrow {}^7F_0$ | ${}^5D_0 \rightarrow {}^7F_1$ | ${}^5D_0 \rightarrow {}^7F_2$ | ${}^5D_0 \rightarrow {}^7F_3$ | ${}^5D_0 \rightarrow {}^7F_4$ |
| <i>I</i> (integrated PL intensity), rel. un. | 168.1 | 516.7 | 10088.7 | 167.3 | 281.2 |
| λ_{max} , nm | 579.2 | 591.8 | 611.06 | 650.6 | 703.8 |
| I_{max} , quant/s | 165.9 | 91.7 | 1770.8 | 64.5 | 68.2 |
| $A_{0 \rightarrow j}$, s^{-1} | 15.9 | 50 | 1007.8 | 17.8 | 32.3 |
| Eu(TTA) ₃ (Ph ₃ PO) ₂ , $\lambda_{\text{exc}} = 337$ nm | | | | | |
| | ${}^5D_0 \rightarrow {}^7F_0$ | ${}^5D_0 \rightarrow {}^7F_1$ | ${}^5D_0 \rightarrow {}^7F_2$ | ${}^5D_0 \rightarrow {}^7F_3$ | ${}^5D_0 \rightarrow {}^7F_4$ |
| <i>I</i> (integrated PL intensity), rel. un. | 217.3 | 1677.4 | 14631.6 | 260.1 | 1197.5 |
| λ_{max} , nm | 578.5 | 590.8 | 613.7 | 649.4 | 699.5 |
| I_{max} , quant/s | 173.8 | 276.03 | 1640.9 | 111.1 | 189.1 |
| $A_{0 \rightarrow j}$, s^{-1} | 6.3 | 50 | 453.02 | 8.5 | 42.2 |
| $\lambda_{\text{exc}} = 405$ nm (powder) | | | | | |
| | ${}^5D_0 \rightarrow {}^7F_0$ | ${}^5D_0 \rightarrow {}^7F_1$ | ${}^5D_0 \rightarrow {}^7F_2$ | ${}^5D_0 \rightarrow {}^7F_3$ | ${}^5D_0 \rightarrow {}^7F_4$ |
| <i>I</i> (integrated PL intensity), rel. un. | 249.7 | 7677.75 | 141294.5 | 2094.3 | 5557.7 |
| λ_{max} , nm | 578.4 | 588.08 | 613.5 | 650.6 | 692.4 |
| I_{max} , quant/s | 478.4 | 1219.1 | 22735.8 | 660.3 | 769.2 |
| $A_{0 \rightarrow j}$, s^{-1} | 1.5 | 50 | 960 | 15.08 | 42.6 |
| Eu(DBM) ₃ (Ph ₃ PO) ₁ H ₂ O, $\lambda_{\text{exc}} = 337$ nm | | | | | |
| | ${}^5D_0 \rightarrow {}^7F_0$ | ${}^5D_0 \rightarrow {}^7F_1$ | ${}^5D_0 \rightarrow {}^7F_2$ | ${}^5D_0 \rightarrow {}^7F_3$ | ${}^5D_0 \rightarrow {}^7F_4$ |
| <i>I</i> (integrated PL intensity), rel. un. | 57.3 | 167.9 | 1716.01 | 42.2 | 71.9 |
| λ_{max} , nm | 578.8 | 591.00 | 611.2 | 651.8 | 703.1 |
| I_{max} , quant/s | 57.3 | 53.6 | 325 | 40.4 | 43.6 |
| $A_{0 \rightarrow j}$, s^{-1} | 10.04 | 50 | 528.2 | 13.8 | 25.4 |
| $\lambda_{\text{exc}} = 405$ nm | | | | | |
| | ${}^5D_0 \rightarrow {}^7F_0$ | ${}^5D_0 \rightarrow {}^7F_1$ | ${}^5D_0 \rightarrow {}^7F_2$ | ${}^5D_0 \rightarrow {}^7F_3$ | ${}^5D_0 \rightarrow {}^7F_4$ |
| <i>I</i> (integrated PL intensity), rel. un. | | | 23.034×10^8 | 0.3981×10^8 | 0.2440×10^8 |
| λ_{max} , nm | | 587.6 | 610.04 | 656.6 | 700.3 |
| I_{max} , quant/s | | 0.153×10^8 | 3.2978×10^8 | 0.0759×10^8 | 0.0556×10^8 |

4. Conclusions

A new $\text{Eu}(\text{DBM})_3(\text{Ph}_3\text{PO})_1\text{H}_2\text{O}$ PL compound has been synthesized; novel technological schemes for the preparation of $\text{Eu}(\text{o-MBA})_3\text{Phen}$, $\text{Eu}(\text{DBM})_3\text{Phen}$, and $\text{Eu}(\text{TTA})_3(\text{Ph}_3\text{PO})_2$ compounds with chosen ligands have been proposed. The MCCs have been characterized by measuring the PL spectral characteristics and the luminescence relaxation kinetics.

The optical properties of a number of ligands have been studied for optimization of the composition in the synthesis of Eu^{3+} -based coordination compounds. The absorption thresholds of both the ligands and the coordinating compounds have been determined. For the studied MCCs, a number of parameters have been determined, namely, absorption threshold, PL transitions

$^5D_0 \rightarrow ^7F_j$ ($j = 0, 1, 2, 3, 4$), PL integrated intensity, PL probability, and relaxation time.

A model of an energy transfer scheme for the Eu^{3+} ion under UV light excitation has been proposed.

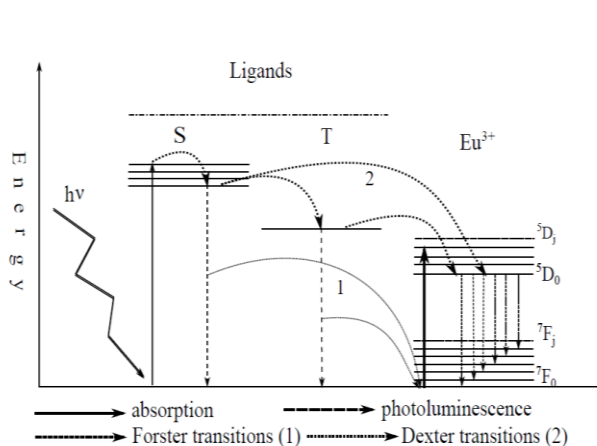


Fig. 5. Illustration of the energy transfer mechanism from ligands to the Eu^{3+} ion.

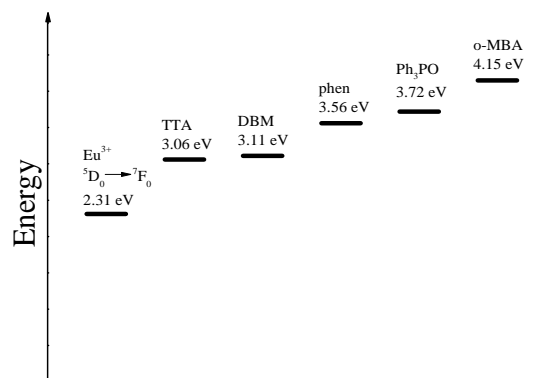


Fig. 6. Positions of energy levels for the absorption threshold of the ligands used in the synthesis of coordination compounds and the levels of the $5D_0 \rightarrow 7F_0$ energy transition of the Eu^{3+} ion.

Acknowledgments. This work was supported by the Institute of Applied Physics (project nos. 11.817.05.03A and 11.817.05.04A) and the Science and Technology Center in Ukraine (project no. 6117). I would like to thank Dr. I. Culeac for PL measurements, Dr. V. Zubareva for the synthesis of Eu^{3+} MCCs, and Prof. M. Iovu and Dr. V. Verlan for discussion of the results.

References

- [1] J. Kido and Y. Okamoto, *Chem. Rev.* 102, 2357 (2002).
- [2] Rare-earth-doped waveguide amplifiers and lasers in *Handbook on the Physics and Chemistry of Rare Earths*, edited by J.-C. Bunzli and V. Pecharsky, Elsevier, North-Holland, 2017, vol. 51, ch. 296, pp. 111–168.
- [3] J.-C.G. Bünzli, *Coord. Chem. Rev.* 293, 19 (2015).
- [4] K. Binnemans, *Chem. Rev.* 109, 4283 (2009).
- [5] J. Tauc, *Mater. Res. Bull.* 3, 37 (1968).
- [6] T. Förster, *Faraday Soc.* 27, 7 (1959).
- [7] D.L. Dexter, *J. Chem. Phys.* 21, 836 (1953).
- [8] B.R. Judd, *Phys. Rev.* 127, 750 (1962).
- [9] G.S. Ofelt, *J. Chem. Phys.* 37, 511 (1962).
- [10] R. Saraf, C. Shivakumara, N. Dhananjaya, S. Behera, and H. Nagabhusana. *J. Mater. Sci.* 50, 287 (2015).

STRUCTURAL STUDY OF MONO- AND BINUCLEAR 2,6-DIACETYLPIRIDINE BIS(NICOTINOYLHYDRAZONE) COORDINATION COMPOUNDS

Olga Danilescu

*Institute of Chemistry, Academiei str. 3, Chisinau, MD-2028 Republic of Moldova
E-mail: olgadanilescu@mail.ru*

(Received May 10, 2018)

Abstract

2,6-Diacetylpyridine bis(nicotinoylhydrazone) (H_2L) represents a Schiff base condensation product of 2,6-diacetylpyridine and nicotinic acid hydrazide and may represent a versatile ligand for a variety of research objectives because it has multiple coordination sites. In this review, the design of seven coordination compounds of the title ligand H_2L with some transition metals-V(II, IV), Fe(III), and Co(II)-is reported. The V(IV), Fe(III), and Co(II) metals give rise to the mononuclear compounds where the metal cations form pentagonal bipyramids, while V(II) forms a binuclear compound with the metal in a tetragonal pyramid environment. The characteristic IR oscillations of H_2L in all complexes and promising adsorption properties are analyzed.

1. Introduction

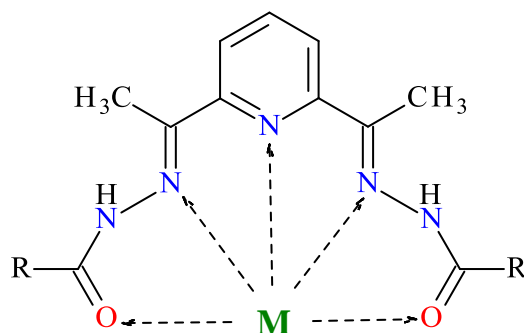
A Schiff base is a condensation product of an aldehyde/ketone and a primary amine [1], which was first reported by Hugo Schiff in 1864. The general formula for a Schiff base is $RN=CR_1R_2$ where R, R_1 , and R_2 could be alkyl, aryl, heteroaryl, or cycloalkyl, etc. The complexation of a Schiff base with transition metals leads to the enhancement of their biological activities and a decrease in the cytotoxicity of both the metal ion and the Schiff base ligand [2–4]. These ligands show their versatility of coordinating with a variety of metal ions in different coordination geometries and oxidation states. Schiff bases have been known to form complexes with all transition metals and with lanthanides, which have made them attractive as analytical reagents for spectrophotometric and sensitive spectrofluorimetric determination of trace amounts of these cations [5].

The imine nitrogen atom is capable of acting as a Lewis base toward metal ions; stable coordination is achieved if the metal ion is coordinated with other electron donating groups of the molecule. This condition is generally met when the azomethine bond is present in the vicinity of other electron donating groups/atoms either as ring heteroatoms or as side chains on the molecular scaffold. Hence, the azomethine linkage provides much flexibility in the design of Schiff base ligands with superior and, in some cases, even selective metal ion coordination properties.

Hydrazones represent an important class of compounds that contain an azomethine bond and, similar to Schiff bases, are versatile compounds with vast synthetic utility. Both nitrogen atoms of hydrazones are nucleophilic; however, the amino group nitrogen is more reactive. The azomethine carbon atom has both electrophilic and nucleophilic character; thus, hydrazones have

been known to react with both nucleophilic and electrophilic reagents [6]. The introduction of different functional groups adjacent to the hydrazone linkage further expands the scope of these compounds as chemical reagents [7].

2,6-Diacetylpyridine (dap) is an excellent precursor for the synthesis of a number of complexing agents [8] which can act as planar pentadentate ligands and contribute to the formation of heptacoordinated pentagonal-bipyramidal complexes [9–14]. The dap ligands, due to their multiple coordination sites (Scheme 1), are capable of efficiently stabilizing the metal center forming unique geometries [15].



Scheme 1. Representation of 2,6-diacetylpyridine hydrazone multiple coordination sites (R = several organic groups).

Coordination compounds derived from dap hydrazones and transition metal ions have yielded a surprisingly rich chemistry. The retrieval of Cambridge Structural Database (CSD) [16] revealed over 100 complexes, reported for R = methyl, amine, pyridine, phenyl, phenol, aniline, imidazole or thiosemicarbazone and their derivatives, only 5 of them being 1D and 2D coordination polymers, while all the other represent discrete compounds, mono-, bi-, tri-, tetra-, and pentanuclear ones.

We have favored 2,6-diacetylpyridine bis(nicotinoylhydrazone) for design and synthesis of vanadium(II, IV), iron(III) and cobalt(II) coordination complexes. Herein, we summarize our recent results on synthesis and single-crystal X-ray structural study of a series of homometallic mono- and binuclear compounds with the following compositions: $[V^{IV}(=O)(H_2L)(SO_4)] \cdot 5H_2O$ (**1**), $[V^{II}_2(H_2L)_2](NO_3)_4 \cdot H_2O$ (**2**), $[(Fe(H_2L)(H_2O)_2](NO_3)_3 \cdot 5H_2O$ (**3**), $[Co(H_2L)(NCS)_2] \cdot CH_3OH$ (**4**), $[Co(H_2L)(NCS)(H_2O)]NCS$ (**5**), $[Co(H_4L)(NCS)_2][Co(NCS)_4] \cdot 1.75H_2O$ (**6**), $[Co(H_2L)(NCS)(CH_3OH)]_2[Co(NCS)_4] \cdot 2CH_3OH$ (**7**) [17–20].

2. Discussion

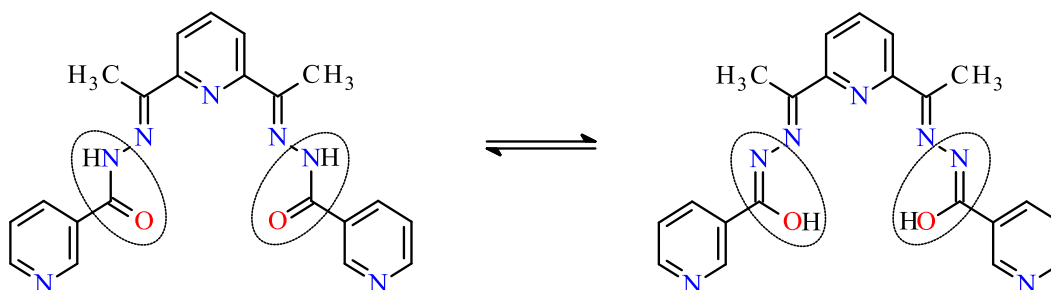
The condensation of 2,6-diacetylpyridine and different hydrazides leads to the formation of the flexible Schiff bases possessing at least five potential donors, such as one pyridine and two azomethine N atoms and two carbonyl O atoms, which can be coordinated in neutral, mono- and/or doubly-deprotonated modes. The coordination of N_3O_2 atom donors provides the

formation of pentagonal-bipyramidal complexes with a stabilized nearly planar system in the equatorial plane of the bipyramid comprised of four five-membered chelate rings and monodentate ligands in the apical positions [21–24]. This geometry depends on the conformational flexibility of the ligand, the coordination capacity of the metal ion, and reaction conditions [25].

Hydrazones play an important role in inorganic chemistry, because they readily form stable complexes with many transition metal ions and many of these complexes may serve as models for biologically important species [26]. It is known that hydrazones derived from condensation of isonicotinic acid hydrazide and pyridine aldehydes exhibit better antitubercular activity than that of hydrazide [27–29].

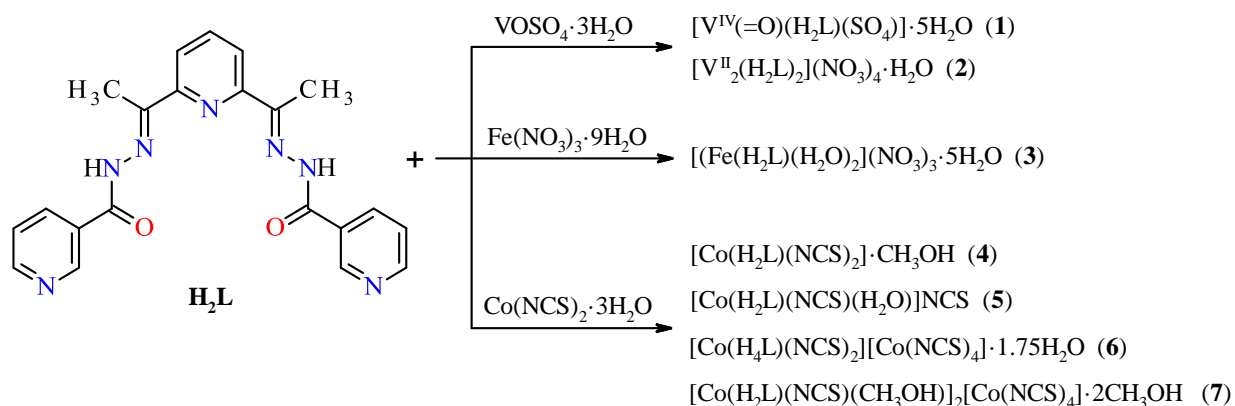
2,6-Diacetylpyridine bis(pyridine-*n*-carbonylhydrazones) ($n = 2, 3, 4$) are versatile ligands for a variety of research objectives. Analysis of the Cambridge Structural Database [16] reveals that, of the three isomeric Schiff bases, 2,6-diacetylpyridine bis(pyridine-3-carbonylhydrazone) is the least commonly used ligand system, since 2,6-diacetylpyridine bis(pyridine-2-carbonylhydrazone) forms mono- [30–32] and tetranuclear complexes with Mn(II), Co(II), Cu(II) and Sn(IV) cations [33–34], while 2,6-diacetylpyridine bis(pyridine-4-carbonylhydrazone) gives rise to mononuclear compound [35] and bidimensional coordination polymer in combination with Mn(II) and Sn(II) cations [36].

2,6-Diacetylpyridine bis(pyridine-3-carbonylhydrazone), also known as 2,6-diacetylpyridine bis(nicotinoylhydrazone) (H_2L), may display keto-enol tautomerism interconversion related with the coordination through either nitrogen or oxygen atoms, or both atoms, and diversifies the coordination to metal centers. It should be noted that the keto-enol equilibrium is possible, especially when the hydrazone hydrogen is abstracted, as shown in Scheme 2.



Scheme 2. Structures of the H_2L ligand and tautomeric forms of it.

Coordination compounds of V(II, IV), Fe(III), and Co(II) with the condensation product of dap and nicotinic acid hydrazide were prepared using the direct method of synthesis in the reaction of the H_2L ligand and the corresponding metal salt in a molar ratio of 1 : 1. Thus, seven transition metal complexes were obtained; their crystal structures were determined by single-crystal X-ray diffraction. Compound **1** represents a binuclear compound, while compounds **2–7** are mononuclear complexes (Scheme 3).



Scheme 3. Synthetic route to the reported coordination compounds.

The crystal structures of **1** and **3–7** are built from molecular mononuclear complexes (**1** and **4**) and cations (**3**, **5–7**), where the coordination polyhedra of the metal cations represent pentagonal bipyramids formed by N_3O_2 set of donor atoms going from the pentadentate Schiff base ligand in the equatorial plane, while the axial vertices are occupied by anions (SO_4^{2-} , NCS^-) and/or solvent molecules (H_2O , CH_3OH) both coordinated in a monodentate fashion (Fig. 1).

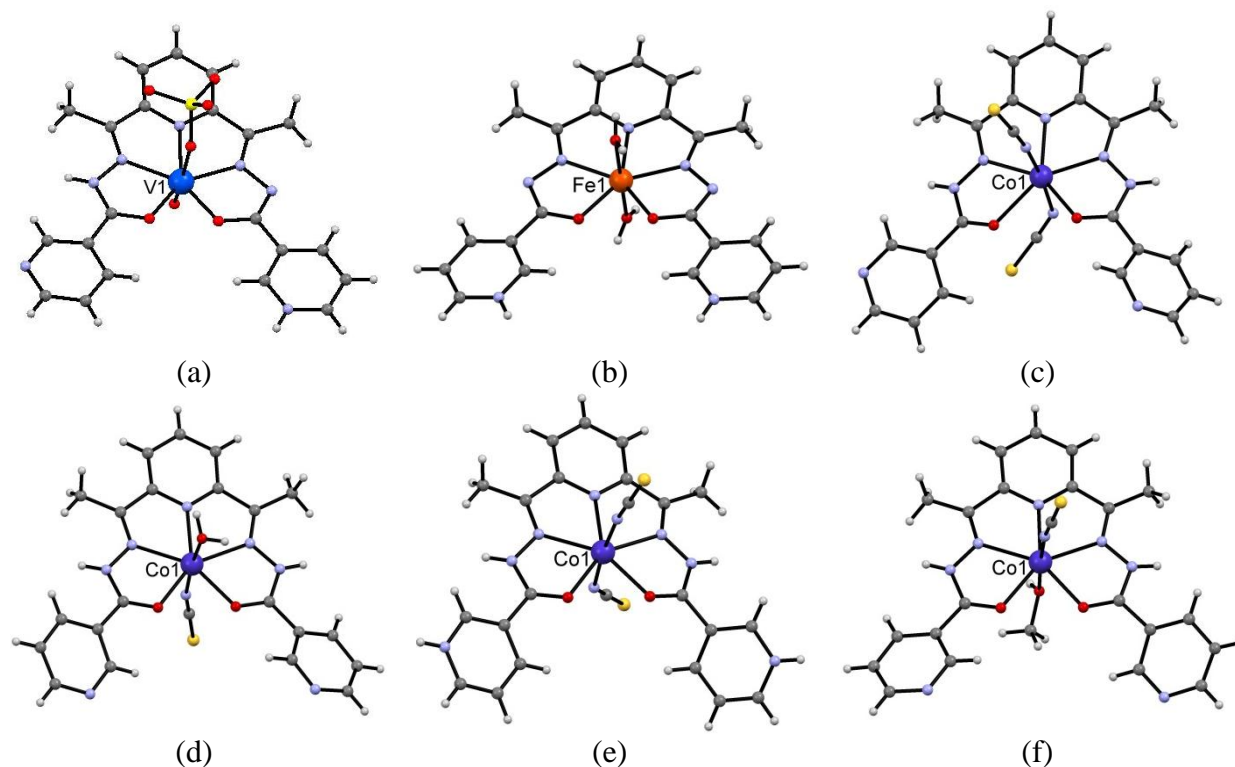


Fig. 1. View of the structure of mononuclear compounds in **1** (a) and **4** (c) and cations in **3** (b) and **5–7** (d–f).

In the molecular complex in **1** and complex cation in **3**, the axial positions are held by two O atoms of the SO_4^{2-} anion and oxo ligand O^{2-} in **1**, while in **3** the O atoms come from two water molecules. In compounds **4–7**, the axial vertices arise from: two N atoms of the NCS^- anions (in **4** and **6**); one N atom of the NCS^- anion and O atom of the water or methanol molecules (in compounds **5** and **7**). In coordination complexes **1**, **3–5**, and **7**, the Schiff base ligand coordinates in the neutral mode, while in complex cation **6**, the organic ligand is protonated at the nitrogen atoms of the terminal pyridine fragments. Analysis of the positioning of the hydrogen atoms from the H_2L ligand in **3** demonstrates the proton transfer from the N atoms of the amide group to the pyridine N atoms. In compounds **6** and **7**, the $[\text{Co}(\text{NCS})_4]^{2-}$ complex anion compensates for the positive charge of the Co^{2+} complex cation.

Complex **2** has an ionic structure; the crystals of it are composed of centrosymmetric binuclear cations $[\text{V}^{\text{II}}_2(\text{H}_2\text{L})_2]^{4+}$ (Fig. 2), NO_3^- anions, and crystal water molecules in a ratio of 1 : 4 : 1. The $[\text{V}^{\text{II}}_2(\text{H}_2\text{L})_2]^{4+}$ binuclear complex cation has a double helical structure in which two organic neutral H_2L ligands are coordinated to two metal atoms and lie along the V(1)-V(1') axis. The neutral H_2L ligand is coordinated to the V atom in a pentadentate mode: in a tridentate fashion through the electron-donating N,N,O-atoms and to the V(1') atom in a bidentate fashion through the N,O atoms. The coordination polyhedron of the V atom in complex **1** is a tetragonal pyramid. The basal plane of it is composed of the O and N atoms of one H_2L molecule and the one N atom of the symmetry-related counterpart; the pyramid is completed with the O atom of the other H_2L molecule as an apex. In the crystal, the complex cations and the anions are linked by intermolecular hydrogen bonds and by electrostatic interactions.

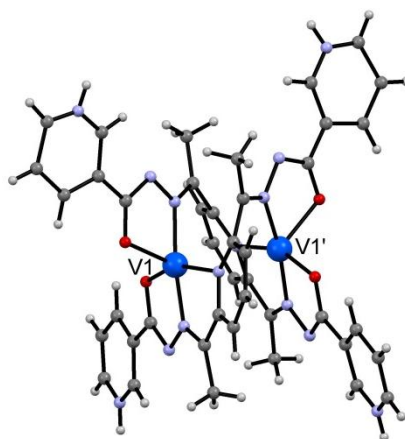


Fig. 2. View of the structure of the binuclear $[\text{V}^{\text{II}}_2(\text{H}_2\text{L})_2]^{4+}$ complex cation in **2**.

Except for compound **5**, all other solids contain voids in the crystal lattice filled with solvent guest molecules (H_2O , CH_3OH). The lattice solvents are held in the pores via hydrogen bonds with the coordination complex. The solvent accessible voids (SAVs) of the crystal unit cells were calculated by the PLATON program and are summarized in Table 1. The cumulative solvent volume varies from 5.4% in **6** to 18.2% in **1**. The SAVs assume the shapes of open channels in **1** and **4** and discrete cages in **2**, **3**, **6**, and **7**. Despite the fact that structure **5** represents a solvent-free solid, it contains negligible SAVs (~2.4% of the unit cell volume, V). The mass portions of the entrapped solvent along with numerical characteristics for the volume occupied by

the solvent molecules in the structures indicate that these solids may be considered to be possible sponge materials.

Table 1. Selected geometrical and crystal packing parameters in compounds **1-7**

| Compound | Space group | V, Å ³ | SAVs, Å ³ (%) | Solvent uptake, % | Reference, refcode in CSD |
|----------|-------------------------|-------------------|---------------------------|---|---------------------------|
| 1 | <i>P2₁/n</i> | 2727.6(2) | 497.0 (18.2) ^a | 13.75 ^{b,c} | [17], IXEYAN |
| 2 | <i>C2/c</i> | 5463.1(8) | 750.7 (13.7) ^a | 1.54 ^{b,c} | [17], IXIGED |
| 3 | <i>P2₁/n</i> | 3265.39(8) | 408.5 (12.5) ^a | 16.37 ^b ; 11.70 ^c | [18, 19], JAPLIY |
| 4 | <i>P-1</i> | 1296.98(12) | 108.0 (8.3) ^a | 5.26 ^{b,c} | [20], YECZIS |
| 5 | <i>C2/c</i> | 2631.1(3) | 63.6 (2.4) | 3.03 ^b ; - ^c | [20], YEFBIX |
| 6 | <i>P-1</i> | 1872.22(19) | 101.7 (5.4) ^a | 3.50 ^{b,c} | [20], YEDBER |
| 7 | <i>C2/c</i> | 6719.3(19) | 895.8 (13.3) ^a | 8.79 ^b ; 4.39 ^c | [20], YEFBOD |

^a SAVs calculated with the removal of guest molecules.

^b Total solvents' gravimetric uptake.

^c Non-coordinated solvents' gravimetric uptake.

IR spectra of the free H₂L ligand and compounds **1-7** were recorded in a range of 400-4000 cm⁻¹; the assignments of wavenumbers observed in the recorded spectra of the complexes, together with the wavenumbers of the ligand, are listed in Table 2. Some spectroscopic similarities are evident in the IR spectra of the ligand and all the compounds. In all complexes, the amide I, amide II, and amide III vibrational bands have undergone a slight shift upon the coordination effect. The displacement of the amide I band by 18-31 cm⁻¹ in compounds **4-7** in the direction to the low-frequency region against the ligand spectrum is probably the result of the coordinating C=O group effect at the metal. The spectra of compounds **1-3** exhibit broad bands in the region of 2700-2300 cm⁻¹, which can be attributed to ν(=NH⁺) vibrations [37] resulting from the proton migration from the NH groups to the nitrogen atoms of the terminal heterocycles.

Table 2. Vibrational wavenumbers of H₂L in compounds **1-7** (cm⁻¹)

| Compound | ν(OH), ν(N-H) | amide I, ν(C=O) | ν(C=N) azomet. | ν(CN) ring | amide II, δ _{NH+VC-N} | amide III |
|------------------|---------------|-----------------|-------------------|---------------|-----------------------------------|-----------|
| H ₂ L | 3182 | 1663 | 1617 | 1591 | 1567 | 1258 |
| 1 | 3384 | 1540 | 1633 | 1593 | 1571 | 1275 |
| 2 | 3348 | 1595 | 1617 | 1583 | 1558 | 1274 |
| 3 | 3381 | 1532 | 1632 | 1595 | 1566 | 1272 |
| 4 | 3467, 3180 | 1632 | 1646 | 1594 | 1538 | 1268 |
| 5 | 3331, 3155 | 1635 | 1657 | 1590 | 1570 | 1273 |
| 6 | 3346 | 1639 | 1605 | 1588 | 1572 | 1287 |
| 7 | 3551, 3445 | 1645, 1635 | 1661 | 1590 | 1570 | 1272 |

In compounds **1–3**, the Schiff base H₂L coordinates in the enol-form, while in **4–7** in the keto-form. The negative charges of the N atoms after proton migration probably cause the formation of pseudometalocycles MNCO, where distances of C=O bonds have intermediate values between single and double bonds (1.288 and 1.302 Å in **1**; 1.278 and 1.290 Å in **2**; 1.272 and 1.273 Å in **3**) similar to V(IV) and Fe(III) acetylacetonates [38, 39] and ammine-(*N*-(1-(4-chlorophenyl)-4,4,5,5,6,6,6-heptafluoro-3-oxohex-2-en-1-ylidene)benzene carboxy-drazonato-*N,O,O'*)-nickel(II) [40], which explain the different spectral behavior of C=O groups in the studied complexes.

3. Conclusions

The combination of 2,6-diacetylpyridine bis(nicotinoylhydrazone) (H₂L) with V(IV), Fe(III), and Co(II) salts has given rise to six mononuclear compounds (V(IV), Fe(III), Co(II)) and one binuclear complex (V(II)); in three of them, H₂L coordinates in the enol-form; in the other four compounds, the ligand exists in the keto-form. Six solids accommodate solvent molecules in the crystal lattice, while the mononuclear [V^{IV}(=O)(H₂L)(SO₄)]·5H₂O compound exhibits the most promising adsorptive properties.

Acknowledgements. The author thanks Dr. I.I. Bulhac and Dr. P.N. Bourosh for the fruitful discussion. This work was supported by project no. 15.817.02.18A.

References

- [1] A. Golcu, M. Tumer, H. Demirelli, and R. A. Wheatley, *Inorg. Chim. Acta* 358, 1785 (2005).
- [2] U. El-Ayaan and A. A.-M. Abdel-Aziz, *Eur. J. Med. Chem.* 40(12), 1214 (2005).
- [3] M. Sönmez, I. Berber, and E. Akbas, *Eur. J. Med. Chem.* 41(1), 101 (2006).
- [4] N. Shahabadi, Z. Ghasemian, and S. Hadidi, *Bioinorg. Chem. Appl.*, 9 (2012).
- [5] N. Galić, M. Rubčić, K. Magdić, M. Cindrić, and V. Tomišić, *Inorg. Chim. Acta* 366, 98 (2011).
- [6] A. Hameed, M. al-Rashida, M. Uroos, S. A. Ali, and K. M. Khan, *Expert. Opin. Ther. Pat.* 27(1), 63 (2017).
- [7] N. P. Belskaya, W. Dehaen, and V. A. Bakulev, *Arkivoc* 1, 275 (2010).
- [8] E. P. McMoran, J. A. Goodner, D. R. Powell, and L. Yang, *Inorg. Chim. Acta* 421, 465 (2014).
- [9] A. Bonardi, C. Carini, C. Merlo, C. Pelizzi, G. Pelizzi, P. Tarasconi, and F. Vitali, *J. Chem. Soc., Dalton Trans.* 0(9), 2771 (1990).
- [10] A. Bonardi, C. Merlo, C. Pelizzi, G. Pelizzi, P. Tarasconi, and F. Cavatorta, *Chem. Soc., Dalton Trans.* 0(4), 1063 (1991).
- [11] L. S. Vojinović-Ješić, V. I. Češljević, G. A. Bogdanović, V. M. Leovac, K. Mészáros-Szécsényi, V. Divjaković, and M. D. Joksović, *Inorg. Chem. Commun.* 13, 1085 (2010).
- [12] S. Naskar, D. Mishra, S. K. Chattopadhyay, M. Corbella, and A. J. Blake, *Dalton Trans.* 14, 2428 (2005).
- [13] R. Pedrido, M. J. Romero, M. R. Bermejo, A. M. González-Noya, M. Maneiro, M. J. Rodríguez, and G. Zaragoza, *Dalton Trans.* 44, 5304 (2006).
- [14] A. Panja, C. Campana, C. Leavitt, M. J. Van Stipdonk, and D. M. Eichhorn, *Inorg. Chim. Acta* 362, 1348 (2009).

- [15] B. A. D. Neto, B. F. L. Viana, T. S. Rodrigues, P. M. Lalli, M. N. Eberlin, W. A. da Silva, H. C. B. de Oliveira, and C. C. Gatto, *Dalton Trans.* 42(32), 11497 (2013).
- [16] C. R. Groom, I. J. Bruno, M. P. Lightfoot, and S. C. Ward, *The Cambridge structural database, Acta Crystallogr. B*72, 171 (2016).
- [17] P. Bourosh, I. Bulhac, A. Mîrzac, S. Shova, and O. Danilescu, *Russ. J. Coord. Chem.* 42(3), 157 (2016).
- [18] I. Bulhac, A. Deseatnic-Ciloci, P. Bourosh, J. Tiurina, O. Bologna, C. Bivol, S. Clapco, A. Verejan, S. Labliuc, and O. Danilescu, *Chem. J. Mold.* 11(1), 39 (2016).
- [19] I. Bulhac, A. Deseatnic-Ciloci, L. Cuba, C. Bivol, O. Danilescu, E. Dvornina, and P. Bouroş, *Proc. Int. Conf. on Modern Technologies in the Food Industry, Chisinau*, 348 (2016).
- [20] I. Bulhac, O. Danilescu, A. Rija, S. Shova, V. Ch. Kravtsov, and P. N. Bourosh, *Russ. J. Coord. Chem.* 43(1), 21 (2017).
- [21] S. Naskar, D. Mishra, A. J. Blake, and S. K. Chattopadhyay, *Struct. Chem.* 18, 217 (2007).
- [22] L. S. Vojinović-Ješić, V. I. Češljević, G. A. Bogdanović, V. M. Leovac, K. M. Szécsényi, V. Divjaković, and M. D. Joksović, *Inorg. Chem. Commun.* 13, 1085 (2010).
- [23] F. Schleife, A. Rodenstein, R. Kirmse, and B. Kersting, *Inorg. Chim. Acta* 374, 521 (2011).
- [24] P. Nithya, J. Simpson, and S. Govindarajan, *Polyhedron* 141, 5 (2018).
- [25] G. Bradan, A. Pevec, I. Turel, I. N. Shcherbakov, M. Milenković, M. Milenković, D. Radanović, B. Čobeljić, and K. Anđelković, *J. Coord. Chem.* 69(18), 2754 (2016).
- [26] A. Kriza, L. V. Ababei, N. Cioatera, I. Rau, and N. Stanica, *J. Serb. Chem. Soc.* 75(2), 229 (2010).
- [27] R. K. Agarwal, D. Sharma, L. Singh, and H. Agarwal, *Bioinorg. Chem. Appl.* 2006, 1 (2006).
- [28] G. Durgaprasad and C. C. Patel, *Indian J. Chem.* 11(12), 1300 (1973).
- [29] S. A.-M. Khlood, *Spectrochim. Acta A*, 70, 162 (2008).
- [30] C. Pelizzi, G. Pelizzi, G. Predieri, and S. Resola, *J. Chem. Soc., Dalton Trans.* 0(7), 1349 (1982).
- [31] C. Pelizzi, G. Pelizzi, and F. Vitali, *Transit. Metal Chem.* 11, 401 (1986).
- [32] D. Delledonne, G. Pelizzi, and C. Pelizzi, *Acta Crystallogr. C*43, 1502 (1987).
- [33] A. Mangia, C. Pelizzi, and G. Pelizzi, *Acta Crystallogr. B*30, 2146 (1974).
- [34] A. Bonardi, S. Ianelli, C. Pelizzi, G. Pelizzi, and C. Solinas, *Inorg. Chim. Acta* 187(2), 167 (1991).
- [35] P. Mazza, F. Zanni, M. Orcesi, C. Pelizzi, G. Pelizzi, and G. J. Predieri, *Inorg. Biochem.* 48, 251 (1992).
- [36] S. Naskar, M. Corbella, A. J. Blake, and S. K. Chattopadhyay, *Dalton Trans.* 11, 1150 (2007).
- [37] L. Bellami, *IK Spektry slozhnykh molekul (IR Spectra of Complex Molecules)*, Izd-vo Inostrannaya Literatura, Moscow, 1963.
- [38] M. Hoshino, A. Sekine, H. Uekusa, and Y. Ohashi, *Chem. Lett.* 34(9), 1228 (2005).
- [39] E. Arslan, R. A. Lalancette, and I. Bernal, *Struct. Chem.* 28, 201 (2017).
- [40] K. G. Avezov, S. I. Yakimovich, B. B. Umarov, V. V. Pakal'nis, G. G. Aleksandrov, T. N. Niyazkhanov, N. G. Sevinchov, and N. A. Parpiev, *Russ. J. Coord. Chem.* 37(4), 275 (2011).

METAL OXIDE GAS SENSORS: DEVELOPMENT AND CHARACTERIZATION

Lidia Ghimpu

*Ghitu Institute of Electronic Engineering and Nanotechnologies,
Academy of Sciences of Moldova, Academiei str. 3/3, Chisinau, MD-2028 Republic of Moldova
E-mail: lidia.ghimpu@gmail.com*

(Received June 29, 2018)

Abstract

In this review, a number of oxide materials deposited on optical fibers have been studied to determine the most optimum materials for the production of optical sensors intended for the detection of petroleum gases, namely, butane, ammonia, and ethanol. The sensory properties of oxides materials, such as ZnO, TiO₂, and SnO₂, with different thicknesses have been described. First, the magnetron sputtering of zinc oxide and titanium dioxide have been described; second, the results of a study of the morphology and sensing characteristics of the optical fiber sensors have been discussed. The fabrication route of liquid petroleum gas (LPG) optical sensors based on optical fibers coated with ZnO, TiO₂, and SnO₂ nanocrystalline films has been analyzed. It has been shown that, after annealing of nanocrystalline ZnO films, the sensitivity increases. The prepared sensors exhibit a sensitivity of 2.77% for ZnO and 24.4% for TiO₂.

1. Introduction

The sensing capacity of materials can be greatly increased by reducing their size down to the nanometer scale. This can presumably be implemented through the preparation of nanocrystalline nanodots, nanowires, nanofibers, and nanowebs.

Zinc oxide (ZnO) is a key functional material exhibiting near-ultraviolet emission, semiconducting, magnetic, and piezoelectric properties. Thus, ZnO is one of the wide band-gap metal oxides that are of great interest for versatile applications [1]. Zinc oxide has a wide band gap of 3.37 eV and a large exciton binding energy of 60 meV at room temperature. Dye sensitized single-crystal zinc oxide electrodes were studied by Gerischer and Tributsch as early as 1969 [2–4]. The semiconductor sensor type belongs to the class of solid state gas sensors. In the presence of a determinate gas, the conductivity of the sensing material undergoes changes. The working temperature at which these devices are more efficient can vary depending on the gas atmosphere and properties of the sensor material selected in every case. Metal oxide semiconductor gas sensors detect a wide variety of gases [7–13]. The main advantage of metal oxide sensors is their life time. Theoretically, in clean applications, it can be 10 years or more. A metal oxide sensor consists of three main components, namely, a sensing material, electrodes, and a heater [14–20]. The commonly used sensing materials include SnO₂, TiO₂, ZnO, or In₂O₃. Zinc oxide gas sensors have good characteristics, such as chemical sensitivity to different adsorbed gases, amenability to doping, high chemical stability, nontoxicity, and low cost.

2. Experimental

Thin layers of metal oxides were deposited by RF magnetron sputtering. The parameters of the RF magnetron sputtering technique are the specific power of the magnetron, the gas pressure in the working chamber, the substrate temperature, and the gas flow rate. The main advantages of this technique are the deposition rate and high reproducibility of the composition of the deposited materials. The deposition rate of RF magnetron sputtering depends on the power of the magnetron, gas pressure in the working chamber, and the substrate temperature. This method and optical properties are described in detail in [5, 6].

The use of RF magnetron sputtering provided the growth of ZnO, SnO₂, and TiO₂ layers in argon atmosphere. A disc of 99.99 % pure zinc served as a target for ZnO layers; a disc of 99.9% pure TiO₂ was used for TiO₂ layers. For a layer of SnO₂, a disc of 99.99% pure SnO₂ was used as a target. The fiber tip was firstly cut by using a manual cleaver and then washed in a mixed solution of potassium dichromate (7 g of K₂Cr₂O₇, 10 mL of H₂O, 100 mL of H₂SO₄) at room temperature. Afterwards, substrate cleaning was followed by rinsing with an abundant distilled water flow (18.2 MΩ cm). Next, the substrates were mounted on a substrate holder equipped with a resistive heater. The distance between the substrate and the ZnO, TiO₂, and SnO₂ was 8 cm. Initially, the chamber was evacuated to a background pressure of 1.2×10^{-6} Torr. The argon (Ar) working gas pressure was monitored so as to maintain a constant vacuum pressure of 6.3×10^{-3} mbar. Film thickness was controlled by using an MTM-10/10A High Resolution thickness monitor quartz microbalance during sputtering. High-purity Ar gas (99.99%) was used for ion bombardment; the argon flow rate of 60 mL/min was controlled by means of a valve at a base pressure of 6.3×10^{-3} mbar. The ZnO, TiO₂, and SnO₂ films were deposited at a temperature of 110°C for 10–30 min under deposition conditions, i.e., a pressure and power of 200 W. The substrate temperature was 30°C in all cases. A schematic of oxide deposition on the top of an optical fiber is show in Fig. 1a.

The response toward butane was monitored by placing the sensors in a custom designed test chamber. This setup is constituted by two lines: the first one for butane and the second one for an inert gas (nitrogen). In the butane channel, a mixture of nitrogen and butane flows with 1 vol % of butane in nitrogen. The gas flow is tuned using a Mass Flow Controller (MFC). The line reaching the chamber is thus divided into two sublimes: the first that contains a low flow range MFC (50 sccm) and the second that contains a high flow range MFC (500 sccm). The butane concentration fluxed in the test chamber (chamber volume of about 0.8 L) is controlled and monitored using the MFC.

The TiO₂ and ZnO coated optical fibers were placed in the test chamber and exposed to LPG taken in different concentrations. Before tests, the fibers were stored in the test chamber for a few minutes to obtain a stable signal. After the signal stabilization, the LPG line was opened to allow the gas to flow into the test chamber until the achievement of a plateau value. The chamber was emptied from the residual LPG via fluxing pure nitrogen until the restoration of the initial value.

The proposed optical sensors are based on the deposition of properly chosen sensitive materials as nanoscale films on the distal end of standard silica single-mode optical fibers as shown in Fig. 1b.

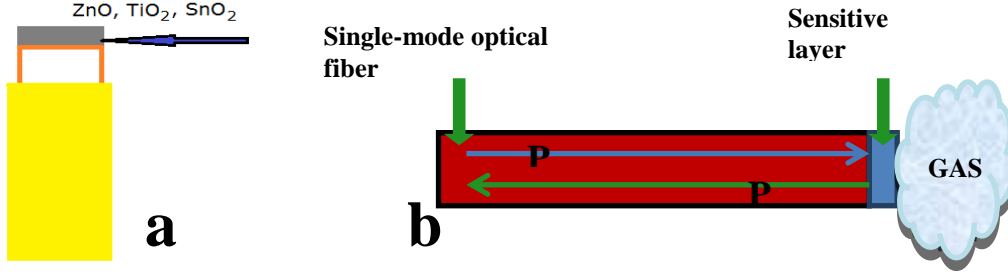


Fig. 1. Schematic of the optoelectronic sensor device: (a) schematic oxide deposition on the top of the optical fiber and (b) an optical fiber/oxide layer to interact with the gas.

3. Results and Discussion

The principle of operation is based on the dependence of reflectance on the optical and geometric properties of the overlay deposited on the optical fiber. This means that any change occurring in the features of the overlay due to the chemical sorption of a certain analyte would induce a consequent change in the fiber reflectance according to the following equation:

$$R_{fiber-film} = \left| \frac{r_{12} + r_{23} \cdot e^{i\beta}}{1 + r_{12} r_{23} \cdot e^{i\beta}} \right|^2 \quad (1)$$

with

$$r_{12} = \frac{\sqrt{\epsilon_{eff}} - \sqrt{\tilde{\epsilon}_{film}}}{\sqrt{\epsilon_{eff}} + \sqrt{\tilde{\epsilon}_{film}}}; \quad r_{23} = \frac{\sqrt{\tilde{\epsilon}_{film}} - \sqrt{\epsilon_{ext}}}{\sqrt{\tilde{\epsilon}_{film}} + \sqrt{\epsilon_{ext}}}; \quad \beta = \frac{2\sqrt{\tilde{\epsilon}_{film}} \cdot d_{film}}{\lambda}$$

where ϵ_{eff} and ϵ_{ext} are the optical fiber and external medium dielectric functions; λ is the optical wavelength; $\tilde{\epsilon}_{film} = \epsilon'_{film} + j\epsilon''_{film}$ and d_{film} represent the complex dielectric function and the thickness of the sensitive layer, respectively.

3.1. Electronic Configuration

Reflectance measurements will be performed by lighting the sensing fiber with a superluminescent diode (40-nm band width) operating at a wavelength of 1310 nm. A 2×2 optical fiber coupler was used to measure the optical power emitted by the source, providing well compensated intensity measurements. Figure 2a shows a block diagram for the electronic setup of the sensor and a real image of the components.

To enhance the system performance, synchronous detection was implemented with the light source amplitude externally modulated at 500 Hz and the sensor outputs retrieved by using a dual channel lock-in amplifier. The optoelectronic sensor output consists of the signal reflected from the fiber coated end divided by the source signal; it is proportional only to the fiber–film interface reflectance:

$$I_{out} = k \cdot R_{fiber-film} \quad (2)$$

where k is a constant taking into account all the setup parameters and $R_{\text{fiber-film}}$ is the function of the fiber and external medium dielectric functions, the operating wavelength and the optical and geometric properties of the sensitive film. In this configuration, any effect capable of modifying the complex dielectric function of the sensitive layer changes the normalized output of the optical sensor. A multichannel fiber optic switch was used to provide a simultaneous monitoring of up to eight SOF sensors. The optical data were stored in a notebook controlling the sensing process in LabView software ambient by means of a NI-DAQ card.

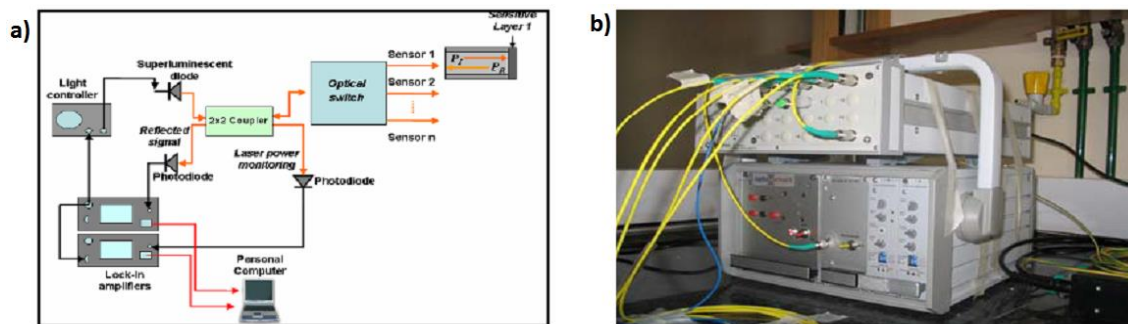


Fig. 2. Electronic setup of the optoelectronic sensor.

The overall set up is showed in Fig. 2b. It demonstrates how the overall setup was properly engineered to provide robust compact portable equipment.

Different types of materials were tested: ZnO, TiO₂, and SnO₂ coated optical fibers. Therefore, results of the morphological and optical studies of the tested fibers will be described.

Optical fibers coated with 200-nm-thick ZnO. The fiber was tested using a refractometer to study the sensing behavior toward three different gases: butane, ethanol, and ammonia. It is evident from Fig. 3a that the butane sensibility is low at a really low signal/noise ratio.

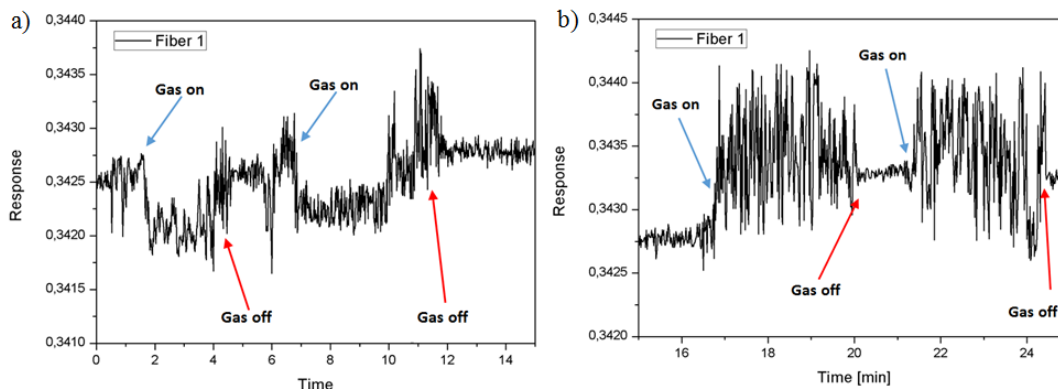


Fig. 3. ZnO-1 with a thickness of 200 nm: (a) butane and (b) ethanol sensing behavior.

A similar behavior was observed for the ethanol sensing properties of the fiber. The ethanol sensibility is low, and the signal/noise ratio is lower than that in the butane test: in fact, in the presence of ethanol, there is only an increase in the oscillation amplitude due to noise; however,

the baseline does not change appreciably. Tests with ammonia cannot be considered as sensing behavior tests, because there is a reaction between the material under study and the ammonia vapors, as shown in Fig. 4. Another evidence of the reaction is the change in the color of the material—from black to white.

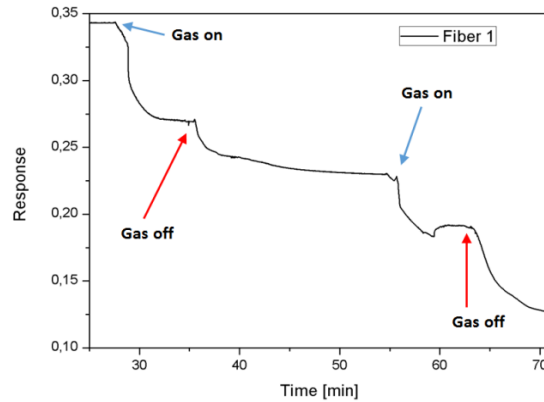


Fig. 4. ZnO-1 with a thickness of 200 nm: ammonia test.

Similar tests were performed for the second fiber; in this case, the butane sensibility and the signal/noise ratio are higher than those of fiber #1. It is evident from Fig. 5a that, after the first exposure to butane, there is a change in the baseline value, which is higher than in the case of the unexposed fiber. This value does not change after a night at room temperature; this fact can suggest that some of the butane molecules cannot be desorbed from the sensible layer at room temperature. A similar trend is observed in Fig. 5b, which shows the ethanol sensing behavior of the material under test.

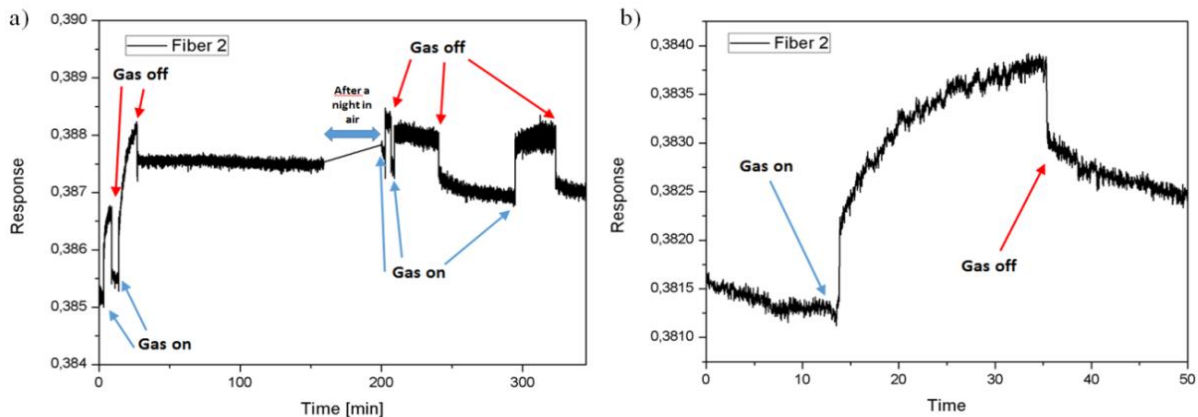


Fig. 5. Behavior of ZnO-2 with a thickness of 200 nm: (a) butane and (b) ethanol sensing.

Despite the promising butane and ethanol sensing behavior of the second ZnO coated fiber, in this case, the material also reacts with the ammonia vapors, as shown in Fig. 6. This figure shows an optical micrograph relative to the film after exposure to ammonia: white regions that correspond to the reacted areas are visible.

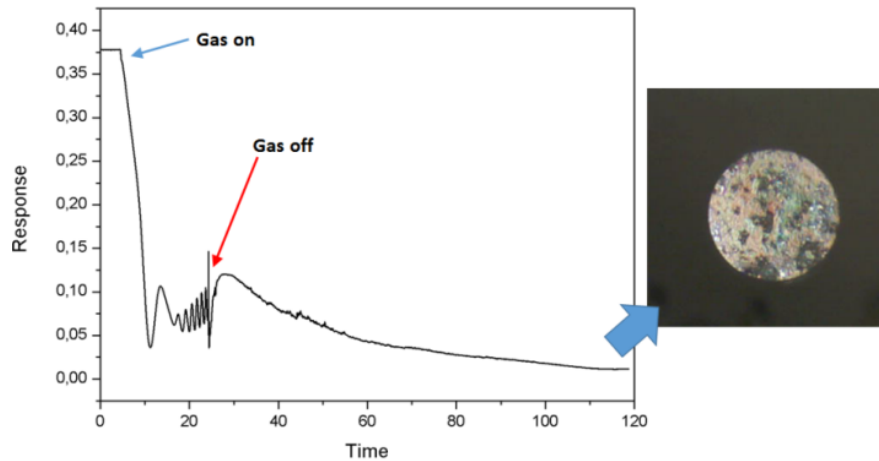


Fig. 6. Fiber/ZnO-2 ammonia test and optical micrograph of the reacted film.

To improve the sensibility of the inorganic layer, the third fiber was subjected to an annealing process. Figure 7 shows the butane sensing properties of the fiber under study before annealing; it is evident that the sensibility toward butane and the signal/noise ratio are high without annealing; it is of interest that tests were also performed in the presence of butane taken in different concentrations and had remarkable results.

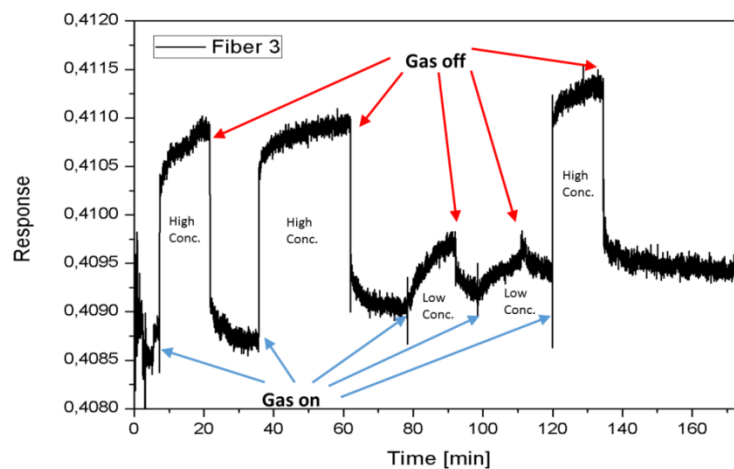


Fig. 7. Fiber/ZnO-3 butane sensing behavior ($d = 200$ nm).

In addition, the absorption curve of the fiber exposed to ethanol (Fig. 8) indicates a high sensibility toward this vapor. In both cases (exposure to butane and ethanol), the signal does not come back to the initial value; this behavior is similar to that observed for the second fiber; it suggests that the vapor molecules cannot be desorbed completely at room temperature.

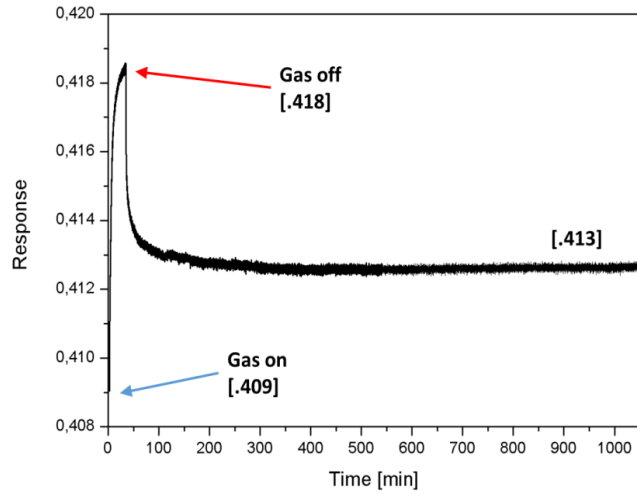


Fig. 8. Fiber/ZnO-3 ethanol sensing behavior ($d = 200$ nm).

The annealing process induces a lowering of the baseline, probably due to an increase of the refractive index of the material. After 50 min of annealing to 150°C , the signal is reduced by about 12%, as shown in Fig. 9a.

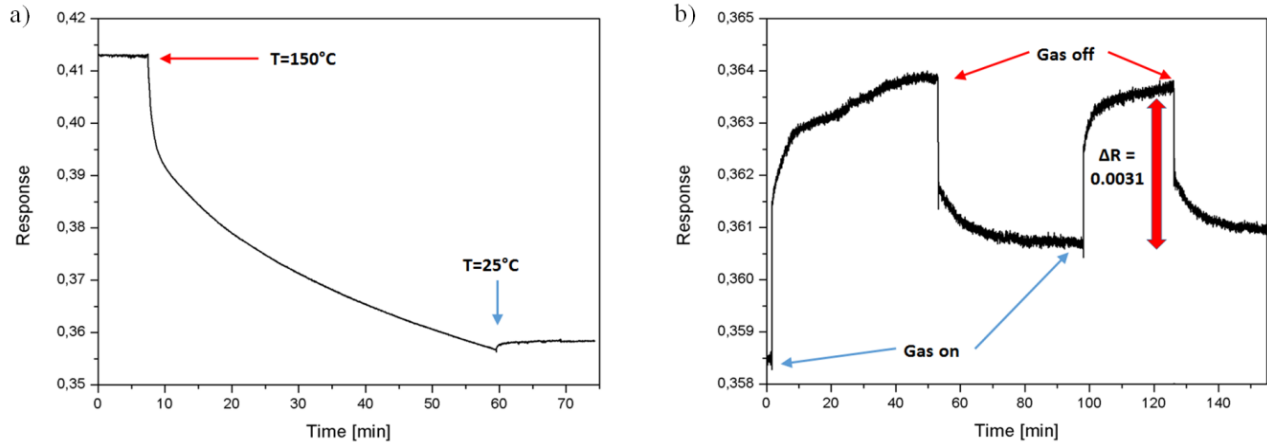


Fig. 9. Fiber/ZnO-3: (a) first annealing and (b) butane sensing behavior after annealing ($d = 200$ nm).

After the first annealing process, the fiber was exposed to butane vapors to verify the possible sensibility variations. For this purpose, sensibility S (%) was introduced; it is defined as follows:

$$S (\%) = \Delta R / R_0 \cdot 100, \quad (3)$$

where ΔR is the total signal variation in the presence of the gas and R_0 is the signal just before the gas exposure. The annealing increases the sensibility toward butane: in fact, the maximum signal variation before annealing was 0.52% against 0.87 % after annealing.

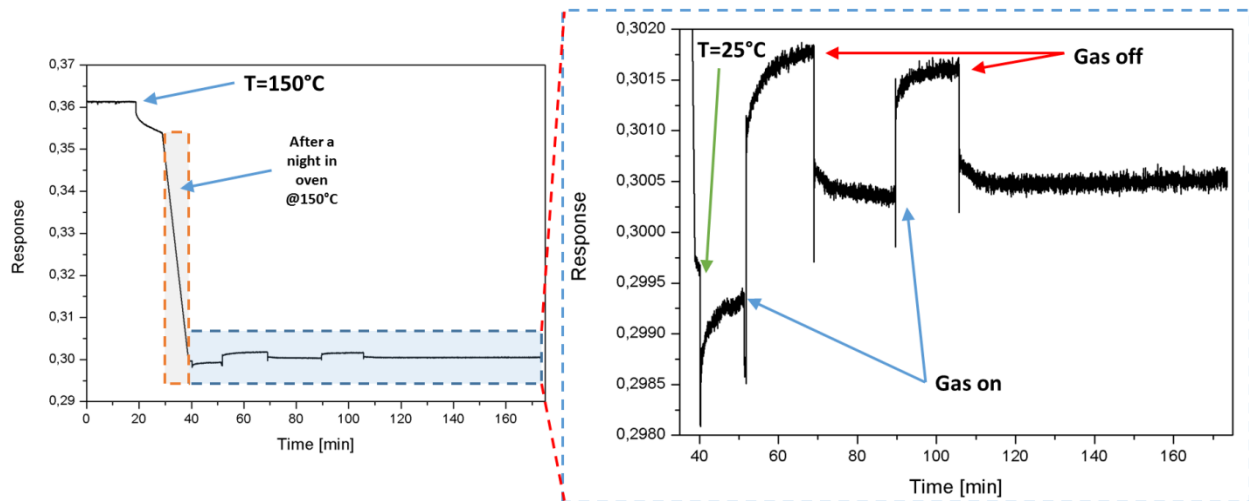


Fig. 10. Fiber/ZnO-3: the second annealing process followed by a test with butane.

The second annealing process was carried out until reaching a plateau value: during a whole night to 150°C, the baseline value changed from 0.360 to 0.299 with a total variation (first and second annealing process) of about 27%.

Figure 11 shows that, before annealing in the fourth fiber, the butane sensibility and the signal/noise ratio are low. Moreover, it is evident that the exposure to butane induces a decrease in the signal intensity, as in the case of fiber #1. On the basis of this result, the fiber was annealed to 150°C for about 4 h; the total decrease in the signal value was about 13%.

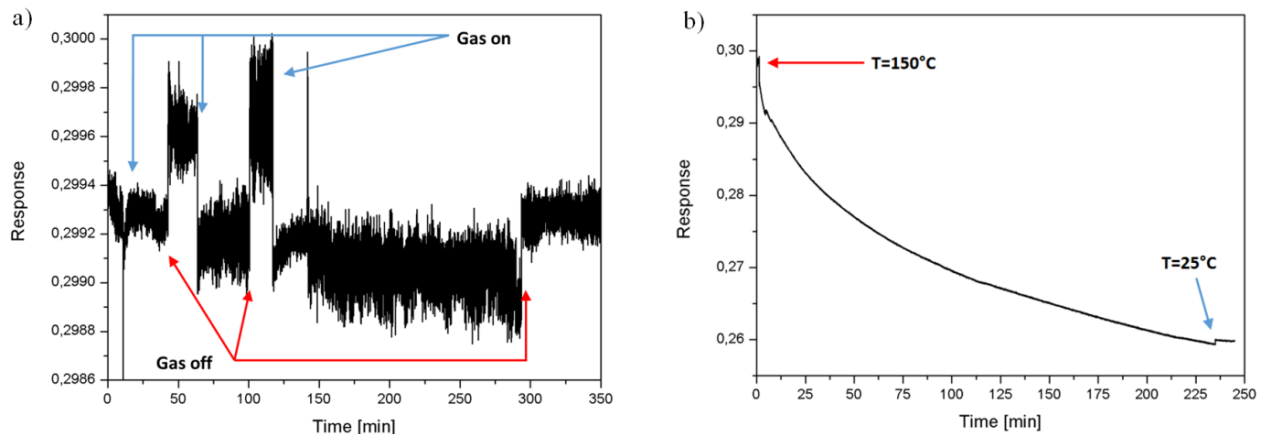


Fig. 11. Fiber/ZnO-4: (a) butane sensing behavior before annealing and (b) subsequent annealing process.

The morphological changes of the material before and after the annealing process were studied by atomic force microscopy (AFM) combined with optical microscopy. The results are shown in Figs. 12 and 13.

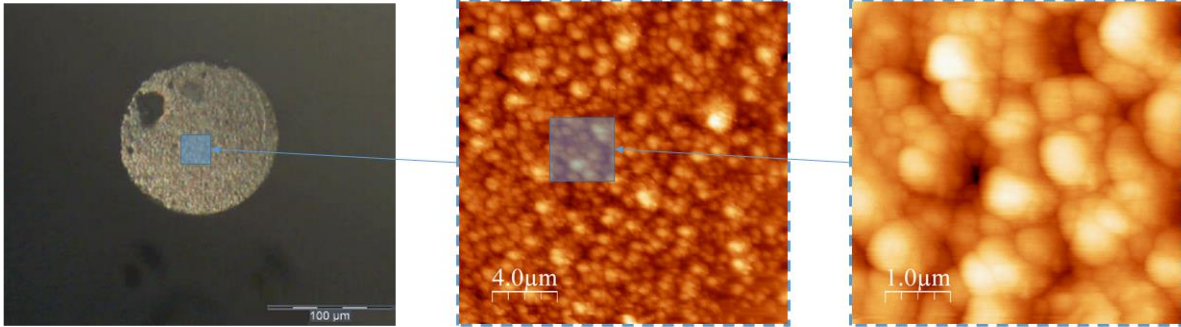


Fig. 12. Fiber/ZnO-4: an optical micrograph and respective AFM zooms before annealing.

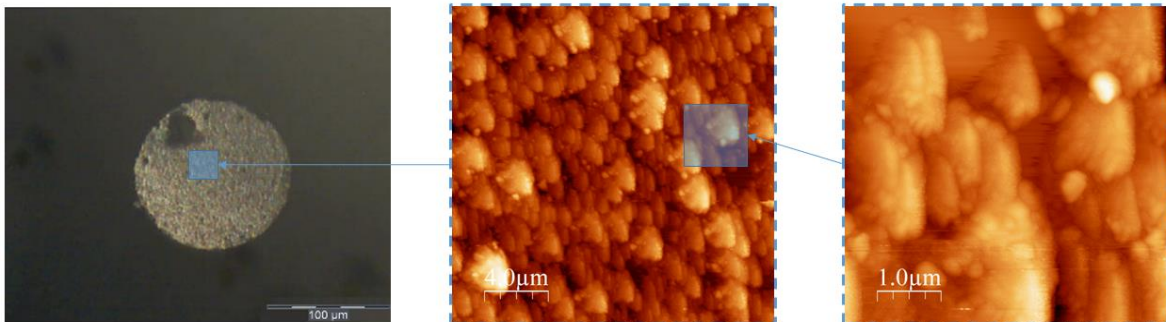


Fig. 13. Fiber/ZnO-4: an optical micrograph and respective AFM zooms after annealing.

It is shown that the annealing process induces the growth on the ZnO grains, which become larger than the grains before annealing. This effect can be attributed to (i) the coalescence of the preannealed smaller grains and (ii) the oxidation of metallic Zn deposited together with ZnO. After annealing, a remarkable increase in the butane sensibility is observed; however, the exposure to butane still induces a decrease in the signal intensity. Figure 14 shows a different behavior with respect to the last “gas off”: in this case (green arrow), the butane was not forced to leave the test chamber; instead, it left the chamber naturally owing to opening the chamber taps. It is of interest that the signal always comes back to the same value after each exposure.

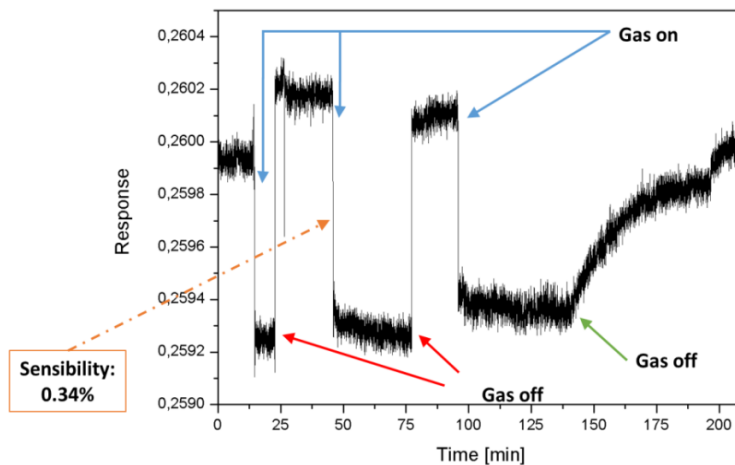


Fig. 14. Fiber/ZnO-4: butane sensing behavior after annealing.

For 4 consecutive days, the fiber under test was exposed to ammonia vapors; despite the annealing process, the inorganic film continued to react with ammonia. Figure 15 shows that there is no reproducibility of the data relative to the exposure to ammonia.

Figure 16 shows the appearance of the optical fiber after exposure to ammonia. It is evident that there is a remarkable difference between the layers before and after exposure to ammonia at both the macroscopic and microscopic levels.

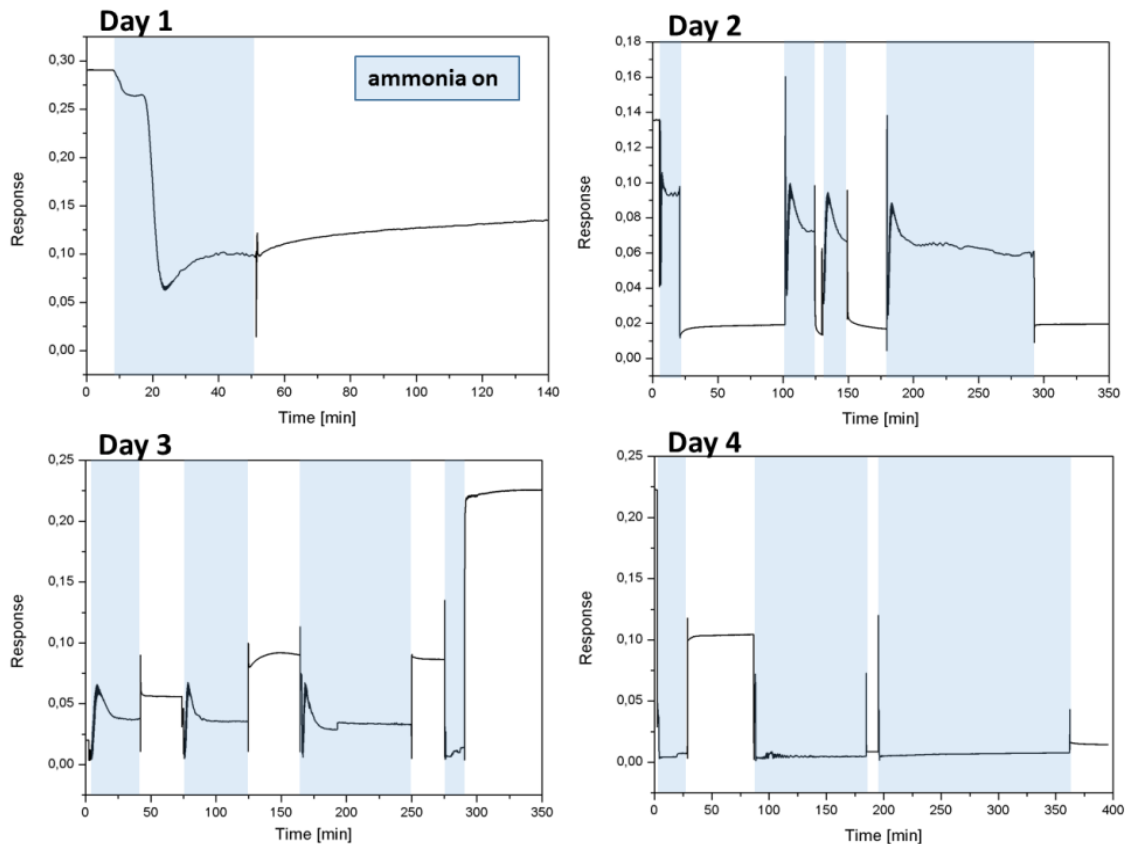


Fig. 15. Fiber/ZnO-4: ammonia test.

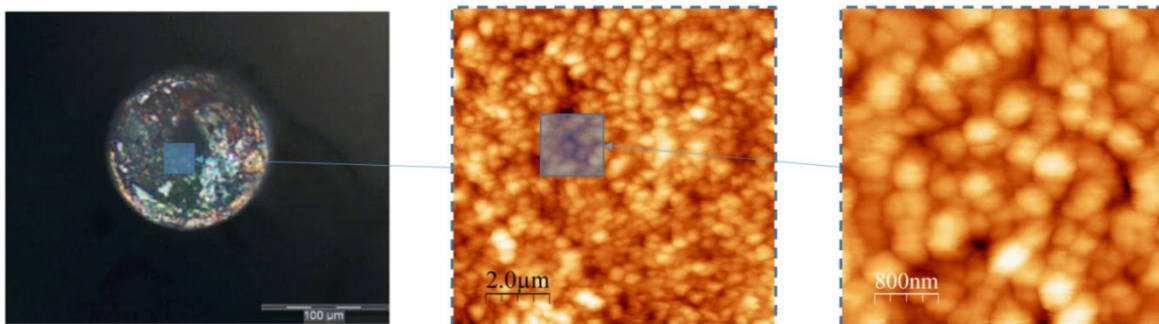


Fig. 16. Fiber/ZnO-4: an optical micrograph and respective AFM zooms after exposure to ammonia.

Annealing of 250-nm-thick zinc oxide fiber/ZnO-5-9. This subset was prepared to study the effect of the annealing time on the zinc oxide sensing properties; sample characteristics are shown in the table.

Annealing parameters of the ZnO layer deposited on optical fibers

| Fiber | Material | Thickness [nm] | Annealing time | Figure |
|-------|----------|----------------|----------------|--------|
| 5 | ZnO | 250 | 5 min | 17 |
| 6 | ZnO | 250 | 10 min | 18 |
| 7 | ZnO | 250 | 1 min | 19 |
| 8 | ZnO | 250 | 30 s | 20 |
| 9 | ZnO | 250 | 30 s | 20 |

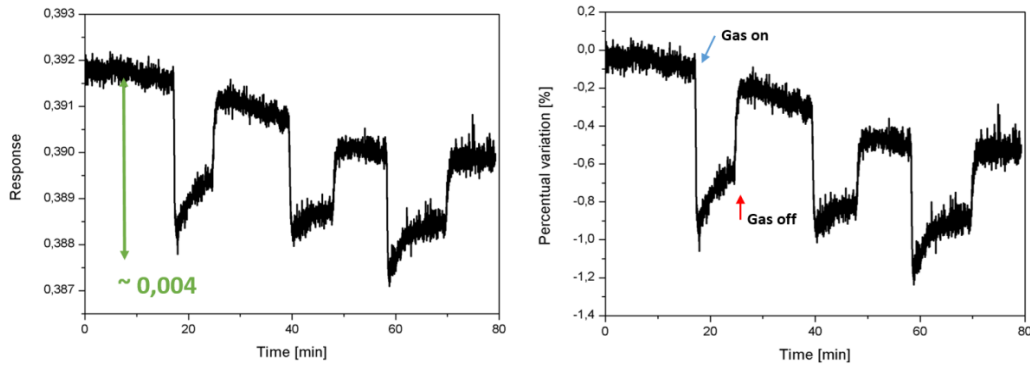


Fig. 17. Fiber #5: butane sensing behavior.

Fiber #5 (Fig. 17) prepared at an annealing time of 5 min shows a maximum variation of about 1%; the signal is stable with a slight reduction of the baseline.

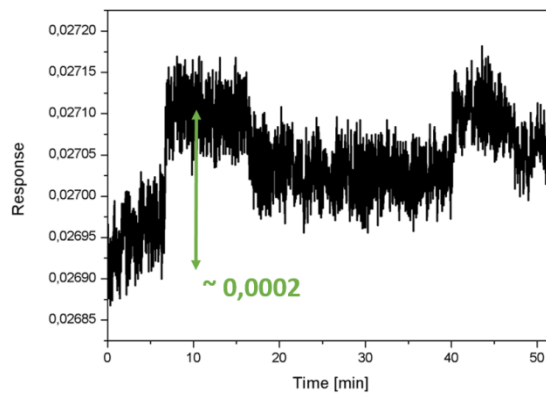


Fig. 18. Fiber #6: butane sensing behavior.

Fiber #6 (Fig. 18) prepared at an annealing time of 10 min shows a low baseline value (~ 0.026) at a low signal/noise ratio; consequently, the butane sensibility is extremely low.

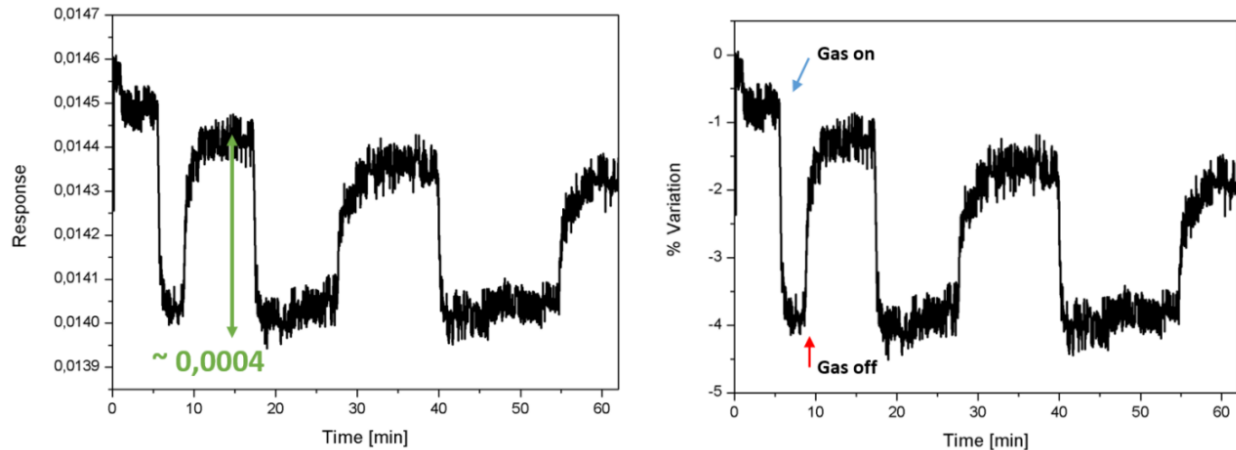


Fig. 19. Fiber #7: butane sensing behavior.

The signal obtained with fiber #7 (Fig. 19) is stable; the signal/noise ratio is good; for this reason, although the baseline value is low (~ 0.0146), the sensibility toward butane is high.

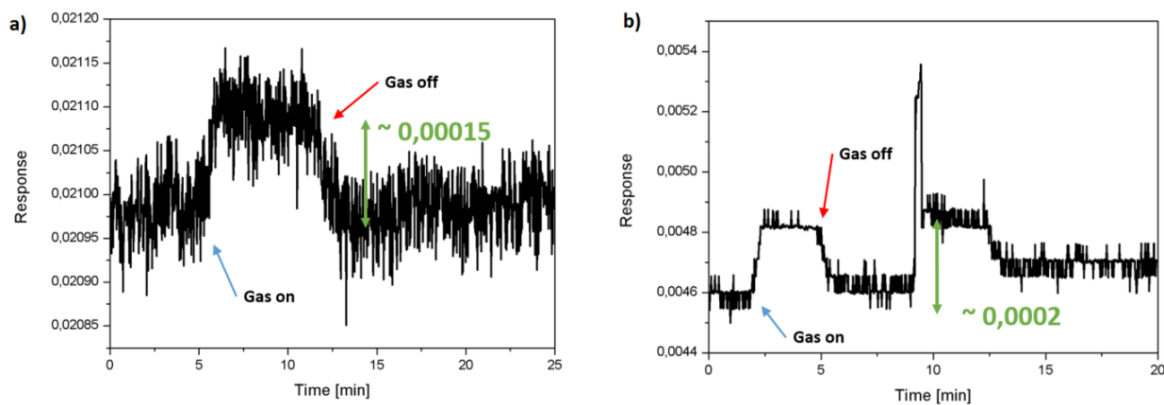


Fig. 20. Butane sensing behavior: (a) fiber #8 and (b) fiber #9.

The baseline and signal/noise ratio values of fibers #8 and #9 (Fig. 20) are too low to obtain a good butane sensor; it is yet not clear whether the poor quality of sensors #8 and #9 is attributed to the short annealing time (30 s) or to the fiber cut.

Optical fibers coated with 250-nm-thick TiO₂. Titanium dioxide is the second material tested using a refractometer. Figure 21 shows that the response of this material is remarkably higher than that of the previously analyzed zinc oxide: in fact, the sensibility of TiO₂ is two orders higher—about 13%. Moreover, exposure to butane induces a decrease in the signal, similarly to ZnO fibers #1 and #4.

The annealing process induces an increase in the baseline value, as shown in Fig. 22a. This process is performed to 150°C; the results are faster than in the case of zinc oxide: titanium dioxide reaches a plateau value after about 45 min, while zinc oxide requires an entire night at a high temperature.

After annealing, there is a remarkable increase in sensibility, which achieves a value of about 24%, as shown in Fig. 22b.

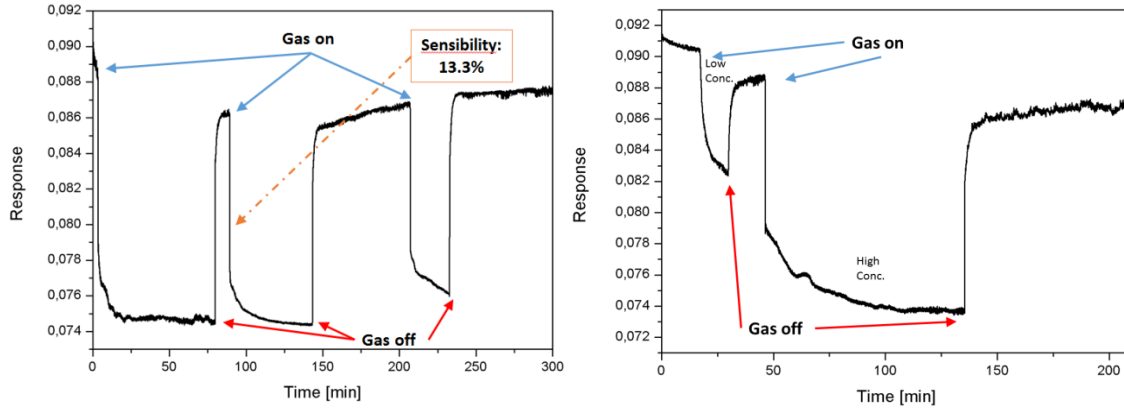


Fig. 21. Fiber #6: butane sensing behavior before annealing.

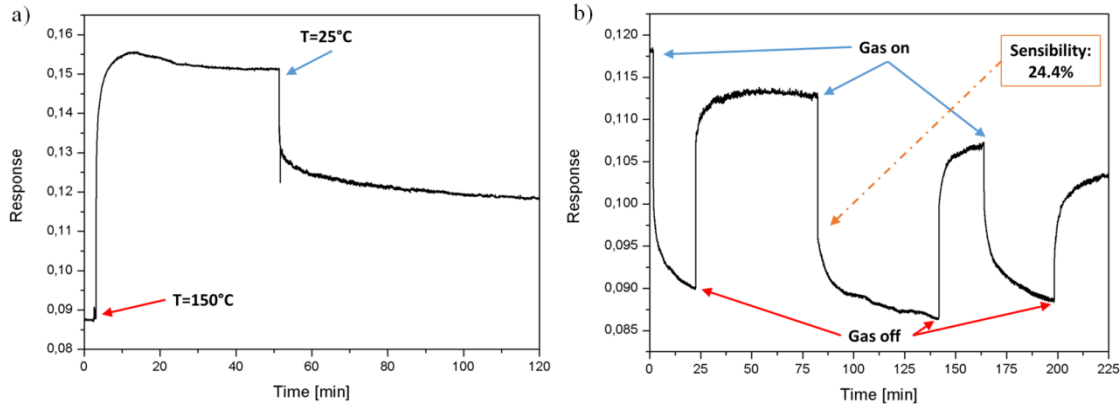


Fig. 22. Fiber #6: (a) annealing and (b) butane sensing behavior after annealing, $d = 250$ nm.

Titanium dioxide with a thickness of 300 nm. Similarly to the TiO_2 sample in the first set, fiber #2 showed a good response to butane vapors, as shown in Fig. 23a. Figure 23b shows the percentage variation of the fiber in the presence of butane vapors: the percentage variation ($\%V(t)$) is calculated for each point of the curve and expressed as follows:

$$\%V(t) = \frac{R_t - R_0}{R_0} \times 100 \quad (4)$$

where R_t is the response at moment t and R_0 is the plateau value of the sensor in the absence of a gas; the maximum $\%V$ value is 0.5%; it is lower than the value obtained for fiber #6 of 250-nm-thick TiO_2 (13.3%); this behavior can be attributed to the different thicknesses of the TiO_2 layer.

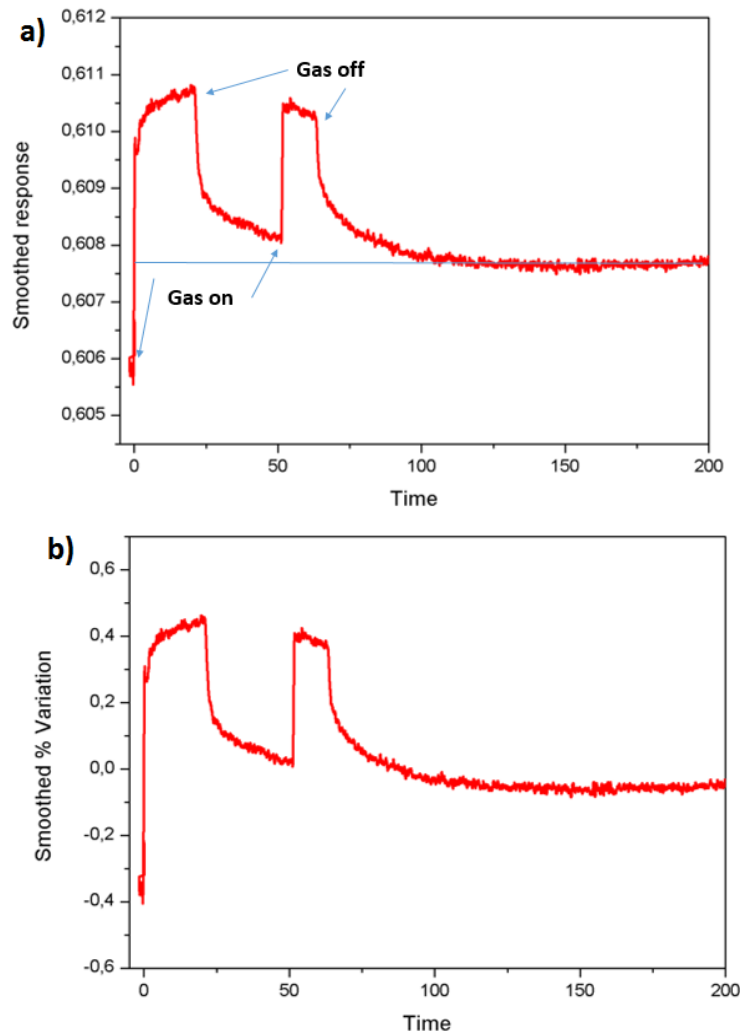


Fig. 23. Fiber #2: butane (a) response and (b) % variation.

Titanium dioxide with a thickness of 100 nm. Fibers #1 and #2 are coated with titanium oxide sputtered starting from a 99.6% purity target; Figs. 24a and 24b show the signal and the % variation of fiber #1, respectively, in the presence of butane; Figs. 24c and 24d characterize fiber #2. It is of interest that both fibers show a good sensibility toward butane with fast adsorption and desorption kinetics. The higher % variation values of the fibers (~2%) compared with the values of the TiO₂-coated fiber in set 2 (~0.4%) can be attributed to the lower film thickness.

Instead, a 99.9% purity target was used to coat fibers #3 and #4; the signal and % variation of the former are shown in Fig. 25. Fiber #4 exhibits a low baseline value apparently owing to a bad fiber cut before TiO₂ deposition, as shown in Fig. 26.

This fiber subset was prepared to study the effect of the target purity on the titanium oxide sensing behavior: comparison of Figs. 24 and 25 shows that there is no remarkable difference in terms of % variation between the fibers obtained with different target purities. It is not yet clear why fibers #1 and #2 show a negative shift (decrease in the signal in the presence of butane), while fiber #3 shows a positive shift.

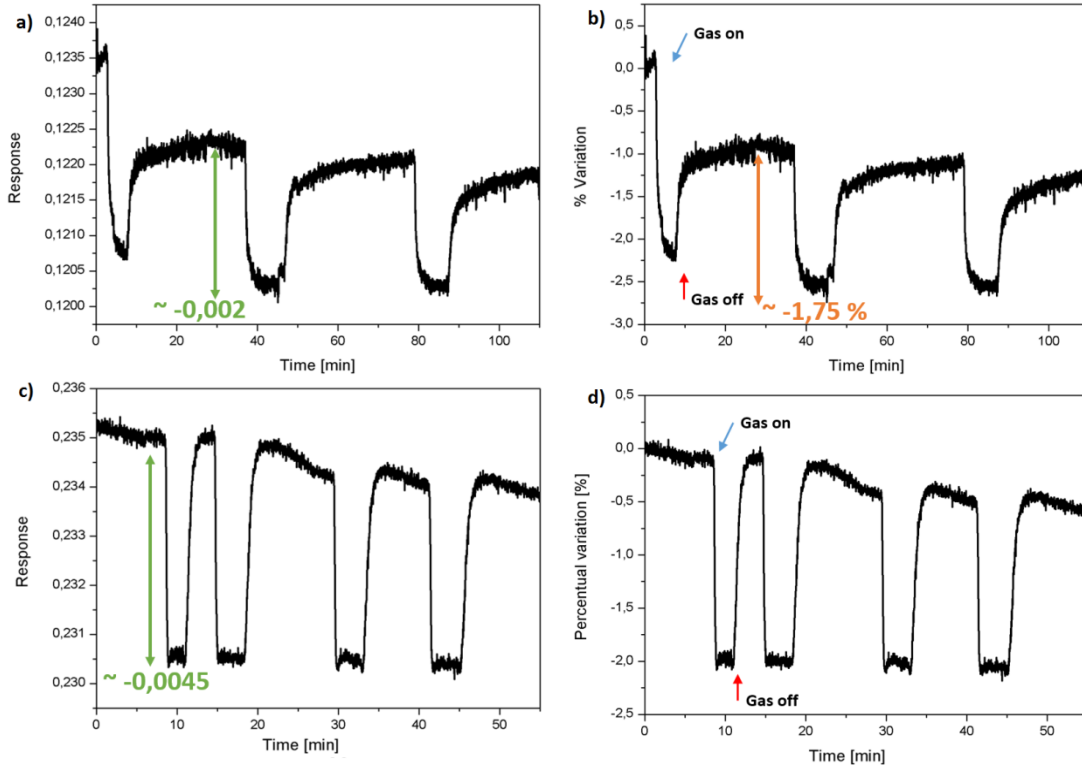


Fig. 24. Fibers #1 and # 2: butane sensing behavior.

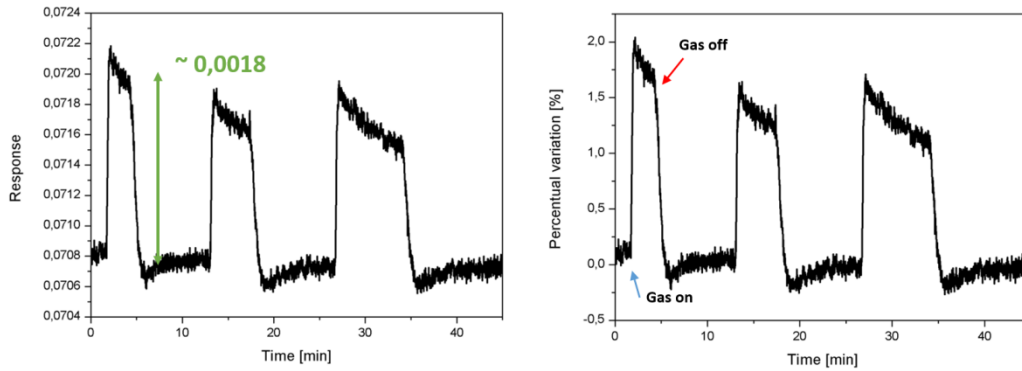


Fig. 25. Fiber #3: butane sensing behavior.

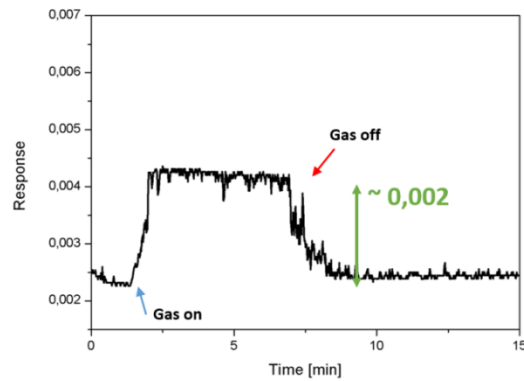


Fig. 26. Fiber #4: butane sensing behavior.

Optical fibers coated with SnO₂. Analogously to the ZnO-coated fiber, fiber #3 with SnO₂ also shows a very low signal/noise ratio, as evident from Fig. 27; moreover, there is a drift of the signal regardless of the presence of butane.

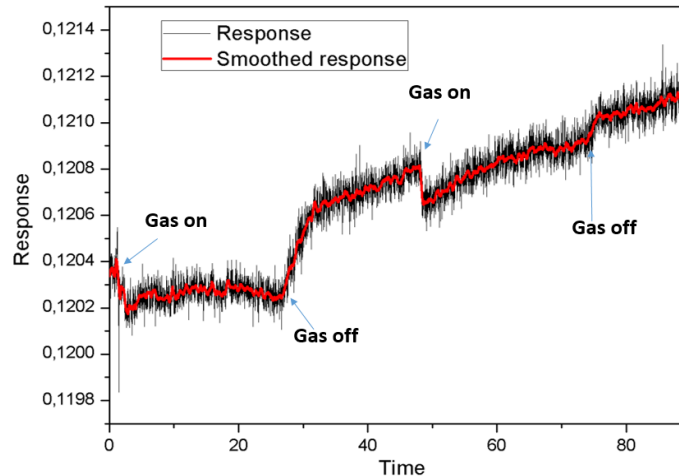


Fig. 27. Fiber #3: butane sensing behavior.

4. Conclusions

The studies have revealed that the ZnO and TiO₂ materials are promising candidates for the fabrication of real-life optical LPG sensors. Although TiO₂ has a higher sensitivity value, the two materials exhibit similar signal variation, which can be even more characteristic of this type of sensors than that of electrical metal oxide sensors. An important finding is the necessity of careful preparation of the fibers and a thermal treatment of the working oxide films. It has been shown that the sensitivity increases after the annealing of nanocrystalline ZnO. The sensitivity increases with increasing layer thickness. The prepared sensors attain a sensitivity of 2.77% for ZnO and 24.4% for TiO₂.

References

- [1] Shi-Kai Tzeng, Min-Hsiung Hon, and Ing-Chi Leu, *J. Electrochem. Soc.* 159 (4), H440 (2012).
- [2] Sutichai Chaisitsak, *Sensors* 11, 7127 (2011).
- [3] Suparna Banerjee, Ali Bumajdad, and P Sujatha Devil, *Nanotechnology* 22, 275506 (2011).
- [4] M. V. Vaishampayan, R.G. Deshmukh, and I.S. Mulla, *Sens. Actuators, B* 131, 665 (2008).
- [5] O. Lupan, V. M. Guérin, L. Ghimpu, I.M. Tiginyanu, and T. Pauporté, *Chem. Phys. Lett.* 22, 125 (2012).
- [6] L. Ghimpu, I. M. Tiginyanu, V. Ursaki, O. Lupan, L. Chow, Y. Rudzevich, and Y. Lin, *CAS-2012 Proc.*, October 15–17, 2012, Sinaia, Romania, vol. II, p. 237.
- [7] S. Majumder, S. Hussain, S.N. Das, R.B. Bhar, and A.K. Pal, *Vacuum* 82, 760 (2008).
- [8] A.R. Babar, S.S. Shinde, A.V. Moholkar, C.H. Bhosale, J.H. Kim, and K.Y. Rajpure, *J. Alloys Compd.* 509, 3108 (2011).
- [9] B. Thomas, S. Benoy, and K.K. Radha, *Sens. Actuators, B* 133, 404 (2008).

- [10] G. Korotcenkov, *Mater. Sci. Eng. R Rep.* 61, 1 (2008).
- [11] A. Gurlo, M. Ivanovskaya, N. Bârsan, M. Schweizer-Berberich, U. Weimar, W. Göpel, and A. Diéguez, *Sens. Actuators, B* 44, 327 (1997).
- [12] G. Ganguly, D.E. Carlson, S.S. Hegedus, D. Ryan, R.G. Gordon, D. Pang, and R.C. Reedy, *Appl. Phys. Lett.* 85, 479 (2004).
- [13] C.H. Han, S.D. Han, I. Singh, and T. Toupance, *Sens. Actuators, B* 109, 264 (2005).
- [14] C.H. Han, S.D. Han, and S.P. Khatkar, *Sensors* 6, 492 (2006).
- [15] C.H. Han, D.U. Hong, J. Gwak, and S.D. Han, *Korean J. Chem. Eng.* 24, 927 (2007).
- [16] Z. U. Abideen, A. Katoch, J.-H. Kim, Y. J. Kwon, H. W. Kim, and S. S. Kim, *Sens. Actuators B* 221, 1490 (2015).
- [17] B. Renganathan and A.R. Ganesan, *Opt. Fiber Technol.* 20, 48 (2014).
- [18] T. van Tran, S. Turrell, M. Eddafi, B. Capoen, M. Bouazaoui, P. Roussel, S. Berneschi, G. Righini, M. Ferrari, S.N.B. Bhaktha, O. Cristini, and C. Kinowski, *J. Mol. Struct.* 976, 314 (2010).
- [19] T. L. Yeo, T. Sun, and K. T. V. Grattan, *Sens. Actuators A* 144 (2), 280 (2008).
- [20] B. Zhang, Y. Tian, J.X. Zhang, and W. Cai, *Physica B: Condens. Matter* 406, 1822 (2011).

DETECTION IN THE CONTACTS AT LOW TEMPERATURES: EFFECT OF THE FREE ELECTRON CONCENTRATION ON THE DETECTING PARAMETERS

Ia. Kerner

*Institute of Electronic Engineering and Nanotechnologies “D. Gitsu”
Academy of Sciences of Moldova
Academiei str. 3/3, Chisinau, MD-2028 Republic of Moldova
E-mail: iacov@nano.asm.md*

(Received June 12, 2018)

Abstract

Diode detectors (DDs) are widely used in electronic information and communication systems. In this paper, the numerical modeling of the electrical potential distribution and current passing in the contacts of a normal metal or a superconductor with a bismuth–antimony (Bi–Sb) semiconductor alloy has been conducted. The possibilities of designing DDs based on these contacts to operate at a temperature (T) of liquid helium of 4.2 K and 1 K have been explored. The dependences of current responsivity (CR), voltage responsivity (VR) and noise equivalent power (NEP) on the free electron concentration have been analyzed. The physical causes of these dependences have been examined. The effect the signal frequency (f) on the detecting parameters has been shown. The obtained results have been compared with the literature data. Comparison with the currently available literature data has shown that proposed DDs can be 1–2 orders better. The physical reasons for these advantages have been discussed. It has been shown that the unique properties of Bi–Sb alloys, particularly the $\text{Bi}_{0.88}\text{Sb}_{0.12}$ alloy, make these alloys promising materials for cryoelectronics.

1. Introduction

Diode detectors (DDs) play an important role in radio technique and electronics. The use of high frequencies (above 1 GHz) has stimulated a thorough study of Schottky-barrier diodes. These diodes are based on quick-acting metal–semiconductor contacts [1].

A further improvement of the parameters of diodes was achieved due to a decrease in the operating temperature [2]. This direction is referred to as cryoelectronics [3]; it provides an increase in the nonlinearity of the current–voltage dependences and current responsivity (CR). The thermal noise power decreases too. For example, DDs based on Pb–pGaAs contacts have been developed [4, 5]. At a signal frequency of $f = 9$ GHz and $T = 4.2$ K, these diodes had $\text{CR} \approx 500$ A/W and a noise equivalent power (NEP) of 5×10^{-15} W/ $\sqrt{\text{Hz}}$.

In addition, deep cooling allows using the materials with a narrow energy gap and a high electron mobility, such as Bi–Sb solid solutions [3, 6].

After the discovery of the high temperature superconductors (HTSCs), the possibilities of using HTSC in cryoelectronics were studied. At the liquid nitrogen temperature of $T = 77$ K and a signal frequency of $f = 37.5$ GHz, the respective structures exhibited a voltage responsivity (VR) of 3000 V/W [7]. Further studies [8] provided the design of structures with $\text{VR} = 5000$ V/W and $\text{NEP} = 2 \times 10^{-12}$ W/ $\sqrt{\text{Hz}}$ at a signal frequency of $f = 31$ GHz and a temperature of $T = 77$ K.

According to our publication [9], the DDs based on HTSC–InSb contacts can have $CR \approx 40$ A/W, $VR \approx 10^6$ V/W, and $NEP \approx 8 \times 10^{-15}$ W/ \sqrt{Hz} at $T = 77.4$ K and $f = 10$ GHz. At the same temperature and $f = 30$ GHz, these DDs can have $CR \approx 15$ A/W, $VR \approx 3.5 \times 10^5$ V/W, and $NEP \approx 2 \times 10^{-14}$ W/ \sqrt{Hz} at a contact area of $100 \mu\text{m}^2$; however, a reduction in the contact area makes it possible to improve these parameters.

On the other hand, the semiconductor in HTSC–semiconductor contacts frequently undergoes oxidation because oxygen is an integral part of a HTSC. In addition, cooling to the liquid nitrogen temperature of 77.4 K can be insufficient to obtain good DD parameters. In this situation, taking into account the rapid development of cryogenics, a study of DDs based on conventional superconductor–semiconductor contacts seems to be an urgent problem. Typically, DDs operate at liquid helium temperatures ($T \leq 4.2$ K) [10, 11]. In this study, DDs based on the contacts of a superconductor (or a normal metal) with a Bi–Sb semiconductor solid solution are discussed.

2. Results and Discussion

Contacts of the $\text{Bi}_{0.88}\text{Sb}_{0.12}$ semiconductor solid solution with a normal metal or a superconductor were considered (for a contact area of $100 \mu\text{m}^2$). Aluminum at $T \geq 1.2$ K and silver or gold at lower temperatures can be used as the normal metal. Niobium or niobium nitride (NbN) can be chosen as superconductors at liquid helium temperatures. Properties of the materials were taken from [12–14]. Results of calculations for contacts with a normal metal are shown in Figs. 1–3. In these figures, a logarithmic scale for both axes is used. An exponential form is commonly used for numbers of axes.

Figure 1 shows the calculated dependence of CR on the free electron concentration in $\text{Bi}_{0.88}\text{Sb}_{0.12}$.

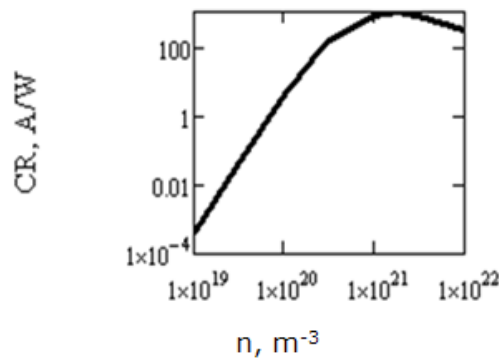


Fig. 1. Calculated dependence of CR on the free electron concentration in $\text{Bi}_{0.88}\text{Sb}_{0.12}$ at a signal frequency of $f = 1$ GHz and $T = 4.2$ K.

Initially, the CR increases with an increase in the free electron concentration because the ohmic volume resistance drops faster than the contact capacity resistance. This effect increases the signal voltage applied to the contact and the signal power absorbed in the contact and transformed in the rectified current.

However, an increase in the free electron concentration above 10^{21} m^{-3} it leads to an

increase in the barrier permeability, because the barrier width decreases. This fact reduces the nonlinearity of the current voltage, and the CR decreases.

Figure 2 shows the calculated dependence of VR on the free electron concentration in $\text{Bi}_{0.88}\text{Sb}_{0.12}$. In our case, inequality $r \ll R_c$ is fulfilled (r is the ohmic volume resistance; R_c is the contact differential resistance). In this situation [1], we can assume that $\text{VR} \approx \text{CR} \times R_c$.

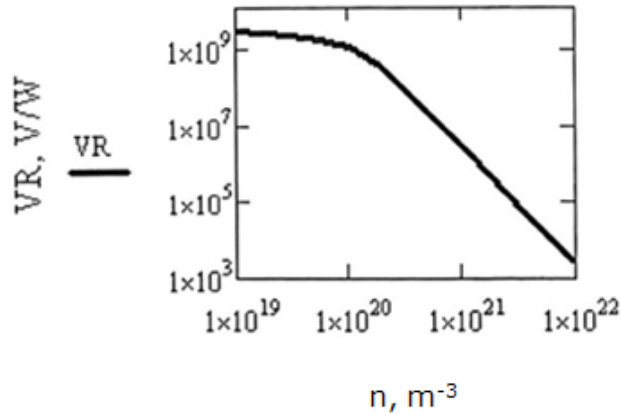


Fig. 2. Calculated dependence of VR on the free electron concentration. Other data are similar to those in Fig. 1.

As the free electron concentration increases, the barrier permeability increases (see above) and the contact differential resistance decreases. The VR also decreases. If the free electron concentration is less than 10^{21} m^{-3} , the enlargement of the CR limits this effect.

However, if the free electron concentration is more than 10^{21} m^{-3} , the CR decreases and the VR rapidly decreases.

Figure 3 shows the calculated dependence of NEP on the free electron concentration in $\text{Bi}_{0.88}\text{Sb}_{0.12}$. This value increases with an increase in the free electron concentration, because the noise current sufficiently increases.

However, in a concentration range of 10^{20} to 10^{21} m^{-3} , this effect is diminished due to a rapid increase in the CR (see Fig. 1).

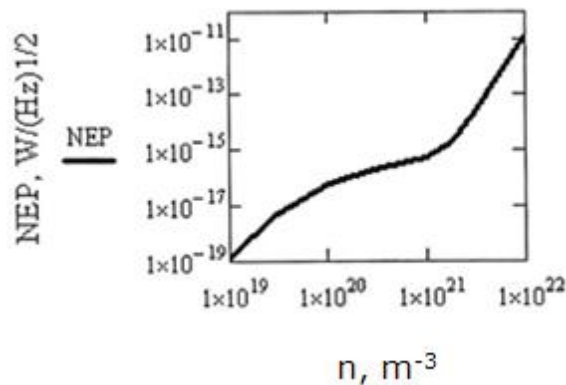


Fig. 3. Calculated dependence of NEP on the free electron concentration. Other data are similar to those in Fig. 1.

If the metal is replaced by a superconductor, the DD parameters are significantly improved [15]. The respective results are shown in Figs. 4 and 5.

The effect is particularly pronounced when the working temperature decrease from 4.2 to 1 K and the current passes due to the field emission regime [3]. In this regime, electrons near the Fermi level bring the main contribution to the contact current. However, at cryogenic temperatures, the properties of these electrons hardly depend on temperature; therefore, their current also hardly depends on temperature. In this case, in contacts with normal metals, the nonlinearity of the current–voltage characteristic (CVC) and the CR hardly depend on temperature [1, 3].

However, in contacts with superconductors, due to unique tunneling properties of superconductor [3], the CVC nonlinearity increases and the DD parameters are especially improved (compare curves 1 and 2 in Figs. 4, 5). This effect increases at a larger energy gap of the superconductor (see curves 2, 3 in Figs. 4, 5). This fact points out the necessity to select a superconductor with a wide energy gap (for example, NbN).

This effect is particularly pronounced in Fig. 6, which shows the initial portions of the CVCs for the NbN–Bi_{0.88}Sb_{0.12} contact. The CVCs for the normal metal–Bi_{0.88}Sb_{0.12} contact nearly coincide with curve 1 in Fig. 6, and they are not shown.

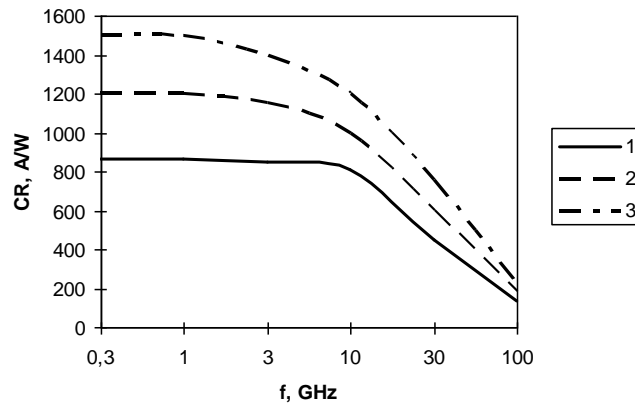


Fig. 4. Calculated dependence of CR on the signal frequency in contacts with Bi_{0.88}Sb_{0.12}. Curves 1, 2, and 3 correspond to the contacts with a normal metal, niobium, and niobium nitride, respectively. $T = 4.2$ K.

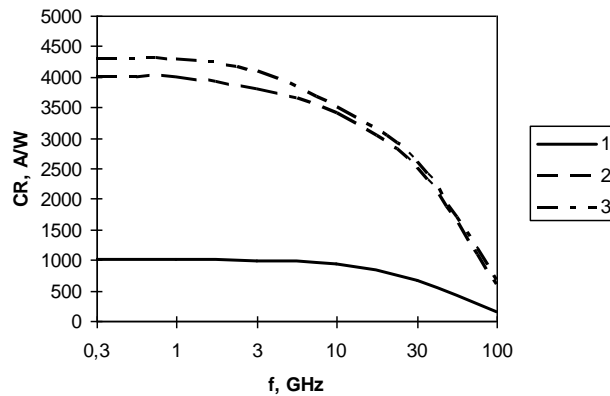


Fig. 5. Calculated dependence of CR on the signal frequency. The legend inscriptions are similar to those in Fig. 4. $T = 1$ K.

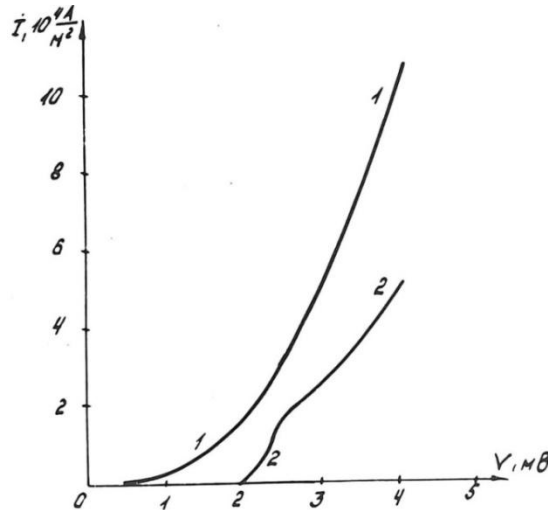


Fig. 6. Initial portions of the CVCs for the NbN–Bi_{0.88}Sb_{0.12} contact; $T = (1)$ 4.2 and (2) 1 K. I is the current density (in A/m²), V is the applied voltage (in mV).

Figures 4 and 5 show that the CR decreases and the NEP increases at frequencies above 3 GHz. At these frequencies, the negative role of the barrier capacity is revealed; it begins to shunt the nonlinear contact resistance. The current redistribution occurs; it leads to a decrease in the rectified current, and the DD parameters become worse.

Taking into account results of [4, 5, 7–9], we can conclude that contacts with Bi–Sb provide a significant improvement in DD parameters. They are much more effective than HTSC–superconductor contacts [7–9, 13]. In addition, they are better than contacts with GaAs [4, 5] operating at the liquid helium temperature.

The main advantages of Bi–Sb are as follows:

(i) Small barrier heights due to a narrow energy gap. This fact provides a considerable nonlinearity of the CVC and a high CR.

(ii) Extremely high electron mobility, which leads to a decrease in the ohmic resistance and improves the frequency properties.

(iii) At the same contact area and barrier permeability, the contact capacity in structures with Bi_{0.88}Sb_{0.12} is 4 times less than that for contacts with GaAs, which is one of the best materials of cryoelectronics. This fact is attributed to small barrier heights and small effective masses of electrons; these features also improve the frequency properties.

These unique properties of Bi–Sb alloys, particularly of the Bi_{0.88}Sb_{0.12} alloy, make these alloys promising materials for cryoelectronics.

3. Conclusions

The obtained results show that parameters of DDs based on contacts with Bi–Sb can be sufficiently improved due to selection of an optimum doping level and especially due to the use of contacts with superconductors. The physical reasons for these effects are discussed.

Analysis of our results [9–1, 15] shows that the proposed DDs (based on contacts with

Bi–Sb) may have a 2 times higher CR and a 50 times lower NEP than the the respective parameters of the currently available DDs (at the same temperature and signal frequency). In addition, they exhibit an extremely high VR. Their parameters can be a few orders of magnitude better than those of DDs operating at the liquid nitrogen temperature. This fact suggests that the preparation of contacts with Bi–Sb is promising.

References

- [1] V.I. Strikha, E.V. Buzaneva, and I.A. Radzievskii, *Poluprovodnikovye pribory s bar'erom Shottki. Fizika, tekhnologiya, primenenie*, Sov. Radio, Moscow, 248 pages, 1974.
- [2] J.H. Hinken, *Superconductor Electronics. Fundamentals and Microwave Applications*, Springer-Verlag, Berlin, Heidelberg, New York, London, 158 pages, 1989.
- [3] V.N. Alfeev, *Sverkhprovodniki, poluprovodniki i paraelektriki v krioelektronike*, Sov. Radio, Moscow, 408 pages, 1979.
- [4] M. Mc Call, M.F. Millea, and A.H. Silver, *Appl. Phys. Lett.* 23 (5), 263 (1973).
- [5] M. Mc Call, M.F. Millea, A.H. Silver, et al., *IEEE Trans. Magn.* 13 (1), 221 (1977).
- [6] V.G. Alekseeva, T.M. Lifshits, E.G. Chirkova, A.Ia. Shul'man, *Radiotekh. Elektron.* 23 (9), 1926 (1978).
- [7] V.A. Kulikov, L.V. Matveets, A.Iu. Serebryakov, et al., *Pis'ma Zh. Tekh. Fiz.* 15 (20), 74 (1989).
- [8] L.S. Kuz'min, V. N. Okhrimenko, E. S. Soldatov, and A. N. Tavkhelidze, *Sverkhprovodimost'* 3, 11, 2650 (1990).
- [9] Ia.I. Kerner, in: *Proc. 3rd Int. Conf. on Nanotechnologies and Biomedical Engineering ICNBME-2015, September 23–26, 2015, Chisinau, Republic of Moldova, Part I*, vol. 55, pp. 40–42.
- [10] Ia.I. Kerner, in: *Proc. 8th Int. Conf. on Microelectronics and Computer Science, October 22–25, 2014, Chisinau, Republic of Moldova; Technica-U.T.M., Chisinau*, 68, 2014.
- [11] Ia.I. Kerner, *Mold. J. Phys. Sci.* 13 (3–4), 222 (2014).
- [12] E. H. Rhoderick, *Metal–Semiconductor Contacts*, Clarendon Press, Oxford, 208 pages, 1978.
- [13] D.V. Gitsu, I.M. Holban, V.G. Kantser, and F.M. Munteanu, *Yavleniya perenosa v vismute i ego splavakh*, Stiinta, Kishinev, 266 pages, 1983.
- [14] *Tablitsy fizicheskikh velichin. Spravochnik*, Ed. by acad. I.K. Kikoin, Atomizdat, Moscow, 1006 pages, 1976.
- [15] Ia.I. Kerner, in: *Proc. 9th Int. Conf. on Microelectronics and Computer Science & 6th Conf. "Physicists of Moldova"*, October 19–21, 2017, Chisinau, Moldova, Ed. by I. Tighineanu and I. Balmus, Chisinau, 2017, pp. 122–125.

TRANSMISSION OF MEASURING SIGNALS BY AN INVARIANT PROPERTY OF COMMUNICATION LINES WITH LOSSES

A. Penin and A. Sidorenko

*D. Ghitu Institute of Electronic Engineering and Nanotechnologies,
Academiei str.3/3, Chisinau, MD-2028 Republic of Moldova
E-mails: aapenin@mail.ru, anatoli.sidorenko@kit.edu*

(Received November 20, 2018)

Abstract

An invariant relationship between sets of load conductivity values and the respective values of the input currents of three wire communication lines is shown. This relationship does not depend on parameters of the lines and the accuracy of measuring devices. It allows transmitting signals of different physical sensors in the analog form for monitoring technical or natural objects.

Keywords: communication line, resistive sensor, projective transformation, cross ratio, projective coordinates

1. Introduction

Different sensors of physical values are used for monitoring technical or natural objects. For these—typically remote—devices, it is necessary to provide the transmission of measuring signals [1], for example, by multi-wire lines [2]. At present time, methods for transmitting discrete electrical signals in the binary code are used. These methods are known as the RS-485 and MicroLAN interfaces. Low noise immunity is a disadvantage of the known methods. Therefore, researches and elaborations of systems for transmitting discrete electrical signals in the analog form with an improved noise immunity are important [3–5]. However, two dedicated communication lines are necessary to transfer two signals. The point is that longitudinal and lateral resistive losses of actual lines do not allow using the common wire so as to apply more economical three-wire lines.

The theoretical researches show that an invariant relationship takes place between sets of load conductivity values and the respective values of the input currents of this line with losses [6–8]. The cross ratio of four points, known in projective geometry, is this invariant relationship [9]. Therefore, the value of cross ratio (ratio of two proportions) does not depend on parameters of the line and the accuracy of the measuring devices. These invariants are used for the transmission or, more precisely, restoration of measuring signals over three wire lines.

In the present paper, the obtained results are developed for the practical implementation of these transmission systems.

2. Foundation of the Transmission of Signals over a Line

We consider a four-port circuit in Fig. 1. Let us give necessary relationships between the input currents and load conductivities. So, we have

$$V_1 = I_1 / Y_{L1}, \quad V_2 = I_2 / Y_{L2}.$$

The family of straight lines $(I_1, I_2, Y_{L1}) = 0$, $(I_1, I_2, Y_{L2}) = 0$ at change of Y_{L1}, Y_{L2} is represented by two bunches of straight lines in the system of coordinates (I_1, I_2) in Fig. 2.

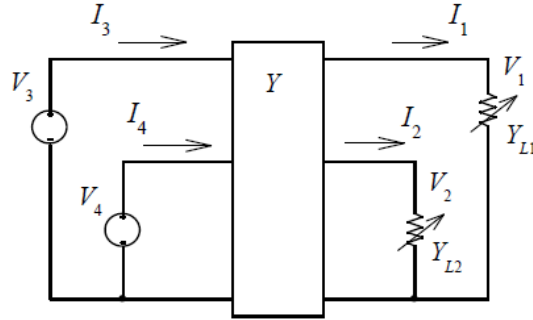


Fig. 1. Four port with variable load conductivities Y_{L1}, Y_{L2} .

Next, we use the idea of projective coordinates of a running regime point. Let the initial or running regime correspond to point M^1 , which is set by the values of conductivities Y_{L1}^1, Y_{L2}^1 and currents I_1^1, I_2^1 .

In addition, this point is defined by projective non-uniform coordinates m_1^1, m_2^1 and homogeneous coordinates $\xi_1^1, \xi_2^1, \xi_3^1$, which are set by the reference or coordinate triangle G_1, G_2, SC .

The nonuniform projective coordinate, as the cross ratio of four points, has the form

$$m_1^1 = (Y_{L1}^{OC} \ Y_{L1}^1 \ Y_{L1}^{SC} \ Y_{L1}^{G1}) = \frac{Y_{L1}^1 - 0}{Y_{L1}^1 - Y_{L1}^{G1}} \div \frac{\infty - 0}{\infty - Y_{L1}^{G1}} = \frac{Y_{L1}^1}{Y_{L1}^1 - Y_{L1}^{G1}}, \quad m_2^1 = \frac{Y_{L2}^1}{Y_{L2}^1 - Y_{L2}^{G2}}. \quad (1)$$

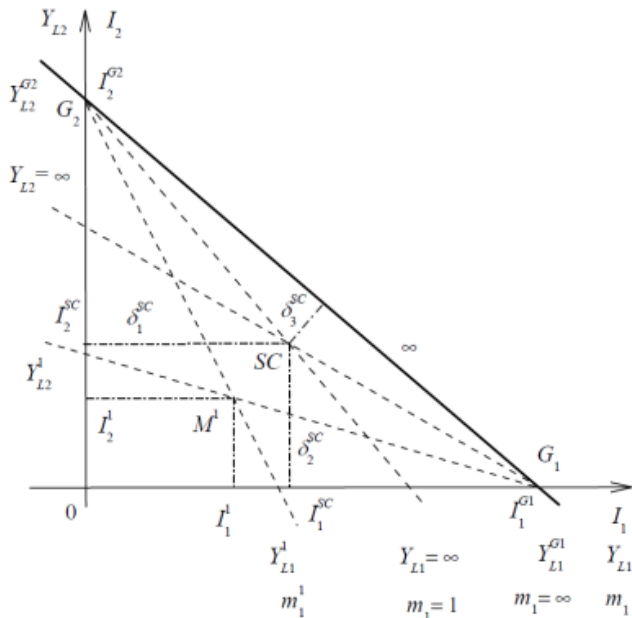


Fig. 2. Two bunches of load straight lines with the parameters Y_{L1}, Y_{L2} .

In turn, the homogeneous projective coordinates ξ_1, ξ_2, ξ_3 set the nonuniform coordinates by

$$m_1 = \frac{\xi_1}{\xi_3}, \quad m_2 = \frac{\xi_2}{\xi_3}. \quad (2)$$

The homogeneous coordinates are defined as the ratio of distances $\delta_1^1, \delta_2^1, \delta_3^1$ of point M^1 and distances $\delta_1^{SC}, \delta_2^{SC}, \delta_3^{SC}$ of point SC to the sides of the coordinate triangle $G_1 0 G_2$:

$$\xi_1^1 = \frac{\delta_1^1}{\delta_1^{SC}} = \frac{I_1^1}{I_1^{SC}}, \quad \xi_2^1 = \frac{\delta_2^1}{\delta_2^{SC}} = \frac{I_2^1}{I_2^{SC}}, \quad \xi_3^1 = \frac{\delta_3^1}{\delta_3^{SC}} = \frac{I_3^1}{I_3^{SC}} \quad \rho \xi_3^1 = \frac{\delta_3^1}{\delta_3^{SC}}. \quad (3)$$

Let us consider the input currents (I_3, I_4) of our four-port. We may superpose the system of coordinates $(I_3 0 I_4)$ with the system of coordinates $(I_1 0 I_2)$ in Fig. 3. Then, any point M^1 with coordinates (I_1, I_2) corresponds to a point \bar{M}^1 with coordinates (I_3, I_4) .

In terms of geometry, a projective transformation that transfers points of the (I_1, I_2) plane into points of the (I_3, I_4) plane takes place. Therefore, the reference triangle $G_1 0 G_2$, the SC point, and the running regime point M^1 correspond to triangle $\bar{G}_1 \bar{0} \bar{G}_2$, point \bar{SC} , and point \bar{M}^1 , as shown by arrows.

Next, the axes of currents I_1, I_2 correspond to axes \bar{I}_1, \bar{I}_2 . In addition, two bunches of the straight lines $(I_1, I_2, Y_{L1})=0$, $(I_1, I_2, Y_{L2})=0$ correspond to two bunches of the lines $(I_3, I_4, Y_{L1})=0$, $(I_3, I_4, Y_{L2})=0$ with centers at points \bar{G}_2, \bar{G}_1 . Thus, point \bar{M}^1 is set by other currents I_3^1, I_4^1 . In addition, this point is defined by projective nonuniform and homogeneous coordinates, which are set by the reference triangle $\bar{G}_1 \bar{0} \bar{G}_2$ and a unit point \bar{SC} .

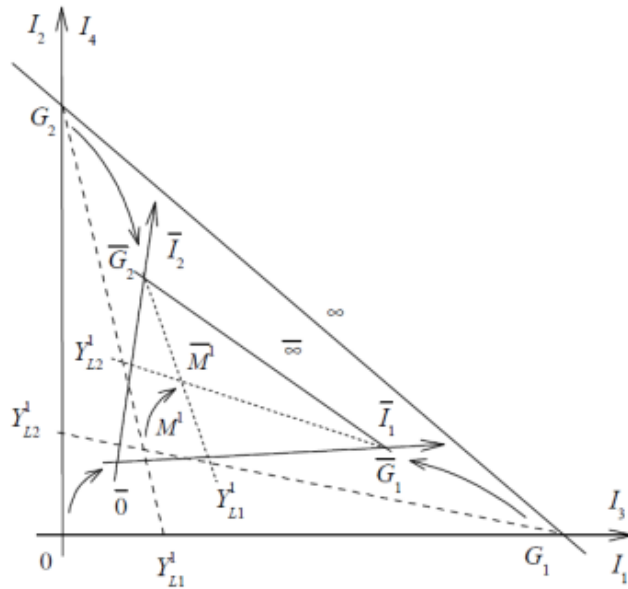


Fig. 3. Projective transformation of the (I_1, I_2) plane onto the (I_3, I_4) plane.

The property of projective transformations shows that the point \bar{M}^1 coordinates are equal to the point M^1 coordinates, as these points M^1, \bar{M}^1 are set by the same loads Y_{L1}^1, Y_{L2}^1 . Therefore, this property gives required invariant relations between the input and output currents. To find the point \bar{M}^1 projective coordinates, it is necessary to use the equations of sides of the reference triangle. Finally, we obtain the nonuniform coordinates by the input currents:

$$m_1 = \frac{C_{11}I_3 + C_{12}I_4 + 1}{C_{31}I_3 + C_{32}I_4 - 1}, \quad m_2 = \frac{C_{21}I_3 + C_{22}I_4 + 1}{C_{31}I_3 + C_{32}I_4 - 1}. \quad (4)$$

Using running values of input currents, we find or, more precisely, restore the values of nonuniform coordinates (9). Then, the values of given load conductivities are calculated according to the inverse expressions $Y_{L1}(m_1), Y_{L2}(m_2)$ to (1).

This formulated algorithm is of practical interest for the transfer of two sensing signals via a three-wire line; it makes it possible to separate (or restore) two signals by the input currents (five pairs of the currents) of the line.

In actual practice, the characteristic values of the input and output currents (as the vertexes of the coordinate triangles and unit points) are precalculated by testing the line. To do so, in a short time slot, the five pairs of load conductivity sets (test and information values) are transmitted. There are test conductivities $Y_{L1}^{OC}, Y_{L1}^{SC}, Y_{L1}^{G1}, Y_{L2}^{OC}, Y_{L2}^{SC}, Y_{L2}^{G2}$ and information conductivities Y_{L1}^1, Y_{L2}^1 . Usually, the test scale conductivities $Y_{L1}^{G1} < 0, Y_{L2}^{G2} < 0$. Therefore, the respective output currents submit to terms $I_1^{G1} > I_1^{SC}, I_2^{G2} > I_2^{SC}$. These large test values complicate the practical implementation. Therefore, we will consider the easily testable transmission system [10] in Fig. 4.

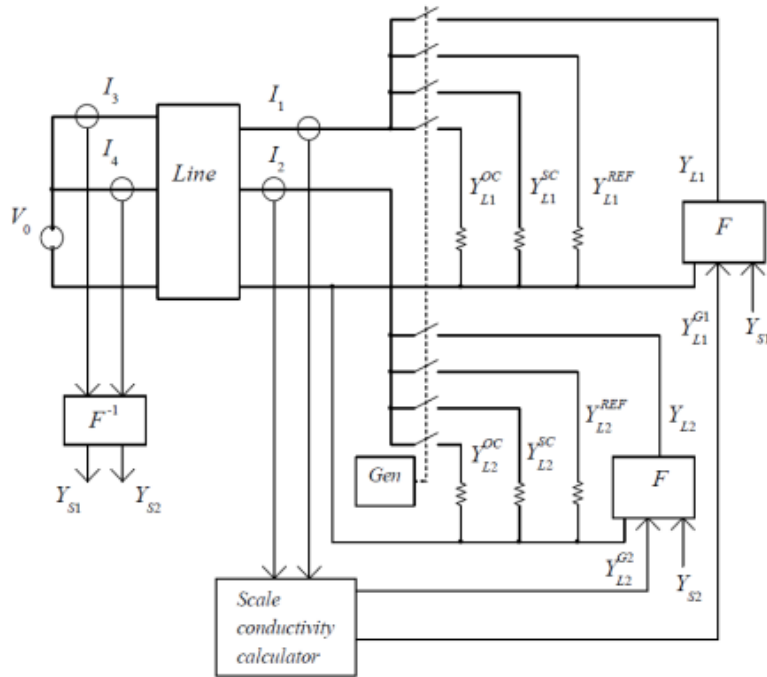


Fig. 4. System of transmission of two sensor signals.

3. Easily Testable Transmission System

At first, in a short time slot, five pairs of test load conductivity sets are transmitted. There are test conductivities $Y_{L1}^{OC}, Y_{L1}^{SC}, Y_{L1}^{REF}, Y_{L2}^{OC}, Y_{L2}^{SC}, Y_{L2}^{REF}$, as shown in Table 1.

Table 1. Correspondence between the test load conductivities and the output and input currents

| Set | Load conductivities | | Output currents | | Input currents | |
|-----|------------------------|------------------------|-------------------|-------------------|----------------|---------------|
| 1 | $Y_{L1}^{OC} = 0$ | $Y_{L2}^{OC} = 0$ | $I_1^{OC} = 0$ | $I_2^{OC} = 0$ | I_3^{OC} | I_4^{OC} |
| 2 | $Y_{L1}^{OC} = 0$ | $Y_{L2}^{SC} = \infty$ | $I_1^{OC,SC} = 0$ | $I_2^{OC,SC}$ | $I_3^{OC,SC}$ | $I_4^{OC,SC}$ |
| 3 | $Y_{L1}^{SC} = \infty$ | $Y_{L2}^{OC} = 0$ | $I_1^{SC,OC}$ | $I_2^{SC,OC} = 0$ | $I_3^{SC,OC}$ | $I_4^{SC,OC}$ |
| 4 | $Y_{L1}^{SC} = \infty$ | $Y_{L2}^{SC} = \infty$ | I_1^{SC} | I_2^{SC} | I_3^{SC} | I_4^{SC} |
| 5 | Y_{L1}^{REF} | Y_{L2}^{REF} | I_1^{REF} | I_2^{REF} | - | - |

For clarity, we give the geometrical interpretation of the obtained sets similarly to Fig. 2. The family of straight lines $(I_1, I_2, Y_{L1})=0$, $(I_1, I_2, Y_{L2})=0$ for the test load conductivities is represented by the two bunches of straight lines in the system of coordinates (I_1, I_2) in Fig. 5.

Let us consider the following points. Points $I_1^{SC,OC}$, $I_2^{OC,SC}$ are situated accordingly on axes I_1 and I_2 . Coordinates I_1^{SC}, I_2^{SC} and I_1^{REF}, I_2^{REF} determinate points SC, REF .

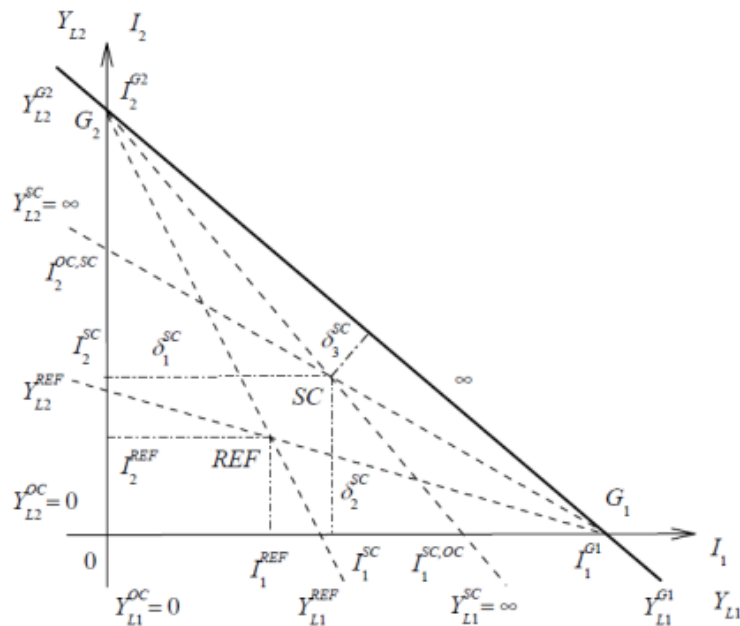


Fig. 5. Two bunches of load straight lines with the test parameters.

As noted above, currents I_1^{G1}, I_2^{G2} considerably exceed currents I_1^{SC}, I_2^{SC} . Then, we can determine scale conductivity Y_{L1}^{G1} corresponding to coordinate $(I_1^{G1}, 0)$ (as the intersection of the straight line passing through points $I_2^{OC,SC}, SC$ with axis I_1).

The straight line $(I_2^{OC,SC}, SC)$ equation is as follows:

$$\frac{I_2}{I_2^{OC,SC}} + \frac{(I_2^{OC,SC} - I_2^{SC}) \cdot I_1}{I_2^{OC,SC} I_1^{SC}} - 1 = 0.$$

For current $I_2 = 0$, point G_1 corresponds to the current

$$I_1^{G1} = \frac{I_2^{OC,SC} \cdot I_1^{SC}}{I_2^{OC,SC} - I_2^{SC}}. \quad (5)$$

Similarly, scale conductivity Y_{L2}^{G2} corresponds to coordinate $(I_1^{G1}, 0)$ or point G_2 . Then

$$I_2^{G2} = \frac{I_1^{SC,OC} \cdot I_2^{SC}}{I_1^{SC,OC} - I_1^{SC}}. \quad (6)$$

Let us introduce the homogeneous coordinate $\xi_1^{REF}, \xi_2^{REF}, \xi_3^{REF}$ of point REF :

$$\xi_1^{REF} = \frac{\delta_1^{REF}}{\delta_1^{SC}} = \frac{I_1^{REF}}{I_1^{SC}}, \quad \xi_2^{REF} = \frac{\delta_2^{REF}}{\delta_2^{SC}} = \frac{I_2^{REF}}{I_2^{SC}}, \quad \xi_3^{REF} = \frac{\delta_3^{REF}}{\delta_3^{SC}}. \quad (7)$$

We use the distances to the sides of triangle $G_1 O G_2$. In particular, for the equation of the straight line $G_1 G_2$

$$\frac{I_2}{I_2^{G2}} + \frac{I_1}{I_1^{G1}} - 1 = 0,$$

and the coordinate

$$\xi_3^{REF} = \frac{\delta_3^{REF}}{\delta_3^{SC}} = \frac{\frac{I_2^{REF}}{I_2^{G2}} + \frac{I_1^{REF}}{I_1^{G1}} - 1}{\frac{I_2^{SC}}{I_2^{G2}} + \frac{I_1^{SC}}{I_1^{G1}} - 1} \quad (8)$$

and further the nonuniform projective coordinates

$$m_1^{REF} = \frac{\xi_1^{REF}}{\xi_3^{REF}}, m_2^{REF} = \frac{\xi_2^{REF}}{\xi_3^{REF}}. \quad (9)$$

On the other hand,

$$m_1^{REF} = (Y_{L1}^{OC} Y_{L1}^{REF} Y_{L1}^{SC} Y_{L1}^{G1}) = \frac{Y_{L1}^{REF}}{Y_{L1}^{REF} - Y_{L1}^{G1}}, \quad m_2^{REF} = \frac{Y_{L2}^{REF}}{Y_{L2}^{REF} - Y_{L2}^{G2}}.$$

Finally, for the load current values and the known test conductivities, the scale conductivity calculator gives the required values

$$Y_{L1}^{G1} = Y_{L1}^{REF} \frac{m_1^{REF} - 1}{m_1^{REF}}, \quad Y_{L2}^{G2} = Y_{L2}^{REF} \frac{m_2^{REF} - 1}{m_2^{REF}}. \quad (10)$$

Next, let us use the geometrical interpretation of input currents I_3, I_4 in Fig. 4. We determine the coordinates (I_3^{G1}, I_4^{G1}) of point \bar{G}_1 (as the intersection of the straight line passing through points $I_4^{OC,SC}, \bar{SC}$ with axis \bar{I}_1).

The straight line $(I_4^{OC,SC}, \bar{SC})$ equation is as follows:

$$(I_3^{SC} - I_3^{OC,SC})I_4 + (I_4^{OC,SC} - I_4^{SC})I_3 + (I_4^{SC}I_3^{OC,SC} - I_3^{SC}I_4^{OC,SC}) = 0. \quad (11)$$

The straight line $\bar{0}, I_3^{SC,OC}$ or the axis \bar{I}_1 equation has the form

$$A_{01}I_4 + B_{01}I_3 + C_{01} = 0,$$

where

$$A_{01} = I_3^{SC,OC} - I_3^{OC}, \quad B_{01} = I_4^{OC} - I_4^{SC,OC}, \quad C_{01} = I_4^{SC,OC}I_3^{OC} - I_4^{OC}I_3^{SC,OC}. \quad (12)$$

Owing to these equations, we obtain coordinates (I_3^{G1}, I_4^{G1}) . Similarly, we determine coordinates (I_3^{G2}, I_4^{G2}) of point \bar{G}_2 .

The straight line $I_3^{SC,OC}, \bar{SC}$ equation is as follows:

$$(I_3^{SC} - I_3^{SC,OC})I_4 + (I_4^{SC,OC} - I_4^{SC})I_3 + (I_4^{SC}I_3^{SC,OC} - I_3^{SC}I_4^{SC,OC}) = 0. \quad (13)$$

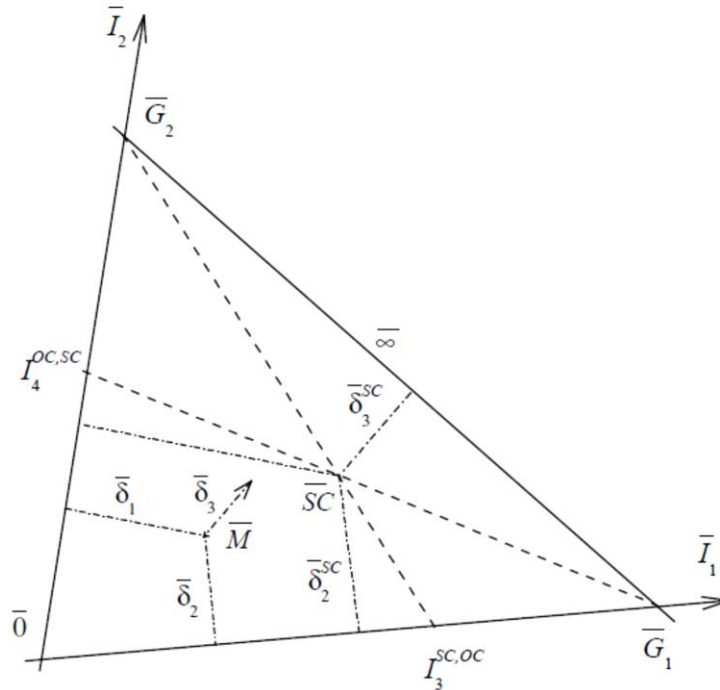


Fig. 4. Input characteristics of the line as coordinate system $\bar{G}_1 \bar{0} \bar{G}_2$.

The straight line $\bar{O}, I_4^{OC,SC}$ or axis \bar{I}_2 equation is as follows:

$$A_{02}I_4 + B_{02}I_3 + C_{02} = 0,$$

where

$$A_{02} = I_3^{OC,SC} - I_3^{OC}, B_{02} = I_4^{OC} - I_4^{OC,SC}, C_{02} = I_4^{OC,SC}I_3^{OC} - I_4^{OC}I_3^{OC,SC}. \quad (14)$$

Owing to these equations, we obtain coordinates (I_3^{G2}, I_4^{G2}) .

In addition, we give the equation of the straight line passing through points \bar{G}_2, \bar{G}_1

$$A_{12}I_4 + B_{12}I_3 + C_{12} = 0,$$

where

$$A_{12} = I_3^{G2} - I_3^{G1}, B_{12} = I_4^{G2} - I_4^{G1}, C_{12} = I_4^{G2}I_3^{G1} - I_4^{G1}I_3^{G2}. \quad (15)$$

The stage of preliminary testing and calculations is finished at this point.

Next, cross ratios (1) are accepted also as transmitted signals Y_{S1}, Y_{S2} . Then, using (5)–(10), the information conductivities are precomputed by units F :

$$Y_{L1} = \frac{Y_{L1}^{G1} \cdot Y_{S1}}{Y_{S1} - 1}, Y_{L2} = \frac{Y_{L2}^{G2} \cdot Y_{S2}}{Y_{S2} - 1}.$$

Using the input currents, we calculate homogeneous projective coordinates ξ_1, ξ_2, ξ_3 . In the given case, the homogeneous coordinates are defined as the ratio of distances $\bar{\delta}_1, \bar{\delta}_2, \bar{\delta}_3$ of point \bar{M} and distances $\bar{\delta}_1^{SC}, \bar{\delta}_2^{SC}, \bar{\delta}_3^{SC}$ of point \bar{SC} to the sides of the coordinate triangle $\bar{G}_1 \bar{O} \bar{G}_2$ by (11)–(15):

$$\xi_1 = \frac{\bar{\delta}_1}{\bar{\delta}_1^{SC}} = \frac{A_{02}I_4 + B_{02}I_3 + C_{02}}{A_{02}I_4^{SC} + B_{02}I_3^{SC} + C_{02}}, \quad \xi_2 = \frac{\bar{\delta}_2}{\bar{\delta}_2^{SC}} = \frac{A_{01}I_4 + B_{01}I_3 + C_{01}}{A_{01}I_4^{SC} + B_{01}I_3^{SC} + C_{01}}, \quad (16)$$

$$\xi_3 = \frac{\bar{\delta}_3}{\bar{\delta}_3^{SC}} = \frac{A_{12}I_4 + B_{12}I_3 + C_{12}}{A_{12}I_4^{SC} + B_{12}I_3^{SC} + C_{12}}.$$

Therefore, transmitted signals Y_{S1}, Y_{S2} by (16) are as follows:

$$m_1 = Y_{S1} = \frac{\xi_1}{\xi_3}, m_2 = Y_{S2} = \frac{\xi_2}{\xi_3}.$$

4. Conclusions

An invariant relationship between regime parameters at the input and output of a communication line takes place. The proposed selection of line parameters makes it possible to introduce projective coordinates for the easily testable transmission system. Input projective coordinates allow finding load conductivities only by the measured input currents without running determination of the transmission parameters of this line. It allows transmitting signals

over a communication line. The obtained results can be a basis for carrying out applied researches and developments; in particular, results can be extended to AC lines.

Acknowledgments. The authors are grateful to acad. V. Postolati and Prof. D. Maevski for useful discussion of results and to STCU#6329 and “SPINTECH–TWINNING” projects for financial support.

References

- [1] K. Walker, M. Ramplin, US Patent 6 459 363 B1 (2002).
- [2] A. Aldereguia, G. Richter, and J. Williams, US Patent 7 502 991 B2 (2009).
- [3] V. Ovchinnikov, US Patent 8 446 977 B2 (2013).
- [4] V. Ovchinnikov, RF Patent 2 250 566 (2005).
- [5] V. Ovchinnikov, RF Patent 2 435 303 (2011).
- [6] A. Penin, *Analysis of Electrical Circuits with Variable Load Regime Parameters: Projective Geometry Method*. 2nd Ed, Springer International Publishing AG Switzerland, 417 p., 2016.
- [7] A. Penin and A. Sidorenko, Transmission of measuring signals and power supply of remote sensors, in: J. Bonca, S. Kruchinin, eds., *Nanotechnology in the Security Systems*, NATO Science for Peace and Security Series C: Environmental Security: Springer, 267 p., 2014.
- [8] A. Penin and A. Sidorenko, Transmission of three resistance sensor signals over four wire lines with losses, in: J. Bonca, S. Kruchinin, eds., *Nanomaterials for Security*. NATO Science for Peace and Security Series A: Chemistry and Biology: Springer, 311 p., 2016.
- [9] J. A. Frank, *Schaum's Outline of Theory and Problems of Projective Geometry*, Schaum Publishing Company, 243 p., 1967.
- [10] A. Penin, A. Sidorenko, and S. Donu, MD Patent 1242 (2018).

PREDICTION OF PERCEIVED IMAGE QUALITY BY MOBILE DEVICE USERS

Pinchas Zorea, Florentin Paladi, and Tudor Bragaru

¹*Moldova State University, A. Mateevici str. 60, Chisinau, Republic of Moldova,*

²*ORT Braude Engineering college, Karmiel, Israel*

E-mails: pini.zorea@gmail.com; fpaladi@usm.md; tbragaru@usm.md

(Received December 1, 2017)

Abstract

This paper provides an overview of the PhD research of perceived image quality (PIQ) assessment, which has a great potential for image processing in many applications. The outcome of this research can be used by smartphone vendors in order to shorten “time to market,” or by any image quality experts, particularly in the academia, to reduce the time and cost of PIQ assessment of smartphones with a small high-definition display. The method can be implemented in a software if it is embedded in the social network websites to predict and improve the image quality as perceived by the users in real time. The research was based on no reference (NR) PIQ evaluation experiments combined with the VIQET software application. The experiments include human visual tests (HVTs) for subjective image quality assessment. The results of HVTs analysis identify the most effective image quality attributes for perceived image quality. The VIQET software tool was calibrated according to the HVTs scores.

1. Introduction

Digital imaging and image-processing technologies have revolutionized the way in which we capture, store, receive, view, utilize, and share images. Social network websites, such as Facebook, Instagram, Twitter, Snapchat, and other social media as well as the huge growth of smartphones, have become a significant part of our everyday lives. Worldwide, people of all ages capture photos and immediately upload them to social networks. Nearly 80% of social media time is now spent on mobile devices (Fig. 1).

The massive transportation of photos and videos in social networks occurs regardless of the material image quality. The main outcome of research is a new zero, or no reference (NR) subjective quality assessment model and framework that would enable the smartphone industry prediction of the PIQ. However, this quantitative method based on combination of results of HVTs with image analysis by VIQET [2] can be used for real time image quality improvement in social networks.



Fig. 1. Percentage of global digital snapshot [1].

Figure 2 shows a new proposed framework for real time image quality assessment and image quality improvement. Where images captured by smartphones uploaded to the social network website, the image goes first through the embedded software for real time image quality evaluation and improvement, and vice versa then it is loaded into the server.

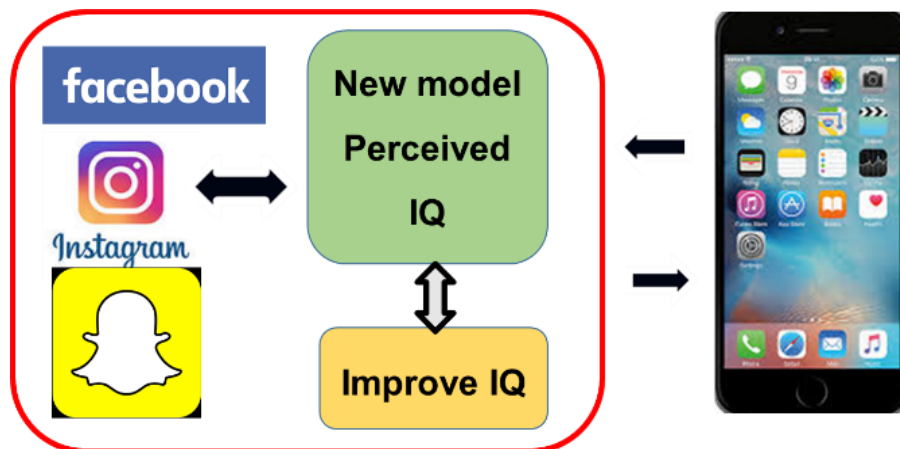


Fig. 2. Real time image quality evaluation and improvement.

The first half of this paper provides the discussion of the framework of evaluation and prediction of NR perceived image quality, utilized methods, and provided experiments. The second half of this paper proves the results of PIQ assessment model. The goal of this study is to help practitioners and researchers to keep abreast of the recent advances in PIQ assessment, which can be embedded as software in many online applications, such as social networks, and many portable devices with small high-definition display, such as smartphones, phablets, and tablet PCs.

2. Perceived Image Quality Assessment Framework

a. Selected image quality attributes for PIQ

Most of the standard image quality factors (sharpness, noise, dynamic range (exposure range), tone reproduction, contrast, color accuracy, distortion, artifacts, etc.) have been considered by researchers as important factors to IQ assessment. In this work, only four standard IQ attributes were selected: brightness, sharpness, contrast, and color saturation. With this reduced number of IQ attributes, there are several important issues to consider, such as the relationship of these IQAs to other IQ criteria used in IQ evaluation applications.

With this intention, the IQ attributes should be based on perception and measurement for technological IQ issues. The IQ attributes should be sufficiently clear to be scored by observers. In addition, the standard IQ attributes should be suitable for other IQ metrics using different IQ criteria. The existing groups of standard IQ attributes and IQ assessment models do not fulfill all of these requirements; therefore, a new group of IQ attributes is needed for HVTs and IQ assessment by software application.

Many of the IQ attributes used in research are similar and have common contribution to the perceived IQ [3–5]. This feature enables them to be grouped within more general IQ attributes in order to create a simpler evaluation of perceived IQ. There is usually a compromise between the simplicity of the IQ assessment procedure and the accuracy when it comes to human visual test performance.

The image quality circle [10] in Fig. 3 describes the link between the customer quality preference and the imaging system. This circle clearly works; however, it is inefficient over time because a new data collection effort is required every time a parameter is changed. The four elements of the PIQ approach are as follows: brightness, contrast, color saturation, and sharpness.

In this research, these attributes have been extracted to more reliable IQ attributes to be used by VIQET.

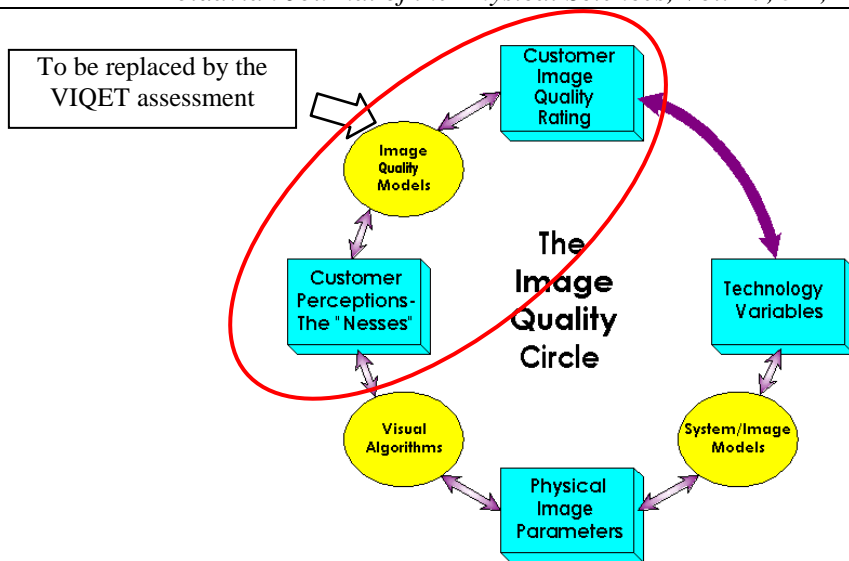


Fig. 3. Image quality circle [10] and the new approach with VIQET.

b. The actual PIQ process in industry

The flow chart in Fig. 4 illustrates the actual procedure for PIQ assessment of smartphones and the new approach implemented in PhD research. This process was performed in the vendors IQ labs by image quality experts; then, they perform subjective IQ assessment through visual experiments, while the observers are “non-experts” in image quality. The obtained results make it possible to correlate the objective assessment results with the subjective assessment results through relationships between classic IQAs and VIQET IQAs.

Image quality can be characterized according to perceptual attributes from various perspectives; however, the selection of the most important image quality attributes has different priorities in different research domains. This research brings special attentions to brightness, contrast, colors, and sharpness by utilizing the proposed image quality assessment framework [8, 9]. Hence, the classic IQAs were extracted to the VIQET application IQ categories as described in Table 1.

Table 1. Image quality attribute extraction to VIQET image quality categories

| Image quality attributes | VIQET image quality categories |
|--------------------------|--|
| Brightness | <ul style="list-style-type: none"> • Illumination • % Over-exposed • % Under-exposed • Lux |
| Contrast | <ul style="list-style-type: none"> • Dynamic range+- |
| Color | <ul style="list-style-type: none"> • Saturation • Color warmth |
| Sharpness | <ul style="list-style-type: none"> • Multi-scale edge acutance • Multi-scale texture acutance • Noise signature index |



Fig. 4. Old and new PIQ assessment processes.

c. Image quality analysis by VIQET

VIQET is an objective NR IQ evaluation tool. It estimates an overall MOS (MOS range 1 to 5, while 1 = “poor” and 5 = “excellent”) for tested images. The estimated MOS for each image is based on a number of image quality categories and statistics extracted from the test photo.

The images tested by VIQET and MOS_p were calculated and analyzed; the VIQET parameters were modified according to the relationship between IQAs and VIQET categories.

The flow chart of the process of IQ assessment using the VIQET is illustrated in Fig. 5. In that process, the VIQET IQ categories were calibrated simultaneously according to the results of HVTs of PIQ. This process ended as the VIQET scores were well correlated with the HVTs scores. The next step will be the evaluation of the VIQET capabilities in prediction of PIQ.

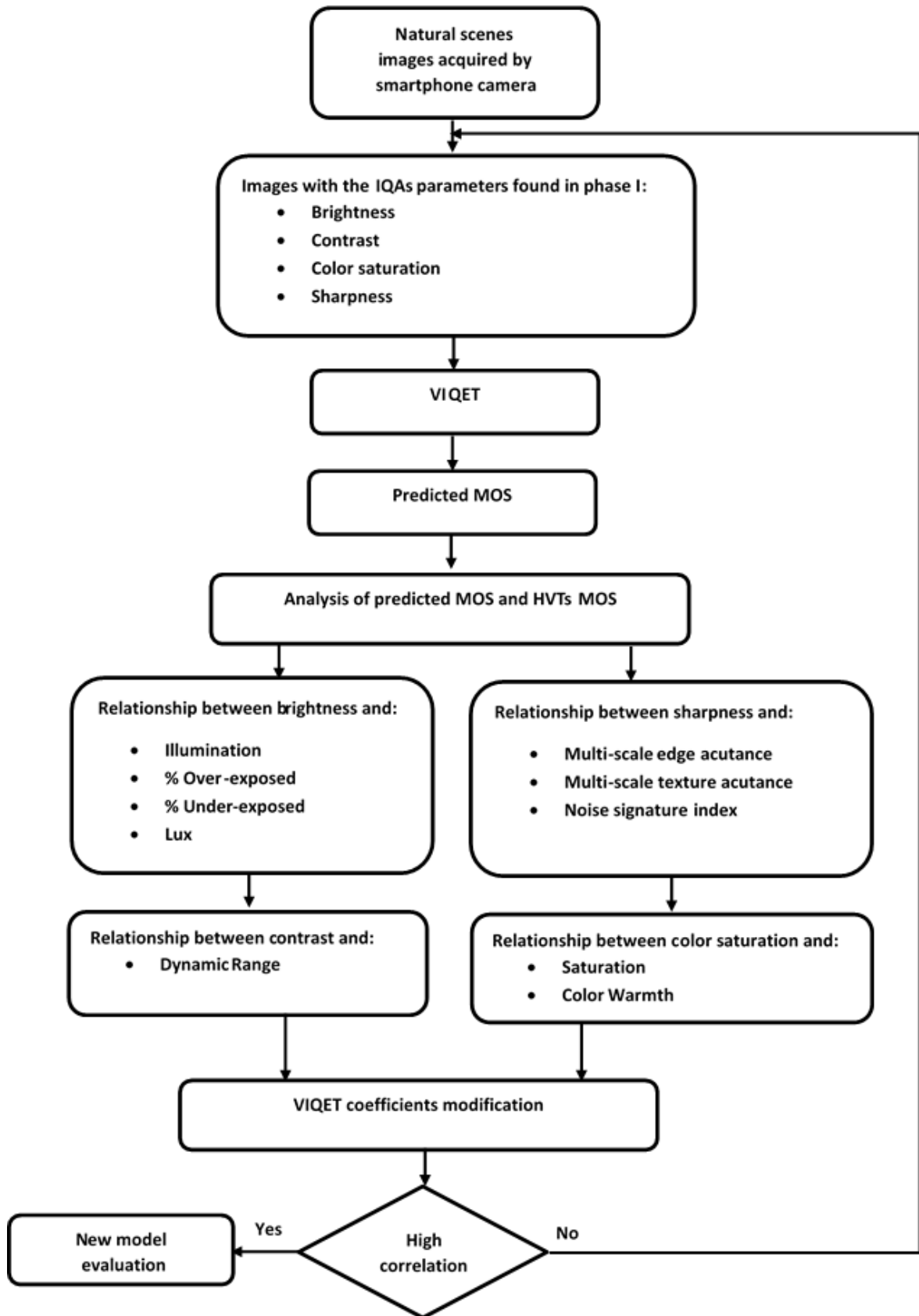


Fig. 5. Image quality assessment by VIQET.

d. Credibility of the PIQ prediction by VIQET

After the subjective tests, the credibility of VIQET in PIQ assessment was checked using the process suggested by ITU-T recommendation P.913 [7]:

(a) *Linear Pearson correlation coefficient* (Eq. (2.1)): Measures the linear relationship between a model’s performance and the subjective data. A significant advantage is that it is on a standard comprehensible scale of –1 to 1 and has been used frequently in similar testing.

The value obtained in this research was 0.86; it shows a high correlation between HVTs’ scores and VIQET’ scores.

The LPCC is calculated as follows:

$$LPCC = \frac{\sum_{i=1}^N (X_i - \bar{X}) * (Y_i - \bar{Y})}{\sqrt{\sum (X_i - \bar{X})^2} * \sqrt{\sum (Y_i - \bar{Y})^2}} \tag{2.1}$$

X_i denotes the subjective score $MOS(i)$ in HVT for the processed image (IQ attribute added), X denotes the MOS (“objective”) of the processed image (IQ attribute added), Y_i denotes the subjective score $MOSp(i)$ in HVT of the original image (no IQ attribute added), and Y denotes the MOS (“objective”) of the original image. N in equation (2.2) represents the total number of images considered in the analysis.

Root Mean Square Error (Eq. (2.2)): The accuracy of the objective metric is evaluated using the RMSE evaluation metric:

$$RMSE = \sqrt{\left(\frac{1}{N} \sum_N P_{error}[i]^2 \right)} \tag{2.2}$$

where N denotes the total number of images considered in the analysis. The accuracy and signification of the MOS results of the subjective IQ assessment during the visual test sessions were examined using the RMSE formula.

(b) *Calculating difference of MOS values (DMOS)*: The data analysis was performed using the DMOS values calculated for each IQ attribute. DMOS values were calculated using the following formula:

$$DMOS = MOS_{iq} - MOS_o \tag{2.3}$$

where MOS_{iq} is the average of MOS of IQ attribute and MOS_o is the average of MOS of the original image. In using this formula, higher DMOS values indicate better quality.

The difference between measured and predicted DMOS is defined as the absolute

prediction error P_{error} (equation (2.4)):

$$P_{error}(i) = \text{Score}(i) - \text{MOSp} \quad (2.4)$$

where index i denotes the image sample, while score (i) is the score given by the observer in HVT and MOSp is the predicted MOS (which is the average of all observers' scores).

e. Statistical significance analysis

The performance of VIQET as an objective IQ assessment tool was characterized by three prediction attributes: accuracy, monotonicity, and consistency. The statistical metrics RMSE, Pearson correlation, and outlier ratio together characterize the accuracy, monotonicity, and consistency of the VIQET performance. Figure 6 shows the predicted MOSp (predicted MOS) relation to MOS obtained by HVTs.

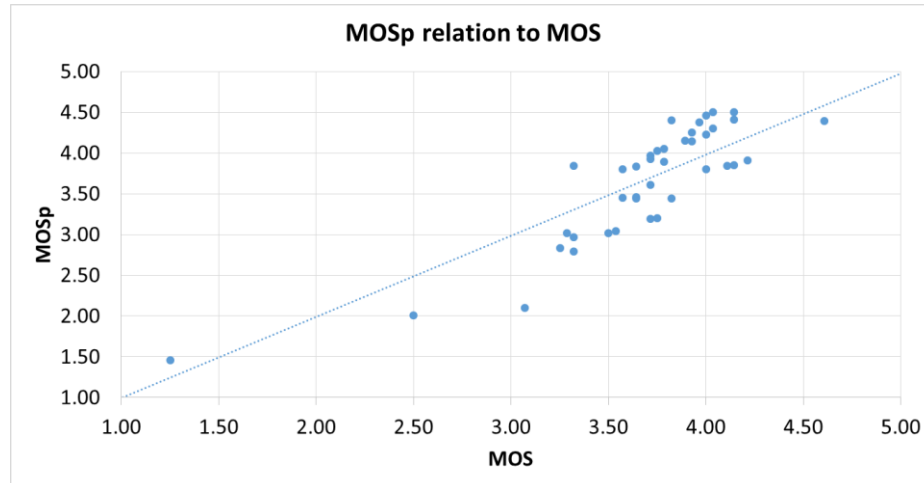


Fig. 6. MOSp relation to MOS of all images.

3. Potential PIQ Implementation in Real Applications

The results of this research on PIQ prediction have been presented to potential users in industry and academia. So far, the PIQ framework is under evaluation by several vendors of products using image processing and the IQ improvement is an essential feature of the products.

PIQ for objective image quality assessment can be implemented in smartphone industry.

Smartphone vendors gain benefits when using the PIQ assessment framework with VIQET during IQ validation. The objective and subjective IQ assessment cycles will be short and efficient (see Figs. 3, 4). The entire process of IQ assessment will be performed at home. Cost reduction of outsourcing HVTs is expected. In addition, “time to market” of new image processing features in new smartphone models will be improved.

PIQ for real time image quality assessment and improvement can be implemented in social networks.

The PIQ framework and image quality algorithms will be implemented in social networks, such as Facebook and Instagram. The block diagram in Fig. 7 illustrates the application architecture to perform real time image quality assessment and improvement of the transported images by social network members.

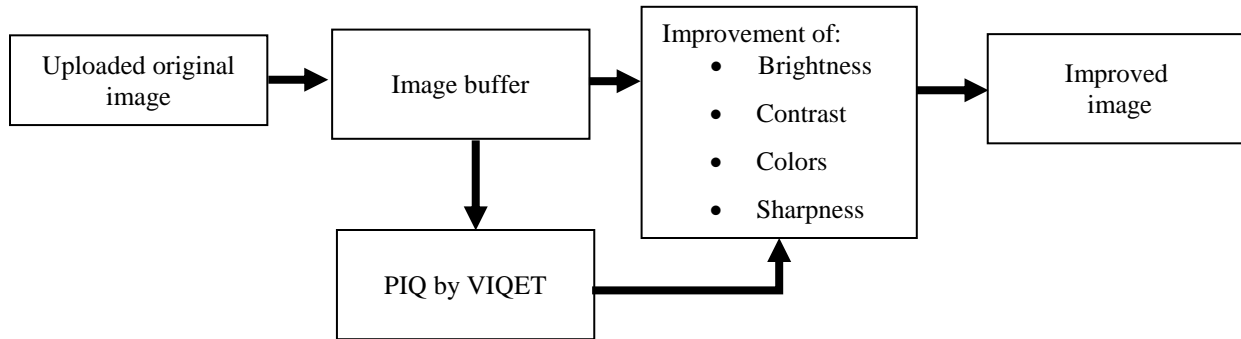


Fig. 7. Application architecture for real time IQ improvement in social networks.

PIQ for image quality improvement can be implemented in medical systems.

An Israeli company (ASI (Applied Spectral Imaging Ltd.)), which is a global leader in the development and sale of computer-aided imaging solutions for cytogenetics, pathology, and the life sciences, has evaluated the PIQ framework and found benefits of PIQ framework for IQ improvement of images taken by spectral imaging systems. The IQ of captured images is crucial in the analysis of regions of interest of the patient body. Better image quality means better image analysis by doctors.

The images shown in Fig. 8 are examples of the IQ improvements on the original image (raw image on the left) that helps doctors to identify the chromosomes' structure in the spectral image.

The colored images are images with different IQAs added to the original image in order to emphasize the differences between chromosomes (by adding colors to the raw black and white image).

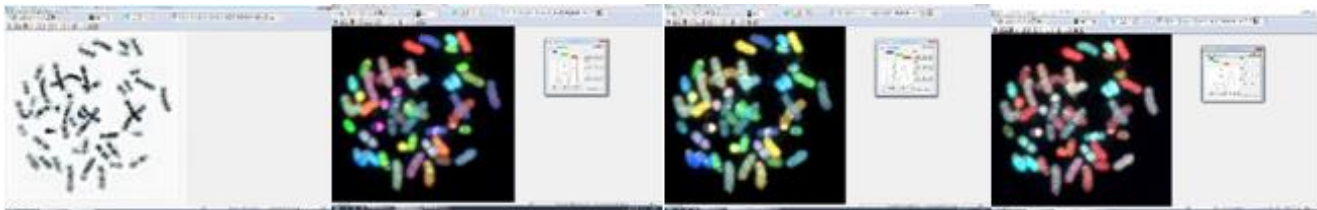


Fig. 8. Spectral images with IQ improvement (left to right).

4. Conclusions

This research proposes a new model consisting of a framework and computer based application, the VIQET for smartphone perceived image quality prediction. The research has proven a good correlation between the results of HVTs and predicted PIQ. The procedure can be customized to particular needs, programmed and integrated into image processing, social networks, communication networks with media content, medical imaging systems, etc. in order to evaluate, predict, and improve the image quality as perceived by the users. Once the software is embedded into the user application, it can evaluate the image quality of incoming images in the gateway while the images are uploaded to the server or data bases and improve their image quality in real time. The same process is done while images are downloaded from the server or data bases.

Image quality evaluation criteria of this application have been defined according to the evaluation of perceived image quality in smartphones [6, 7, 11, 14–16].

This paper has summarized the PIQ assessment related knowledge gained from PhD research, through HVTs testing, and statistical modeling approaches for NR evaluating of PIQ and predicting it. One main conclusion that can be drawn from this paper is that the proposed model can perform remarkably well at predicting human judgments of image quality.

However, it is evident that the real time improvement of IQ is far from being solved; users have yet to develop the specific software for each case. Rather, it may seem that our current accomplishments have shown that we can design algorithms to improve image quality by more conventional applications.

Acknowledgements. The authors thank E. Kobee (ASI Ltd., Israel) for his support in evaluating the PIQ framework for medical applications.

References

- [1] Nearly 80 percent of social media time now spent on mobile devices.
<https://marketingland.com/facebook-usage-accounts-1-5-minutes-spent-mobile-171561>
(accessed 22.10.2017).
- [2] Video Quality Experts Group (VQEG). <ftp://vqeg.its.bldrdoc.gov/Documents/Projects/hdtv>
- [3] P.G. Engeldrum, Proc. Conf. on Image Processing, Image Quality, and Image Capture Systems (PICS) (Savannah, Georgia, Apr. 1999), 1999, pp. 251–255.
- [4] F. Yang and S. Wan, IEEE Commun. Mag. 50 (11), 203 (2012). doi: 10.1109/MCOM.2012.6353702.
- [5] S. Bhattacharya, R. Sukhankar, and M. Shan, Proc. Int. Conf. on Multimedia, ACM, 2010, pp. 271–280.
- [6] E. Fry, S. Triantaphillidou, J. Jarvis, and G. Gupta, Image Quality and System Performance XII, Proc. Annual Symp. on Electronic Imaging (San Francisco, CA, USA, Jan. 2015).
http://westminsterresearch.wmin.ac.uk/15738/1/Fry_Triantaphillidou_Jarvis_Gupta_2015.pdf
(accessed 22.10.2017).
- [7] Methodology for the Subjective Assessment of the Quality of Television Pictures, ITU-R BT.500-11.

- [8] P. Zorea, Int. J. Sci. Eng. Res. 8, 2 (2017).
<https://www.ijser.org/onlineResearchPaperViewer.aspx?Perceived-image-quality-prediction-based-on-image-quality-attributes-extraction.pdf> (accessed 22.10.2017)
- [9] P. Zorea, Stud. Univ. Mold. 7 (97), 170 (2016).
- [10] P.G. Engeldrum, Journal of Imaging Science and Technology, 48, 446 (2004).
http://www.imcotek.com/pdf_temp/JIST_446-456_04_IQtheory.pdf (accessed 22.10.2017)
- [11] S. Triantaphillidou, J. Jarvis, G. Gupta. Proc. SPIE 9016, Image Quality and System Performance XI, 901604, 2014. p. 10.1117/12.2040007 (2015).
- [12] Y. Gao, J. Tang, R. Hong, S. Yan, Q. Dai, N. Zhang, and T. S. Chua, IEEE Trans. Image Process. 21 (4), 2269 (2012)
- [13] Y. Gao, M. Wang, Z.-J. Zha, Q. Tian, Q. Dai, and N. Zhang, IEEE Trans. Multimedia. 13 (5), 1007 (2011).
- [14] J. Hyesng and W. K. Choon, Proc. SPIE 9395, Color Imaging XX: Displaying, Processing, Hardcopy, and Applications, 93950U (January 8, 2015).
<https://www.spiedigitallibrary.org/conference-proceedings-of-spie/9395> (accessed 22.10.2017).
- [15] W. Zou, J. Song, and F. Yang, Mobile Information Systems, Volume 2016 (2016), Article ID 9621925. <https://www.hindawi.com/journals/misy/2016/9621925/> (accessed 22.10.2017).
- [16] R. Gong, H. Xu, B. Wang, and M. Luo, Optical Engineering, 51(8), 084001 (2012).
<https://www.spiedigitallibrary.org/journals/Optical-Engineering/volume-51/issue-8/084001/Image-quality-evaluation-for-smart-phone-displays-at-lighting-levels/10.1117/1.OE.51.8.084001.short> (accessed 22.10.2017)

CONTENTS

Condensed Matter and Nanomaterials Theory

V. M. Fomin

TAILORING OF ELECTRON AND PHONON ENERGY DISPERSION AND THERMAL TRANSPORT IN NANO- AND MICROARCHITECTURES.....121

S. Andronic, A. Casian

DEPENDENCE OF PEIERLS TRANSITION ON CARRIER CONCENTRATION IN ORGANIC CRYSTALS OF TTT_2I_3 IN 3D APPROXIMATION.....132

S. A. Baranov and I. I. Dobynde

INVESTIGATION OF ORIENTATION MAGNETIC PHASE TRANSITION FOR USE IN ULTRAFAST OPTOMAGNETIC BISTABLE EFFECTS138

T. Oloinic, S. S. Rusu, and V. Z. Tonciu

SYNCHRONIZATION OF CHAOTIC QUANTUM DOT LASERS WITH EXTERNAL FEEDBACK UNDER PARAMETER MISMATCH.....142

Bulk materials, Wires, and Powders

D. Meglei, S. Alekseeva

DETERMINATION OF CHARGE CARRIER SYSTEM PARAMETERS IN $\text{Pb}_{1-x}\text{Sn}_x\text{Te}$ BY JOINT ANALYSIS OF TEMPERATURE DEPENDENCES OF FOUR KINETIC COEFFICIENTS.....148

E. Condrea

STRAIN INFLUENCE ON THE DIFFUSION THERMOPOWER IN BI WIRES.....154

O.V. Iaseniuc, M.S. Iovu, A. Ghiulnare, R. Mesterca, A. Jderu, M. Enachescu

MICRO-RAMAN SPECTRA OF Ge-As-Se CHALCOGENIDE AMORPHOUS POWDERS.....161

Coordination Compounds

O. Bordian

Eu^{3+} PHOTOLUMINESCENCE IN MONONUCLEAR COORDINATION COMPOUNDS WITH DIFFERENT LIGANDS.....167

O. Danilescu

STRUCTURAL STUDY OF MONO- AND BINUCLEAR 2,6-DIACETYLPIRIDINE BIS(NICOTINOYLHYDRAZONE) COORDINATION COMPOUNDS.....177

Detectors and Sensors

L. Ghimpu

METAL OXIDE GAS SENSORS: DEVELOPMENT AND CHARACTERIZATION.....185

Ia. Kerner

DETECTION IN THE CONTACTS AT LOW TEMPERATURES: EFFECT OF THE FREE ELECTRON CONCENTRATION ON THE DETECTING PARAMETERS.....202

Miscellaneous and General Physics

A. Penin and A. Sidorenko

TRANSMISSION OF MEASURING SIGNALS BY AN INVARIANT PROPERTY OF COMMUNICATION LINES WITH LOSSES.....208

P. Zorea, Fl. Paladi, and T. Bragaru

PREDICTION OF PERCEIVED IMAGE QUALITY BY MOBILE DEVICE USERS.....217